Roller Compaction:
Improving the Powder Feeding to Compaction Zone

Mingzhe Yu

A thesis submitted in partial fulfilment of the requirements for the degree

of

Doctor of Philosophy

Department of Chemical & Biological Engineering

The University of Sheffield

Supervised by:

Prof. Agba D. Salman

Prof. James D. Litster

February 2020

List of publications

Journal papers:

Mingzhe Yu, Chalak Omar, Marcus Weidemann, Alexander Schmidt, James D. Litster & Agba D. Salman. 2020. Roller compaction: Infrared thermography as a PAT for monitoring powder flow from feeding to compaction zone, ***International Journal of Pharmaceutics***, 578, 119114.

Mingzhe Yu, Marcus Weidemann, Chalak Omar, Alexander Schmidt, James D. Litster & Agba D. Salman. 2020. Application of feeding guiders to improve the powder distribution in the two scales of roller compactors, ***International Journal of Pharmaceutics***, 573, 118815.

Mingzhe Yu, Marcus Weidemann, Chalak Omar, Alexander Schmidt, James D. Litster & Agba D. Salman. 2018. Improving feeding powder distribution to the compaction zone in the roller compaction, ***European Journal of Pharmaceutics and Biopharmaceutics***, 128, 57-68.

Conference Papers:

Mingzhe Yu, Marcus Weidemann, Chalak Omar, Alexander Schmidt, James D. Litster & Agba D. Salman. Roller compaction: online monitoring of powder feeding, UK–China International Particle Technology Forum VII, UK, 28-30 July 2019, paper No. 127.

Mingzhe Yu, Marcus Weidemann, Chalak Omar, Alexander Schmidt, James D. Litster & Agba D. Salman. Roller compaction: monitoring the temperature of different powders from feeding to compaction zone, 9th International Granulation Conference, Switzerland, 28-30 June 2019, paper No. 12.

Mingzhe Yu, Marcus Weidemann, Chalak Omar, Alexander Schmidt, James D. Litster & Agba D. Salman. Roller compaction: online monitoring of powder feeding. International Congress on Particle Technology - PARTEC 2019, Germany, 9-11, April 2019.

Mingzhe Yu, Marcus Weidemann, Chalak Omar, Alexander Schmidt, James D. Litster & Agba D. Salman. Roller compaction: monitoring feeding of temperature-sensitive powder to the compaction zone, 8th International Granulation Conference, UK, 28-30, June 2017, paper No. 198.

Acknowledgement

I appreciate the help and guidance from my supervisors Prof Agba Salman and Prof James Litster. I am deeply grateful for your help, continuous support, advice and encouragements in my PhD study. Your valuable guidance has been extremely helpful all the time during the research and writing of my thesis, much appreciated. I also appreciate supports from Dr Alexander Schmidt.

I am appreciating my parents and grandparents for all supports and love all the time in my life; they taught me learning and loving. My father encourages me to learn from everything, whatever it is about life or study. My mother taught me to treat people nice and help them whenever people need it. I am grateful that my family members, my brothers and sisters, their love and care make me feel warm. I thank and love my girlfriend Yang; she is the gift to my life.

Also, I need to thank the members of the particle product group; they treat me as a family member. Thank you for the help, support, encouragement from Chalak, Riyadh, Syed, Chuan. Thank you to Osama, Bilal, Ali, Jiankai, Arthi, Claire, Sihan, Marcus being my nice friends and gave helps., also thank my brother Yueming Li and best friend Ming.

Abstract

Roller compaction is a dry granulation technology which is widely used in the food and pharmaceutical industries. The process involves feeding of fine powders towards two counter-rotating rollers which applies high stress and produce compacts then be milled into granules. The feeding of the powder has a significant effect on the powder behaviour in the compaction zone and further on the final product properties. This thesis aims to investigate the feeding process of the fine powder during the roller compaction and improve the quality of the final product by altering some design parameters in order to get a better insight into the process.

In this study, different powders were used in the roller compaction process. A preliminary study was carried out to improve the distribution of the powder feeding by designing an array of straws and a guiding setup. The designs showed improvements in the way the powder delivered to its destination.

A more robust attempt was implemented in the feeding zone of the roller compactor, which involved novel designs of feeding guiders. These feeding guiders were located at the end of the feeding zone and used to improve the powder feeding across the width of the compaction zone. In order to find the optimum design for powders with different flow properties, novel feeding guiders were designed with different dimensions (height). The ultimate aim of these designs was to overcome the non-uniform powder distribution to the compaction zone. The novel feeding guiders were found to improve the powder distribution during compaction and produce ribbons with uniform properties. The improvement of powder distribution during compaction was evident by the uniform

temperature distribution, which was monitored in real time using online thermal imaging as a Process Analytical Technology (PAT) tool.

The online thermal imaging was used to investigate the temperature distribution across the ribbon width, which was further analysed to define the term “relative temperature uniformity” indicating the uniformity of ribbon property. The novel feeding guiders resulted in the significant increase of relative temperature uniformity comparing to original guiders. The novel feeding guiders were also scaled up to a pilot plant scale roller compactor, which was validated using powders with different flow properties. The temperature and porosity distribution across the ribbon width were examined and showed significant improvement in comparison to the original guiders.

In order to get a better insight into the process and investigate the powder behaviour while compacted between the rollers, a modified side-sealing cheek plate was designed with a special type of glass (Germanium) which allows NIR radiation to be seen through, which was used to monitor the powder temperature along feeding to compaction zone, using an online thermal imaging technique. It was found that the powder temperature increased along the feeding direction towards the compaction zone. The density distribution of the pre-compacted powder was investigated, and results supported the temperature distribution along the feeding direction.

Overall, the uniformity of ribbon properties (temperature and porosity distribution) can be improved using novel feeding guiders in the feeding zone of two roller compactors. Powder behaviour while compacted between the rollers were examined and presented with matched trend of temperature and porosity distribution.

Contents

List of tables

Symbols

A	Parameter used in Eq (4) (Johanson theory)
CI	Carr's index
D	Roller diameter
d	Thickness of compacted materials at the minimum roller gap (Johanson theory)
F	Roller force factor
F_A	Counterbalance force (Ring shear test)
F_N	Vertical normal force (Ring shear test)
F_1	Force acting on the tie rod (Ring shear test)
F_2	Force acting on the tie rod (Ring shear test)
ffc	Flow function coefficient (Ring shear test)
H_{AoR}	Height distance from powder heap to the horizontal platform
HR	Hausner ratio
K	Compressibility factor (Johanson theory)
L	Corresponding length of the uniform temperature
P_m	Maximum stress on the powder (Johanson theory)
p	Normal stress on the layer (Slab model)
p_1	Bulk density of powder before compression
p_2	Bulk density of powder after compression

R_{AoR}	Radius distance from the centre of the powder heap
Rf	Roller force
RW	Ribbon width
S	Rolle gap
T_{max}	Maximum temperature of ribbon
T_{ave}	Average temperature of ribbon
T_{min}	Minimum temperature of ribbon
t	Thickness of slab (Slab model)
v	Acute angle between the tangent to the roller surface (Johanson theory)
W	Roller width
x	Distance gradient start from minimum roller gap (Johanson theory)
$Y(\rho)$	Yield stress (Slab model)

Greek alphabet

α	Nip angle (Johanson theory)
α_x	Instantaneous angle (Slab model)
δ_{Temp}	Deviation of temperature
ε_p	Porosity of ribbon
θ	Angular position (Johanson theory)
θ_e	Effective angle of internal friction
θ_{repose}	Angle of repose
μ	Johanson theory parameter (Johanson theory)
$\mu(p)$	Coefficient of friction (Slab model)
μ_w	Coefficient of wall friction (Ring shear test)
ρ_{loose}	Loose bulk density of powder
ρ_{true}	Powder true density
ρ_{ribbon}	Ribbon density
ρ_{tap}	Tapped bulk density of powder
ρ_1	Bulk density of powder after applying pressure of p_1
ρ_2	Bulk density of powder after applying pressure of p_2
σ	Normal stress on the powder (Johanson theory)
σ_θ	Mean normal stress at position θ (Johanson theory)
σ_c	Unconfined strength (Ring shear test)

σ_w	Normal stress in wall friction measurement (Ring shear test)
σ_x	Stress along x direction (Slab model)
σ_1	Consolidation stress (Ring shear test)
τ_f	Friction stress (Slab model)
τ_w	Shear stress in wall friction measurement (Ring shear test)
φ_w	Angle of wall friction (Ring shear test)
ω	Angular velocity (Ring shear test)

Chapter 1 Introduction

1.1 Granulation

With the development of powder processing, granulation has become more and more important in different industries, such as pharmaceuticals, food, detergents, catalysts, ceramics and pesticides. Granulation is a size-enlargement process of fine particles, which improves the uniformity and flowability of a downstream blend of materials (Guigon and Simon, 2003, Michrafy et al., 2011a, Omar et al., 2015).

Granulation could be either a wet or dry process. It can also be either a batch or continuous process. Roller compaction is a continuous process, which could process the moisture-sensitive powder, as there is no need to add liquid binder (Guigon and Simon, 2003, Muliadi et al., 2013). For instance, dry granulation is more desirable in comparison to wet granulation for some pharmaceutical powders due to its sensitivity to moisture (Skikant et al., 2015, Yu et al., 2018). Additionally, dry granulation is widely used in different fields because of its high efficiency, energy-saving and easy to scale up (Yu et al., 2018).

1.2 Roller compaction

1.2.1 Introduction of roller compaction

Roller compaction usually consists of three stages: feeding, compaction and crushing (Al-Asady et al., 2016, Yu et al., 2018). In the feeding stage, the powder is fed from the hopper towards two counter-rotating rollers, by either gravity or screw feeders. The particles are rearranged under low stress in this stage (Kleinebudde, 2004). As the particles start to enter the compaction zone where the stress increases dramatically, they are compressed into ribbons or flakes as a result of the stress applied by the rollers. In the following crushing stage, ribbons or flakes are crushed into granules of different sizes depending on the application requirement.

1.2.2 Types of roller compactors

There are two types of feeding systems in the roller compaction process: gravity feeding and screw feeding (Guigon and Simon, 2003). The gravity feeding is shown in Figure 1-1 (a). The screw feeding could be either inclined or horizontal, as shown in Figure 1-1 (b) and (c). For the gravity feeding, powder is fed by gravity (screw may need in some machine) to the compaction zone and pressed by the rollers. The inclined and horizontal feeding, use the screw to drive the powder to the compaction zone. Comparing to the gravity feeding, feeding with screw ensures a continuous powder feeding which is useful for the powder with poor flow performance (Wu et al., 2010). Two sealing systems are commonly used to prevent the leaking of the powder during the compaction process which are rimmed rollers and the side cheek plates.

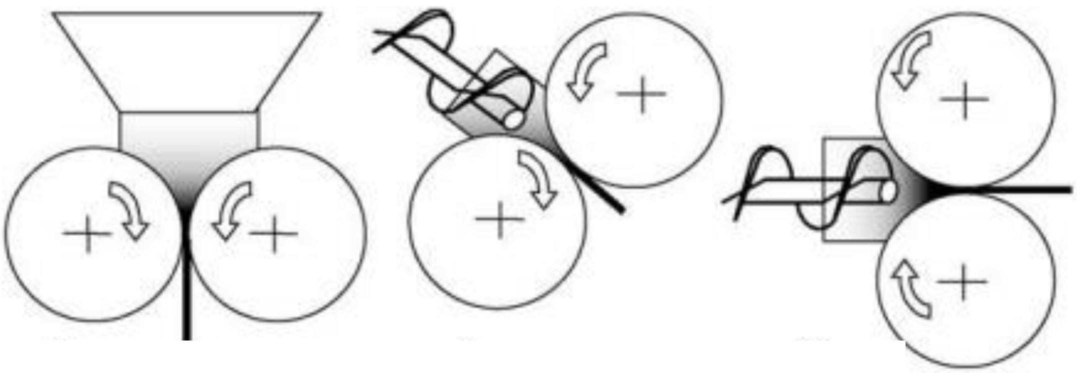

a b c

Figure 1-1: Three types of powder feeding in the roller compacter: a – vertical gravity feeding; b – inclined screw feeding; c – horizontal screw feeding (Guigon and Simon, 2003).

1.2.3 Advantages and limitations of roller compaction

Roller compaction has numbers of advantages and limitations. Regarding the advantages, the roller compaction could process a moisture-sensitive powder due to the absence of water in this process (Omar et al., 2015). Moreover, it is a continuous granulation process, which could process a large quantity of powder and improve manufacturing efficiency (Kleinebudde, 2004, Guigon and Simon, 2003). Finally, it is also an easily operated, high efficiency and energy-saving process (Yu et al., 2018). In other words, roller compaction saves time and money.

Despite the advantages of using roller compaction in the pharmaceutical and food industries, there are still limitations to the process. First of all, there is a large amount of fines produced in the process, which could be uncompacted or leaked powder during the compaction process. Thus, it is essential to recycle the fines, which may have a negative impact on the content uniformity in the product. Secondly, for some types of powder, such as hard materials (lactose), the amount of fines is large, and it is also difficult to achieve full width of ribbons (Omar et al., 2015). Finally, the properties of the ribbons are not uniform across ribbon width, such as density (Michrafy et al., 2011a). Thus, the granules resulted from the crushing stages could not be uniform in term of quality such as strength and size, as more fines could be produced from the weak parts of the ribbon. Based on the limitations of the application of roller compaction, there need to be improved in the uniformity of powder distribution in the compaction zone, which has a significant effect on the ribbon and the granule properties. These issues will be focused on addressed in this project.

1.3 Aims of the research

The uniform powder feeding is crucial for the powder processing industries. The non-uniform powder distribution could cause the non-uniform quality of the product, especially for continuous powder processing. For example, roller compaction only requires dry powders; thus, powder flow behaviour in the process is vital for product quality.

This study will be focused on improving the powder feeding uniformity in the roller compaction process and aims to improve the quality of the product. A detailed study will be conducted on the effect of primary powder properties on the flowability during the discharge of different types of powder.

This study then focuses on the geometry design to improve the distribution of the feeding powder in the roller compaction process. The improvement of the powder feeding system in the lab-scale roller compactor will be validated and scaled up to a pilot-scale compactor). Online thermal imaging will be implemented in the process to examine the temperature of the ribbon in real time. The thermal imaging will also be used to investigate the temperature of the powder at different stages from the feeding to the compaction zone to gain better insight into the process.

1.4 Overview of the thesis

Chapter 2 presents a review of previous works on the powder flow and roller compaction process. It summarised different methods of examining the powder flowability and product properties from the roller compaction, especially the inhomogeneous properties. Also, previous theory and experimental were briefly explained.

Chapter 3 illustrates the preparation of materials and equipment used in the experiments, examining methods of the powder flowability and product properties.

Chapter 4 describes a method of geometry design to improve powder flow and distribution (gravity discharge). The results of powder flowability are also discussed with different relative humidity condition.

Chapter 5 demonstrates a novel design of feeding guiders', which is to improve the powder distribution in the roller compaction process and implemented in two different roller compactors (WP120 Pharma and WP200 Pharma). The product properties, such as temperature profiles, porosity profiles, and improvement of novel feeding guiders were explained with details.

Chapter 6 presents the design of feeding guiders with a range of dimension according to different materials' flow properties. The properties of roller compacted product are monitored online by thermal imaging. In addition, the determination and comparisons of the product uniformity have been discussed in details. A design space with process parameter and material properties has been proposed for achieving uniform product property.

Chapter 7 proposes a new method to online monitor powder feeding process (temperature distribution) along the feeding to compaction direction. Also, the density distribution of compacted powder was presented and matched with temperature distribution to investigate the nip region with different roller forces.

Chapter 8 presents the conclusions of the entire study and recommendations in the future.

Chapter 2 Literature Review

This chapter involved reviewing previous studies about the powder flow, methods and technologies developed in the roller compaction process.

2.1 Powder flow behaviour

Powder flow has been investigated in process engineering, which involves handling, conveying, compaction and storage (Saker et al., 2019). For example, the design of hopper in the roller compactor is similar to the silo, which stores and initiates the powder feeding (powder discharge). The powder flow could be affected by the design of the unit and process parameters (Freeman, 2007, Schulze, 2007). Figure 2-1 shows the different pattern of powder flow in the silo. Figure 2-1 (a) shows the mass flow where the powders are flowing in all downwards directions. However, a stagnant zone in Figure 2-1 (b) and (c) is formed when the powder is cohesive (Schulze, 2007). In addition, the particles are not moving with the same velocity because of the wall and interparticle friction. The particle velocity profile is displayed in Figure 2-2. The particles at the centre have a higher velocity than that at the sides.

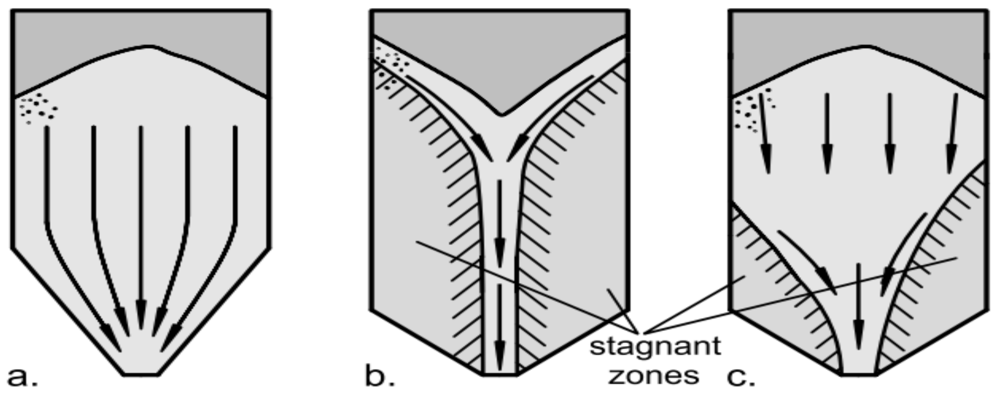

Figure 2-1: Mass flow (a) and stagnant zone occurred in the silo (b) and (c) (Schulze, 2007).

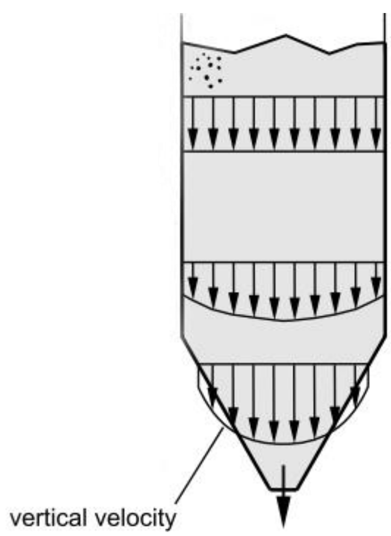

Figure 2-2: Particle flow with a velocity profile in a silo (Schulze, 2007).

2.2 Powder flow properties

Powder flow properties play a vital role in the processes, such as mixing, packing and filling, and storage (Capece et al., 2016). Measuring powder flow property is generally divided into three categories: (1) the test for the non-compacted powder, such as angle of repose; (2) the test for the tapped powder, such as Hausner ratio and Carr's index; (3) the test for the consolidated powder, such as shear test, which includes flow function coefficient, angle of effective internal friction and wall friction (Saker et al., 2019, Salehi et al., 2017, Leturia et al., 2014, Horio et al., 2014). Powder flow property is affected by particle size, particle shape and moisture content (Yu et al., 2011, Emery et al., 2009, Liu et al., 2008, Kaerger et al., 2004, Litster and Ennis, 2004).

2.2.1 Angle of repose

The angle of repose is one of the ways to characterise the flow properties of powder or granular material under the non-compacted condition. Powders are discharged from a fixed height onto a flat surface. The angle between the slope of the heap of the powder and the horizontal platform was determined, which represents the angle of repose as shown in Eq (1). The higher the angle of repose, the poorer the flowability of the powder (Teng et al., 2009, Freeman, 2007). The angle of repose was influenced by particle shape, size, and moisture content, for example, the spherical particle contributed to a decrease of repose angle (Yu et al., 2011, Liu et al., 2008, Kaerger et al., 2004).

$$\theta_{repose} = arctan\frac{H_{AoR}}{R_{AoR}} \qquad \text{Eq (1)}$$

Where θ_{repose} is the angle of repose,

H_{AoR} is the height distance from the powder heap to the horizontal platform,

R_{AoR} is the radius distance from the centre of the powder heap.

The powder flow property is influenced by the moisture content or relative humidity (Lumay et al., 2016, Stoklosa et al., 2012, Wu et al., 2010). High relative humidity or moisture content could result in sticking and caking of the powder during the storage and processing (Lumay et al., 2016, Stoklosa et al., 2012, Wu et al., 2010). Lumay et al. (2016), Omar et al. (2016), Stoklosa et al. (2012) and Wu et al. (2010) mentioned that increasing the moisture content contributed to the increase of repose angle. The reduction of powder flowability with the increasing moisture content results from the liquid bridge between the particles. However, the moisture could decrease the friction as it works as a lubricant (Wu et al., 2010, Emery et al., 2009, Coelho and Harnby, 1978).

2.2.2 Hausner ratio and Carr's index

Hausner ratio (HR) and Carr's index / Compressibility Index (CI) are two similar methods to measure the powder flow property at compression condition. Both of them need to make the powder from loose to a tapped bulk condition (Saker et al., 2019). Qiu et al. (2017) and Weyenberg et al. (2005) argued that a lower Hausner ratio or Carr's index indicated a better flow property. They also mentioned that the value of Hausner ratio and Carr’s index could be affected by the particle size, particle shape and moisture content.

Hausner ratio (HR) is defined as the ratio of the tapped bulk density to the loose bulk density:

$$HR = \frac{\rho_{tap}}{\rho_{loose}} \qquad \text{Eq (2)}$$

Where ρ_{tap} is the tapped bulk density of the powder,

ρ_{loose} is the loose bulk density of the powder.

Carr’s index (CI) is defined as the ratio of the difference of the tapped and loose bulk density to the loose bulk density:

$$CI = \frac{\rho_{tap} - \rho_{loose}}{\rho_{tap}} \qquad \text{Eq (3)}$$

2.2.3 Shear cell tests

Comparing to the previously described methods of measuring the powder flow property, the shear tests include standardised procedures, which is used for silo or other design that considers the consolidation of the powder (Salehi et al., 2017, Schulze, 2007, Jenike and Shield., 1959). The powder flowability (flow function coefficient, internal friction angle and angle of wall friction) can be measured by the shear tests (Jenike shear tester and Schulze shear tester) are shown in Figure 2-3.

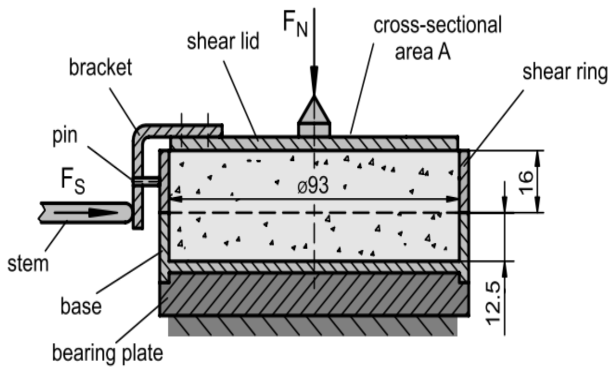

Jenike shear tester

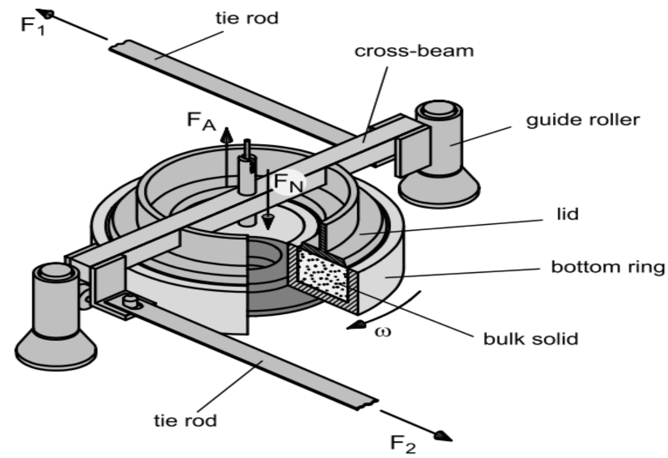

Ring shear tester

Figure 2-3. Jenike shear tester and Ring shear tester (Schulze, 2007).

2.2.3.1 Flow function coefficient

In the Ring Shear Testers RST-XS (Dietmar Schulze, Germany), the testing procedure of the flow function coefficient is to firstly apply a normal load to consolidate powder (pre-shear). Then at the shear stage, different normal stress levels are used, which are less than pre-shear stress, the consolidated powders are subsequently sheared to failure.

Generally, powder flowability can be classified according to the value of flow function coefficient (ffc), “not flowing; very cohesive; cohesive; easy-flowing and free-flowing" (Fitzpatrick et al., 2004). Sun (2016) investigated the effects of relative humidity and normal stress on the powder flowability (MCC) by using Schulze ring shear tester. As the relative humidity increases, the flow function coefficient (ffc) decreases, which means the flowability decrease, as shown in Figure 2-4. Also, the increase of the normal stress resulted in the increase of the flow function coefficient. Furthermore, Omar et al. (2016) and Wu et al. (2010) stated that moisture content influenced the powder flowability (flow function coefficient). The increase in moisture content resulted in a decrease in flow function coefficient and poorer flowability.

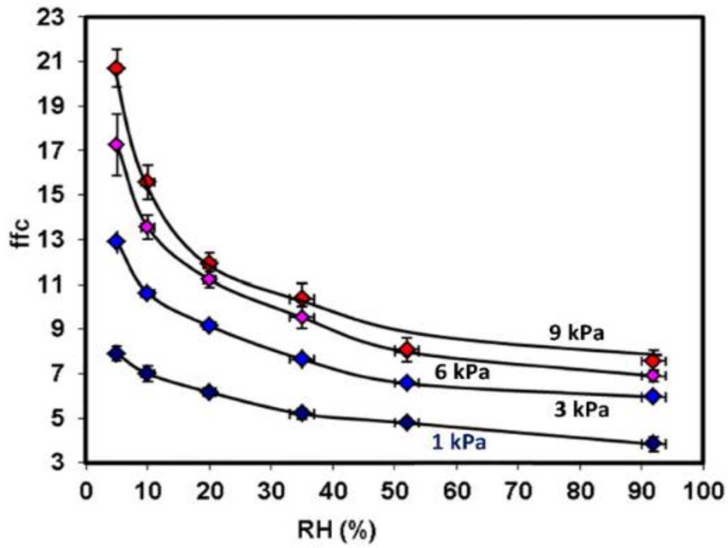

Figure 2-4. Flow function coefficient (ffc) of MCC on RH under different pre-shear normal stresses (Sun, 2016).

2.2.3.2 Angle of wall friction

The angle of wall friction is used to define the friction between a bulk powder and a wall material surface (Schulze, 2007). Jager et al. (2015) argued that the angle of wall friction angle increased with decreasing consolidation stress, as shown in Figure 2-5. At low values of consolidation stress, the powders have not undergone appreciable deformation, and their surface roughness remains relatively intact, resulting in increased friction with the wall material. At high values of consolidation stress, particles began to deform into flatter, smoother bodies resulting in decreasing friction with the wall material (Jager et al., 2015). Moreover, Yu et al. (2013) concluded that the angle of wall friction decreases with the increasing amount of magnesium stearate (MgSt).

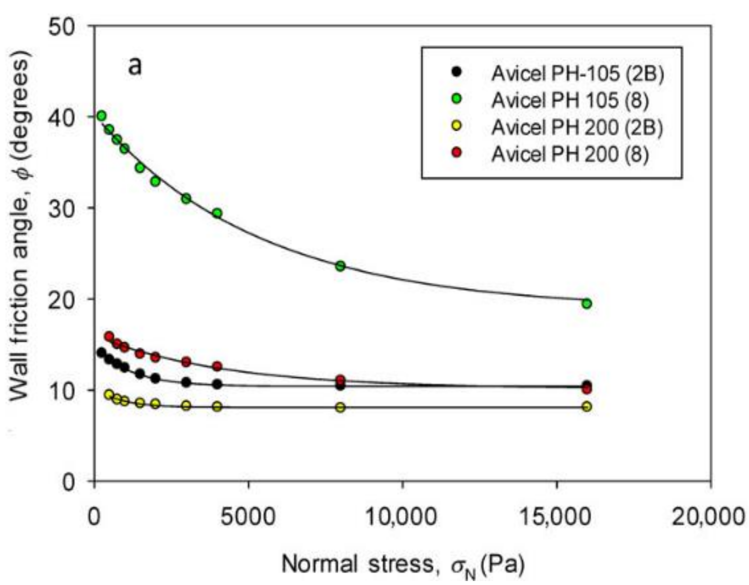

Figure 2-5. Angle of wall friction under different normal stress (Jager et al., 2015).

2.3 Roller compaction

This section involves reviews of experimental and predictive model studies. The studies of roller compaction mainly include feeding process (gravity feeding, screw feeding and mixed feeding) and compaction process (counter-rotating compressing rollers). The reviews of experimental studies involve the powder flow performance in the feeding stage and the examined properties of the product (ribbon) from the compaction stage. The reviews of predictive models include the Johanson theory, Slab Model, Finite element model and Discrete element model, which can predict the stress distribution applied from the rollers and the product properties according to the primary powder properties.

2.3.1 Experimental studies of roller compaction

The experimental studies of roller compaction involve the examination of powder flow behaviour in the feeding stage and properties of compacted powder/ribbon from the compaction stage. The powder performs differently in the feeding stage due to the powder properties and design of the feeding zone (Omar et al., 2015, Krok et al., 2014, Guigon and Simon, 2003). The properties of compacted powder/ribbon can be examined by online and offline measurement, which is also influenced by the process parameters used in the roller compaction process.

2.3.1.1 Powder flow in the feeding stage

Measuring methods of powder flow in the feeding stage

There are some measuring technologies developed in the feeding stage to monitor the process and investigate the powder flow behaviour (Omar et al., 2015). As for the gravity (vertical) feeding process, Miguelez-Moran et al. (2009) examined the powder flow behaviour in the feeding stage by using optical measurement to define a “drag angle” from the top view of feeding zone, which indicated the powder flow behaviour. They stated that powder at the roller centre moved with a higher rate than that at the roller edges due to the friction between the powder and stationary side-sealing cheek plate. Guigon and Simon (2003) used a Plexiglas window fitted on the cheek plate to analyse the trajectories of powder using a video analysis software. They argued that particle motion is not continuous due to the periodicity of the screw rotation. Also, Krok et al. (2014) developed a method of Digital Particle Image Velocimetry (DPIV) with a transparent cheek plate to investigate the velocity field in the powder feeding stage. The velocity of particles was increasing as the particles are moving towards the smooth roller surface (Krok et al., 2014).

While in the horizontal feeding process, Omar et al. (2016) used the Particle Image Velocimetry (PIV) with a transparent cheek plate and coloured particles to examine the powder surface velocity in the feeding stage. The measured powder surface velocity by the PIV method was lower than the tip speed of the knurled roller (Omar et al., 2016). Particle Image Velocimetry (PIV) method improved an understanding of powder flow behaviour (such as velocity) in the feeding stage, with requirements of the light condition and distinguishing the colour difference of particles.

Non-uniform powder flow in the feeding stage

The roller compaction starts with a powder feeding process with a storage hopper. As the powder moves from the hopper, there could be mass flow or core flow, and that depends on whether the powder is cohesive or if the wall friction exists. If the powders are cohesive and there is wall friction, the stagnant zone occurs in the feeding process as shown in Figure 2-6 (a), and non-uniform powder distribution is shown as the concave powder-roller interface in Figure 2-6 (b) (Miguelez-Moran et al., 2009). Thus, more powders are fed at the centre than the sides of rollers.

Also, Miguelez-Moran et al. (2008) used the lubricated powder to improve the powder flow in the hopper, which reduced the friction between the powder and the inner wall of the hopper. They found that the lubricated powder resulted in a change of “drag angle”, but there were still some powders remained close to the cheek plate.

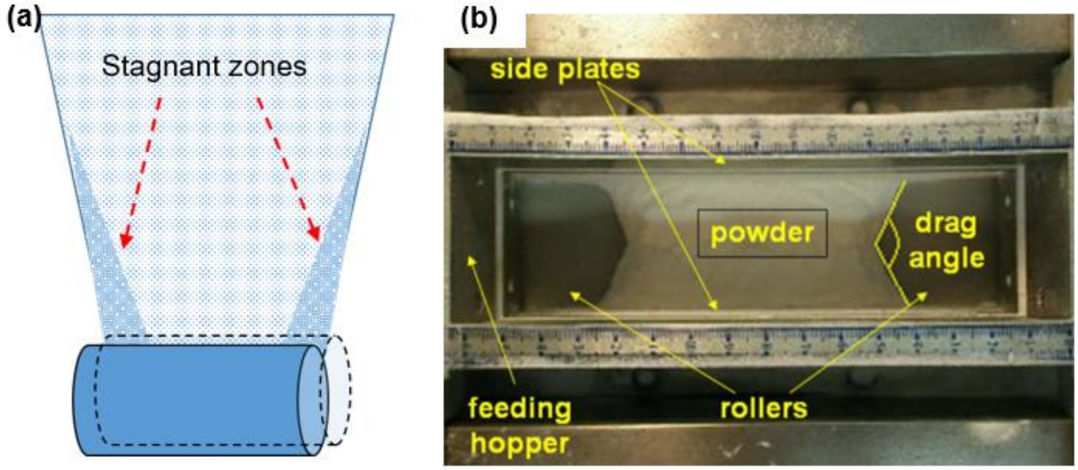

Figure 2-6: Powder feeding towards rollers: (a) Stagnant zone occurs in the powder feeding process; (b) Powder flow pattern in the feeding zone of roller compactor (Miguelez-Moran et al., 2009).

The phenomenon of stagnant powder zone also exists in the roller compactor with the horizontal screw feeding process, which can affect the uniformity of ribbon properties across the width. The screw feeder drives powders towards the rollers. When the powders leave the screw towards the rollers, it will pass through different positions which are represented by different angles, as shown in Figure 2-7. Firstly, the slip angle starts where powders contact the rollers until compressed by the rollers. Secondly, the nip angle is starting when the surface velocity of the particles is equal to the roller velocity (Bindhumadhavan et al., 2005). The value of the nip angle depends on the material properties such as flowability and compressibility, in addition to the roller compactor design and process parameters (Cunningham et al., 2010). Next, the neutral angle is the angle at which the powder experienced maximum normal stress from the rollers (Miguelez-Moran et al., 2008).

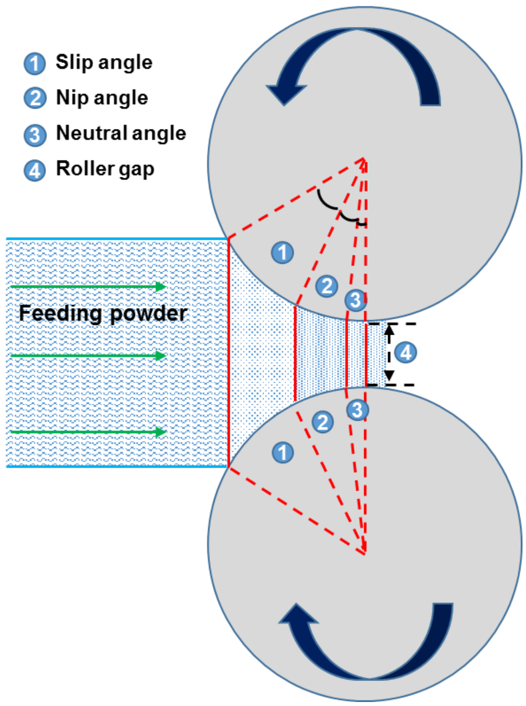

Figure 2-7: Regions of roller compaction: (1) Slip angle; (2) Nip angle; (3) Neutral angle; (4) Roller gap.

Some work had been done by using transparent cheek plate (side-sealing) to study the powder flow in the feeding zone. For example, Omar et al. (2016) and Krok et al. (2014) applied the particle image velocimetry (PIV) by using a high-speed camera to examine particle velocities of particles from the feeding to the compaction zone by using a transparent cheek plate. The difference between those studies is the feeding system: Omar et al. (2016) studied on the horizontal screw feeding system, while Krok et al. (2014) studied the vertical feeding system. Omar et al.

(2016) found that the speed of the moving powder gradually increased until contacting the rollers where a significant increase in speed occurs as displayed in Figure 2-8. In addition, Omar et al. (2016) suggested that conditioning the powder at a high relative humidity resulted in a poor flow performance with low velocities of particles in the feeding process. Moreover, Krok et al. (2014) concluded that the high powder flowability contributed to the high velocities of particles in the feeding zone. The results indicate that the flowability of powder has a major influence on the particle velocities in the feeding zone.

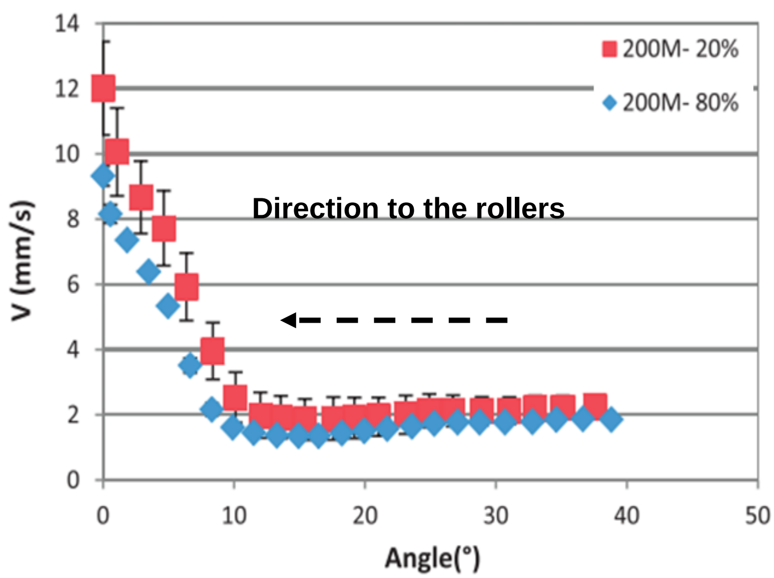

Figure 2-8: Effect of powder flowability on the velocity of particles in the feeding zone of roller compaction, Pharmatose 200M under the condition at 20% and 80% of relative humidity (Omar et al., 2016).

2.3.1.2 Ribbon properties in the compaction stage

Measuring methods of ribbon properties - Process Analytical Technologies (PAT) and offline measurements

Process Analytical Technology (PAT) presents convenient ways to observe the product quality and give feedback to change the variables in the roller compaction process (McAuliffe et al., 2014). For example, Infrared thermography (thermal imaging) has been used as Process Analytical Technology (PAT) in the compaction stage to investigate the product properties (porosity and temperature of ribbons) (Wiedey and Kleinebudde, 2018, McAuliffe et al., 2014). Infrared thermography (thermal imaging) had been recently used to study the ribbon temperature and uniformity of temperature distribution across the ribbon width (Wiedey and Kleinebudde, 2018, Yu et al., 2018, Omar et al., 2016, Al-Asady et al., 2015, Osborne et al., 2013). In those studies, an online monitoring method using a thermal camera was used to investigate the surface temperature of the ribbons as they exited from the roller gap.

Moreover, the offline measurement can be carried out when the roller compaction process has been shut down. Offline measuring the properties of product from roller compaction stage can be performed in different ways. For example, Miguelez-Moran et al. (2009) used three different methods, X-Ray, Micro-indentation and sectioning, to examine the relative density across the ribbon width. Also, Guigon and Simon (2003) used the light transmitting compact to examine the density distribution. They showed the heterogeneity density distribution by defining a different grey level of the images. Offline measurement, such as X-Ray, can be used to examine more details of the compacted powder, such as density or porosity distribution across the ribbon width and along the feeding direction to the compaction direction (including pre-compaction to the compaction) in the from the pre-compaction to the compaction stage (Al-Asady et al., 2016, Yu et al., 2018, Yu et al., 2020a, Yu et al., 2020b).

Non-uniform properties across the ribbon width

The non-uniform properties across the ribbon width result from the non-uniform powder distribution from feeding process, which is mainly influenced by the screw feeder, friction between powders and cheek plate (Krok and Wu, 2019, Yu et al., 2018, Michrafy et al., 2011b). The screw feeder pushes the powder forward, and the particles are arranged with time which resulted in the powders being pre-compacted in the feeding zone (Rowe et al., 2013, Muliadi et al., 2013). The friction of the powder with cheek plates and with each other contributed to the non-uniform powder distribution across the roller width in the feeding process. That resulted in a different amount of powder are compacted across the roller width in the compaction process. Guigon and Simon (2003) and Michrafy et al. (2011a) concluded that the powder feeding process influenced the uniformity of the ribbon properties. For instance, Figure 2-9 shows that the bright patterns are denser than the dark ones that linked to the stress applied to the powders (being ribbons). The density and porosity distribution are not uniform across the width and the length because of the periodically rotating screw (Mazor et al., 2018).

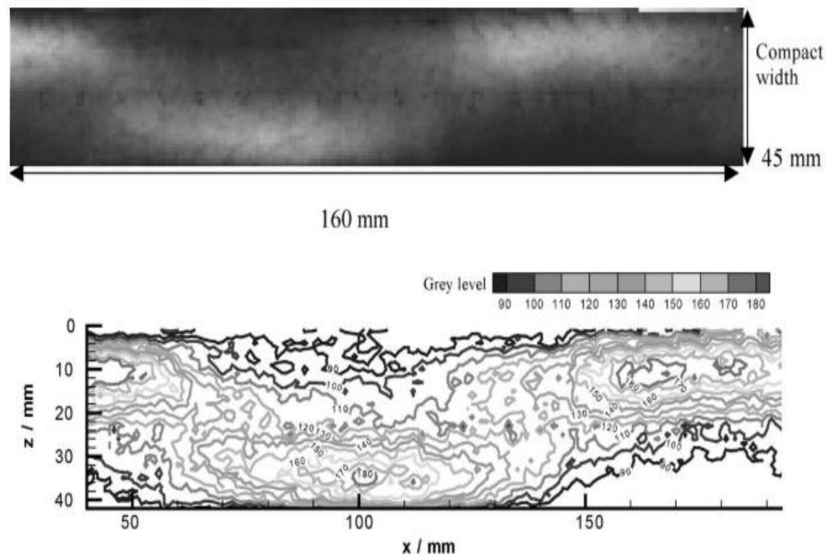

Figure 2-9. The non-uniform density distribution across the ribbon width by light transmitted photography (Guigon and Simon, 2003).

Yu et al. (2018), Omar et al. (2016), Miguelez-Moran et al. (2009), and Funakoshi et al. (1977) also mentioned that the non-uniform amount of powder was fed across the roller width, and the amount of powder at the sides of the roller is not sufficient to produce full-width ribbon during the compaction. The amount of powder fed at the centre is higher than that at the side of the rollers, which explains the non-uniform density distribution across the ribbon width (higher at the ribbon centre and lower at the ribbon sides). Miguelez-Moran et al. (2009) used three different methods to investigate the relative density across the ribbon width. They also showed that the density of the ribbon centre was the highest and gradually decreased to a minimum value of at the side of the ribbon, as shown in Figure 2-10.

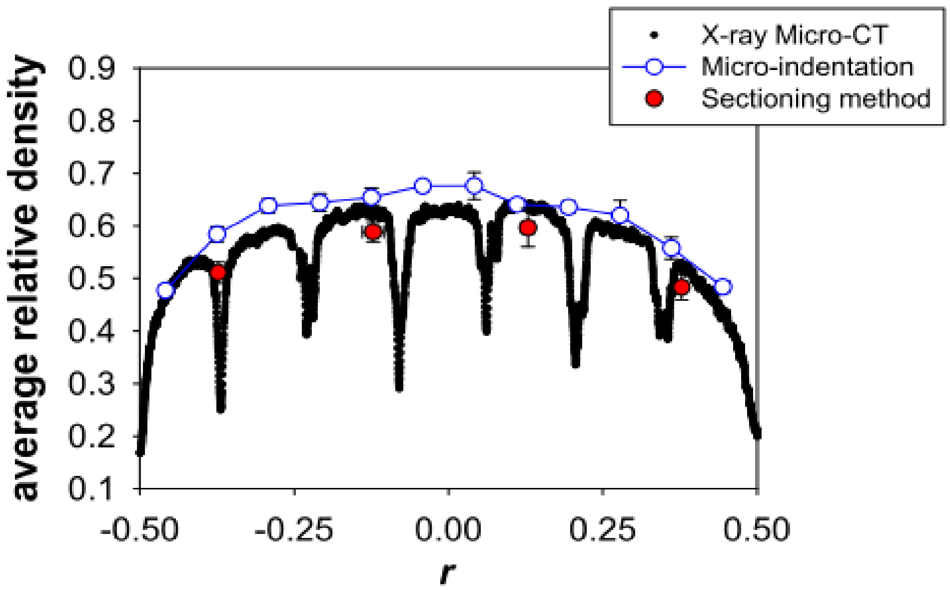

Figure 2-10. Relative density across ribbon width (Miguelez-Moran et al., 2009)

Funakoshi et al. (1977) used concave-convex rollers (rim angle of 65 °) with rectangular chute in the roller compaction in order to achieve the relatively uniform pressure across the width, as shown in Figure 2-11. The results showed less difference of stress distribution across the width of concave-convex rollers than the flat surface roller. The reason is the reduced the effect of wall friction from the side seals, as powders are flowing towards minimum roller gap. Additionally, the concave roller/rimmed roller reduced the amount of fines because of its concavity holding the powders during the feeding process (Funakoshi et al., 1977).

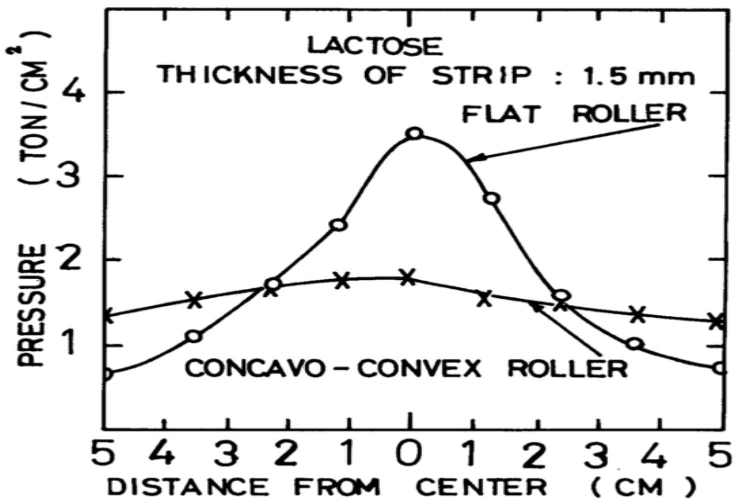

Figure 2-11. Comparison of a concave-convex roller and flat roller on the pressure (lactose used) (Funakoshi et al., 1977).

Some recent studies had investigated the uniformity of ribbon properties in addition to the reduction of the fines using the rimmed rollers (Mazor et al., 2016, Wiedey et al., 2018, Wiedey and Kleinebudde, 2018, Omar et al., 2019). Wiedey and Kleinebudde (2018) showed that the relative density and temperature increased at the edges of the ribbon and decreased at the centre of the ribbon, comparing the rimmed rollers to cheek plate (side-sealing) as shown in Figure 2-12. The temperature and relative density at the edges of ribbons were higher than that at the centre of ribbons from the rimmed rollers, which indicated non-uniform properties across the ribbon width. Furthermore, Omar et al. (2019) modified the design of the roller with a curved surface. New curved roller resulted in a significant improvement in the uniformity of the temperature across ribbon width as illustrated in Figure 2-13, which also resulted in a decreasing difference in the porosity between the centre and the side of the ribbon (Omar et al., 2019).

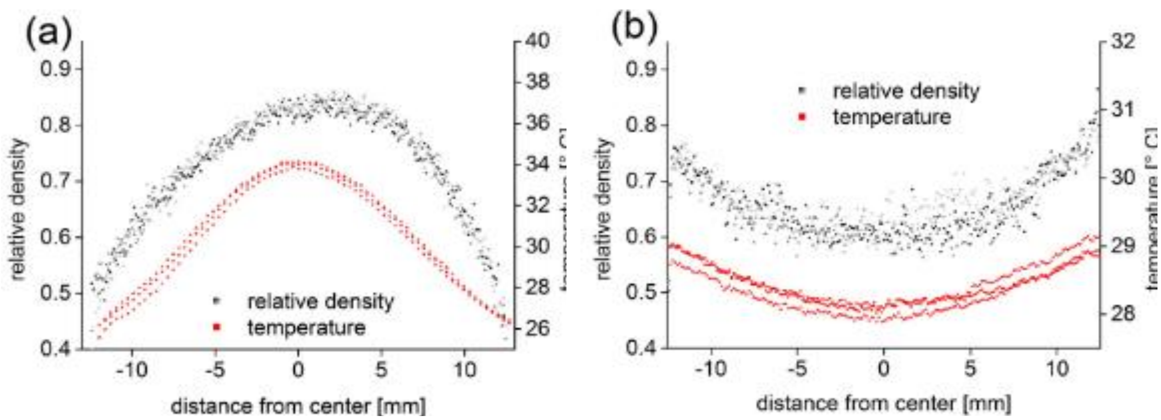

Figure 2-12. Relative density and temperature distribution across ribbon width: (a) cheek plates, (b) rimmed rollers (Wiedey and Kleinebudde, 2018).

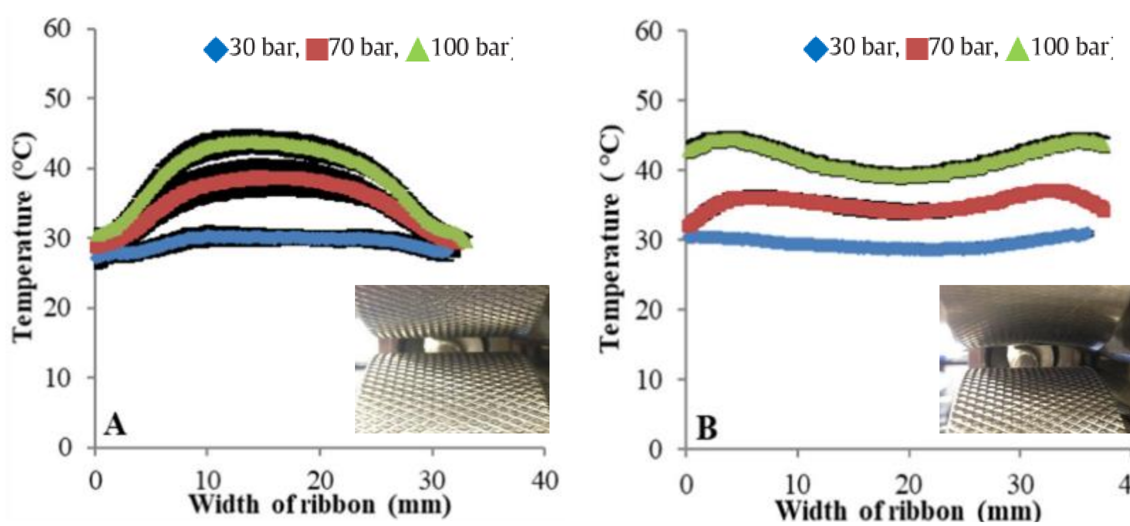

Figure 2-13. Temperature profile across ribbon width (Lactose 200M): flat roller (A); curved roller (B) (Omar et al., 2019).

Limited studies had investigated the uniformity of ribbon properties across ribbon width using a large scale of roller compactors; most of the uniformity related studies had been conducted using lab-scale roller compactors. Alleso et al. (2016) showed a non-uniform porosity distribution across the ribbon width using 100 mm wide rollers under different roller force and roller gap. They also mentioned that the cause could be from the feeding process.

Overall, the non-uniformity of ribbon property results from the non-uniform feeding powder distribution. No method has been explained in the literature to improve powder flow in the feeding stage to achieve uniform powder distribution. The concave-convex/rimmed rollers were used in order to compact more powder at the sides of rollers; however, the concave-convex rimmed rollers were not adjustable to design for a range of materials (Funakoshi et al., 1977). Therefore, it is necessary to develop a method covering a range of materials to improve and achieve uniform powder distribution in the compaction stage.

Effect of roller force / hydraulic pressure on ribbon properties

In the roller compaction, the force from the rollers strongly influences the properties of the products, such as the temperature of ribbon surface and the porosity of the ribbon (Al-Asady et al., 2015, Omar et al., 2015). During the compaction process, particles could be deformed or fractured under stress. The deformation and the fracture of the particles could generate heat in addition to the interparticle and wall friction. The increasing stress results in the growth of heat generation during compaction process (Yu et al., 2018, Al-Asady et al., 2016, Omar et al., 2015, Osborne et al., 2013). More heat is generated when the higher pressure was applied. Omar et al. (2015) and Al-Asady et al. (2016) suggested that the increasing hydraulic pressure resulted in an increase of maximum temperature of ribbon surface, which was monitored by the online thermal imaging.

Furthermore, porosity and density of the ribbon are influenced by hydraulic pressure from the roller. High compaction pressure results in high density or low porosity of ribbons and vice versa (Omar et al., 2015, Khomane and Bansal, 2014, Bacher et al., 2007). A study conducted by Al-Asady et al. (2015) also demonstrates the same trend using six different materials, as shown in Figure 2-14.

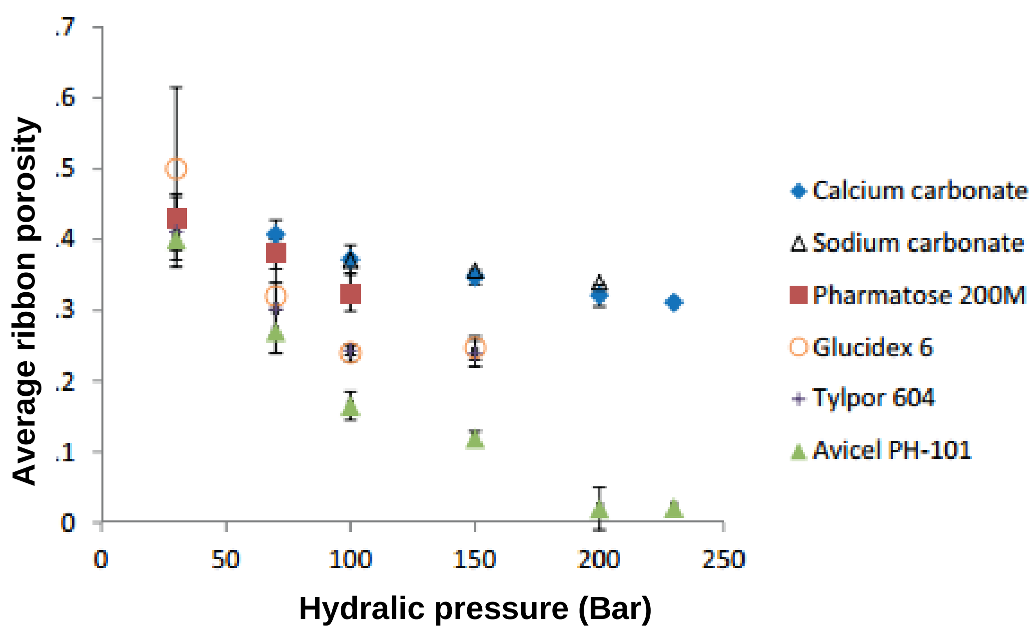

Figure 2-14: Effect of hydraulic pressure on ribbon porosity (Al-Asady et al., 2015).

2.3.2 Predictive models for roller compaction

2.3.2.1 Johanson's theory

Johanson (1965) developed the first model to predict the maximum roller pressure and pressure distribution. In this model, there are three regions in the compaction: slip region, nip region and release region, as shown in Figure 2-15. Johanson theory enables to calculate the nip angle and maximum normal stress based on material properties such as compressibility factor, angle of wall friction, internal friction angle and dimension of rollers such as roller diameter. In this model, the material was assumed to be isotropic, frictional, compressible and cohesive and it follows the effective yield function which is proposed by Jenike and Shield (Jenike and Shield., 1959).

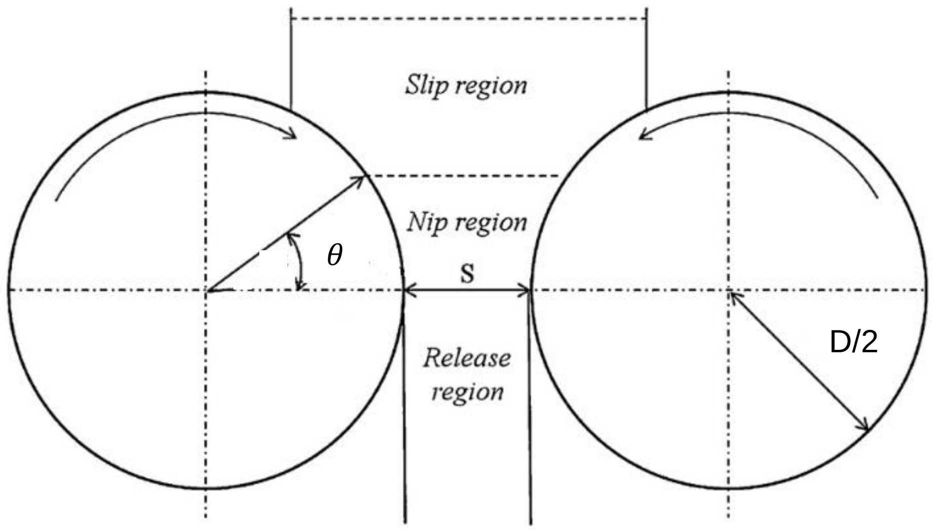

Figure 2-15. Regions proposed in Johanson theory (Johanson, 1965).

Johanson's theory presented the calculation steps of stress gradient by the following equations. The stress gradient for slip region condition is given by

$$\left(\frac{d\sigma}{dx}\right)_{slip} = \frac{4\sigma\left(\frac{\pi}{2} - \theta - v\right) tan\, \theta_e}{\frac{D}{2}\left[1 + \frac{S}{D} - cos\, \theta\right]\left[cot(A - \mu) - cot(A + \mu)\right]} \qquad \text{Eq (4)}$$

where σ is the normal stress the powder;

x is the distance gradient starts from the minimum roller gap;

θ_e is the effective angle of internal friction;

S is the roller gap;

D is the roller diameter;

μ is the Johanson theory parameter given by

$$\mu = \frac{\pi}{4} - \frac{\theta_e}{2} \qquad \text{Eq (5)}$$

v is the acute angle between the tangent to the roller surface, and the direction of the major principal stress is given by

$$2v = \pi - arcsin\frac{sin\,\Phi_w}{sin\,\delta} - \Phi_w \qquad \text{Eq (6)}$$

where Φ_w is the angle of wall friction;

θ is the angular position at the roller surface, for instance, θ=0, which means at the minimum gap, the A is given by

$$A = \frac{\theta + v + \frac{\pi}{2}}{2} \qquad \text{Eq (7)}$$

The stress gradient for the nip condition is given by

$$(\frac{d\sigma}{dx})_{nip} = \frac{K\sigma_\theta\left(2\cos\theta - 1 - \frac{S}{D}\right)\tan\theta}{\frac{D}{2}\left[\frac{d}{D} + \left(1 + \frac{S}{D} - \cos\theta\right)\cos\theta\right]} \qquad \text{Eq (8)}$$

where the K is the compressibility factor;

σ_θ is the mean normal stress at position θ.

d is the thickness of the compacted materials at the minimum roller gap.

Johanson (1965) proposed that stress gradient in the slip and nip regions are equal at the nip angle in Eq (9) and further calculated by using Eq (4) and Eq (8).

$$\left(\frac{d\sigma}{dx}\right)_{slip} = \left(\frac{d\sigma}{dx}\right)_{nip} \qquad \text{Eq (9)}$$

When the stress distribution between rollers is known,

$$Rf = P_m WDF/2 \qquad \text{Eq (10)}$$

where Rf is the roller force;

P_m is the maximum stress on the powder;

W is the roller width;

F is the roller force factor given by

$$F = \int_{\theta=0}^{\theta=\alpha} [\frac{(d+S)/D}{\frac{d}{D} + (1 + \frac{S}{D} - \cos\theta)\cos\theta}]^K \cos\theta \, d\theta \qquad \text{Eq (11)}$$

Bi et al. (2014) and Muliadi et al. (2012) found that Johanson's rolling model overpredicted the maximum roll surface pressure. The reason is that the effects of velocity gradient had not been taken into consideration by the Johanson model, and the mass of material was over-predicted (Muliadi et al., 2012). Bi et al. (2014) also argued that inadequate assumption had been corrected by a new term defined as "mass correction factor".

2.3.2.2 Slab model

The slab method was proposed by Katashinskii (1966), which is used for predicting the stress distribution of compressing metal powder by rollers. Same as the Johanson model, plane sections are assumed as they pass through the rollers. The slab model split the deformation zone between the two rollers into trapezoidal slabs. In this method, yield criterion for fully dense metal was proposed to use in order to develop the material model (Dec et al., 2003, Kuhn and Downey, 1971). Dec et al. (2003) carried out the validation of the slab model by using an instrumented roller to measure the stress. They mentioned that not all of the predicted values from the model agreed with that from the experiments.

An equilibrium equation of the stress in the x direction was obtained from the force balance on the slab, and expressed as:

$$\frac{d(t\sigma_x)}{d_x} + 2(p \tan \alpha_x - \tau_f) = 0 \qquad \text{Eq (12)}$$

where, σ_x is the stress along the x direction;

t is the thickness of the slab;

p is the normal pressure on the layer;

α_x is the instantaneous angle;

τ_f is the frictional stress, and it could be expressed as:

$$\tau_f = Y(\rho)\text{: for } \mu(p)p \geq \tau_f = Y(\rho) \qquad \text{Eq (13)}$$

$$\tau_f = \mu(p)p \text{ : for } \mu(p)p < \tau_f = Y(\rho) \qquad \text{Eq (14)}$$

where $Y(\rho)$ is the yield stress as a function of the slab density which can be determined from compression test of the powder and $\mu(p)$ is the coefficient of friction which can be obtained by the annular friction tester (Dec et al., 2003).

2.3.2.3 Finite element model

The finite element model (FEM) has been used in the roller compaction process to investigate the effects of feeding pressure, roller speed, nip angle and wall friction coefficient since past years. The finite element model (2D and 3D) was performed with using ABAQUS package (Krok and Wu, 2019, Mazor et al., 2018, Mazor et al., 2016, Muliadi et al., 2013, Cunningham et al., 2010, Dec et al., 2003). The constitutive model of powder was used in the simulation, which is based on the pressure-dependant yielding plasticity model (modified Drucker–Prager/Cap model) with linear elasticity. The model was calibrated by mechanical tests, such as diametrical compression, instrumented die compression and uniaxial compression.

Dec et al. (2003) compared the finite element model with Johanson model and slab model in terms of the process design, prediction of the nip angle and stress distribution. The finite element model results showed that feed stress (constant stress applied at the inflow boundary in the rolling direction) had a significant effect on the maximum roller stress generated, as displayed in Figure 2-16. They also mentioned that the important part was the calibration of the material model, feeding process and tool geometry (roll surface), which contributed to a potential of realistic analysis of the compaction process and with appropriate visualisation of the results to design and control.

Cunningham et al. (2010) developed a 2D and 3D finite element model and compared with the experimental results by using an instrumented roller. Some assumptions were made in the simulation, such as ignored effect of interstitial air, ignored deformation of rollers and stress by the screw feeder. The results illustrated that oscillating feed stress conditions revealed periodic variations in roll pressures and relative densities. The 3D model predicted lower roller pressure and lower densities near the edges (non-uniform distribution across the roller width) because of the friction between the powder and side-sealing cheek plate. In addition, they also mentioned that variable inflow of material along the roll width was related to variation in roll pressure and the model predictions agreed with experimental results' trends.

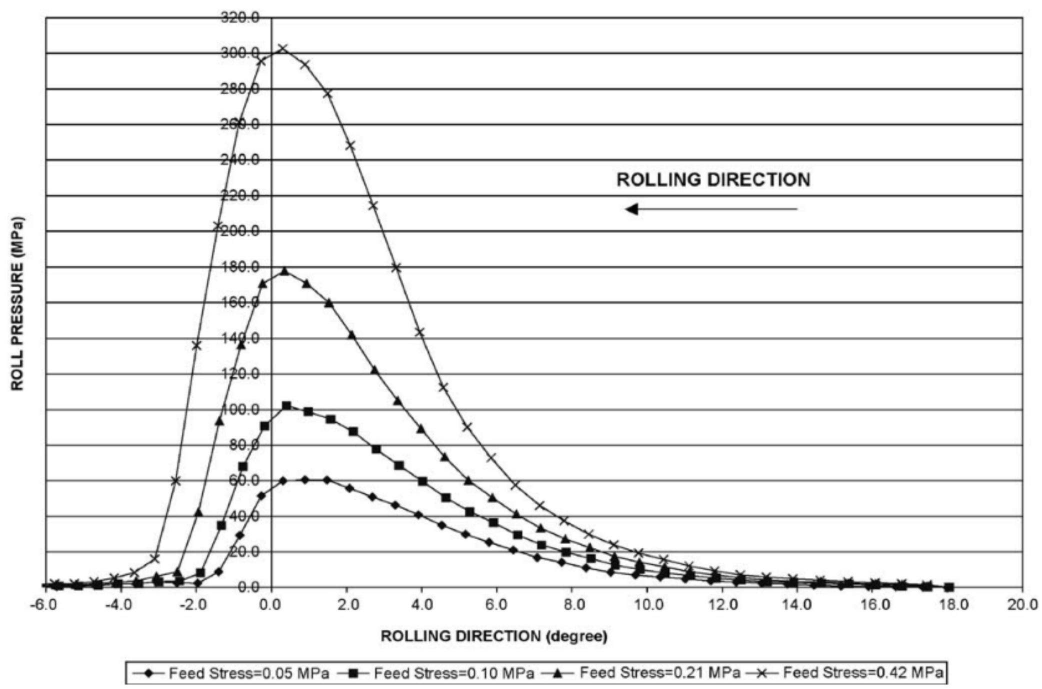

Figure 2-16. Effect of the feeding stress on the maximum roller pressure (Dec et al., 2003).

Moreover, Muliadi et al. (2013) used an air-powered piston feeder configuration that applied known uniform stress on the powder in the experimental study, which is different from the previous other works. Then, they developed a 3D FEM simulation which compared the density results with the experimental trend. The simulation predicted the density distribution results independent of the inlet stress, which agreed with the experimental work. However, Muliadi et al. (2013) mentioned some shortcomings of the current simulation. For example, the mesh density required for stable computations was inversely proportional to the roll gap, and performing simulations with insufficient mesh density were found to result in unrealistic discontinuities in the yield (densification) paths, zero plastic strain results at the roll gap because of significant deformation. Also, the explicit Adaptive Lagrangian–Eulerian (ALE) scheme employed was unsuitable for capturing the elastic spring-back that the ribbons may exhibit from the minimum roller gap (Muliadi et al., 2013).

Furthermore, in a more recent study, Krok and Wu (2019) developed a FEM method, which predicted the thermo-mechanical behaviour of powders during roller compaction (gravity feeding). The non-uniform temperature and relative density distribution across the ribbon width due to the wall friction were predicted by FEM, which matched with the experimental results (Krok and Wu, 2019). The results showed that the temperature and relative density were higher at the ribbon centre than that at the sides of the ribbon. Moreover, Mazor et al. (2018) developed a method by using the results (particle velocity) from DEM as an input in the FEM simulation in order to investigate the effect of the inhomogeneous inlet feeding velocity due to the rotating screw feeder. The results illustrated the inhomogeneous roller contact pressure and relative density across the ribbon width.

2.3.2.4 Discrete element model

The Discrete Elements Model is another numerical method recently used in the feeding and compaction zone of roller compaction process, in which it commonly used spherical particles (Mazor et al., 2018, Odagi et al., 2001). Mazor et al. (2018) stated that the interaction among particles was influenced by external force fields according to an interaction law.

Odagi et al. (2001) concluded the results with 2D simulation, which was displaying the particle velocity distribution in the gravity (vertical) feeding zone until the exit of the roller gap. They stated that the particle velocity was increasing when they were moving towards the roller surface. Furthermore, Mazor et al. (2018) developed a 3D simulation successfully to model the behaviour of particles in the feeding zone (horizontal screw feeding) and the highly inhomogeneous velocity field at the interface between the screw feeder and the compaction region. Although the DEM model was employed to model the particle flow behaviour in the feeding zone of the roller compaction process, it was not suitable to model the compaction process due to the deformation not being presented (Mazor et al., 2018).

2.4 Summary

2.4.1 Non-uniform powder feeding and ribbon properties in roller compaction

Previous experimental studies have shown that non-uniform powder distribution, which exists in the powder feeding zone of the roller compaction, is mainly caused by the friction between the powders and cheek plates (Miguelez-Moran et al., 2009).

This resulted in the non-uniformity of ribbon properties across the ribbon width, which has also been investigated by various predictive models (Mazor et al., 2016).

Although the concave-convex/rimmed rollers were used in previous studies to reduce the friction effect and improved the uniformity of pressure and relative density across ribbon width, the methods still had drawbacks: (1) the approaches of concave-convex/rimmed rollers did not fully consider the main cause of the non-uniform powder distribution arisen from the feeding to the compaction zone; (2) the designs of concave-convex/rimmed rollers only involve three specific ‘’rim wall angles’’ for limited numbers of material to achieve relatively uniform pressure across the width (Funakoshi et al., 1977), which can be expensive and non-flexible to build for a range of materials; (3) the approaches considered the effects on the uniformity of ribbon properties with a limited number of materials and process parameters (Mazor et al., 2016, Perez-Gandarillas et al., 2016, Funakoshi et al., 1977). Additionally, the usage of lubrication materials can help improve the powder uniformity to some extent, but the formulation and final product quality can be affected due to the amount of usage.

A range of practical and replaceable elements can be designed in the feeding zone to improve the uniformity of powder distribution and ribbon property across the width regarding the different powders’ properties and roller forces. This concept will be focused in this study for lab-scale roller compactor, which can also be verified in the pilot-plant scale roller compactor.

2.4.2 Online monitoring as PAT applied in roller compaction

Several PAT tools have been used to monitor the powder/ribbon properties in the roller compaction process. PIV was utilised to investigate the powder flow behaviour along feeding to compaction direction, which required considerations of preparation of traced particles and mixing process. While, online thermal imaging was used to directly monitor and capture the ribbon surface temperature across the width, as the ribbon exited from the minimum roller gap. The temperature of powder along the feeding to the compaction zone can also be online monitored by a new modified method with a specially designed cheek plate allowing NIR radiation to be seen through, which will be developed in this study. Also, a new method can be used to understand and compare the powder temperature along the direction from feeding to compaction (including the temperature at and after the minimum roller gap) and across the ribbon width.

Chapter 3 Materials and methodology

3.1 Materials preparation

Materials are used in this study, as listed in Table 3-1. Powder true densities are from manufacturers. Those materials cover a range of flowability from poor flowing to free flowing. Pharmatose ® 200 M - Lactose monohydrate is commonly used as filler and additive in pharmaceutical and food industries, and it is a brittle material (Omar et al., 2015). Avicel ® PH 101 Microcrystalline Cellulose (MCC) is an ideal excipient for use in dry granulated formulations which shows excellent compaction and disintegration properties (Rajkumar et al., 2019). Starch 1500 is the most widely used pregelatinized starch and used mainly for compression and capsule filling (Rojas. et al., 2012). Tylopur ® 603 Hydroxypropyl Methylcellulose (HPMC) is easy to use as film-forming agent, and there is no interaction with the active ingredient and soluble in water or organic solvents (Foroughi-Dahr et al., 2019). Light Sodium Carbonate known as soda ash, is an alkaline additive used in the dairy industries (Tao et al., 2019). GLUCIDEX ® Maltodextrin DE6 is an odourless, white powder with a dextrose equivalent value (DE) of 6. It serves as a texturizer, a powder carrier, suitable for a variety of applications, including soups and cereals (Hull, 2010).

Before measurement of powder properties, powders are conditioned in the humidity chamber (KMF 240 climatic chamber, Binder, UK) at 20 °C, 40 % and 60 % of relative humidity for 72 hours (Yu et al., 2018, Omar et al., 2016).

Table 3-1: Powder used in this study.

Powder names and types	Supplier	True density (kg/m^3)
Pharmatose ® 200 M Lactose monohydrate	DFE Pharma, Netherlands	1540
Avicel ® PH 101 Microcrystalline cellulose (MCC)	FMC BioPolymer, USA	1561
Starch 1500	Colorcon, USA	1490
Tylopur ® 603 Hydroxypropyl methylcellulose (HPMC)	Shin-Etsu, Japan	1285
Light Sodium Carbonate	Tata Chemicals Europe, UK	2533
GLUCIDEX ® Maltodextrin DE6	Roquette, France	1440

3.1.1 Particle size and size distribution

The primary particle size is determined using Camsizer XT (Retsch Technology GmbH, Germany), which operates based on image analysis. The equipment uses compressed air to disperse particles which ensure to record a single particle. Value of D_{10}, D_{50} and D_{90} of primary particle size distribution for different materials are listed in Table 3-2.

Table 3-2: Particle size distribution of different primary powders.

Material	D_{10} (µm)	D_{50} (µm)	D_{90} (µm)
Pharmatose ® 200 M Lactose monohydrate	10.3	37.9	92.4
Avicel ® PH101 MCC	20.9	44.5	76.0
Starch 1500	17.7	60.7	134.4
Tylopur ® 603 HPMC	23.9	64.3	124.7
Light Sodium Carbonate	16.1	72.5	182.9
GLUCIDEX ® Maltodextrin DE6	19.9	91.9	227.6

3.1.2 Particle morphology

The particle morphology of six materials are examined by scanning electron microscopy (SEM) - JEOL IT100 (JEOL, Japan) as shown in Figure 3-1. It can be seen that Avicel ® MCC PH101 and Tylopur ® 603 HPMC are fibrous and elongated particles. The shape of Light Sodium Carbonate and Maltodextrin particles are angular with flat surface compared to the other types of materials. While particles of Starch 1500 are relatively most spherical shape.

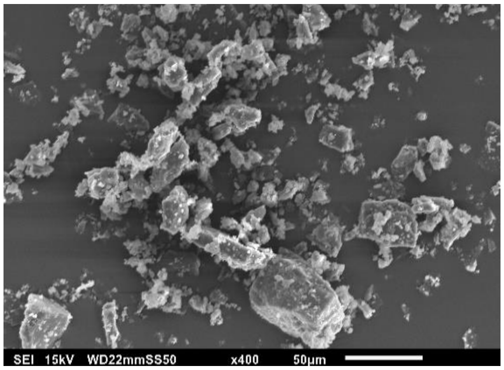

Pharmatose 200M

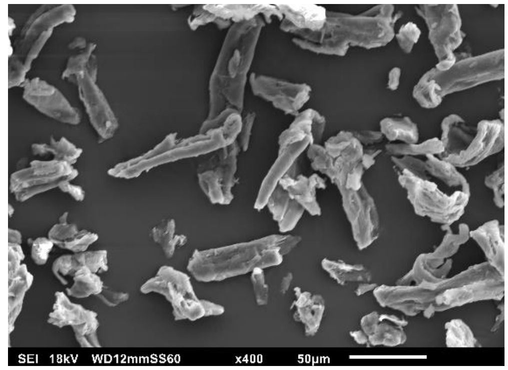

Avicel ® PH 101 MCC

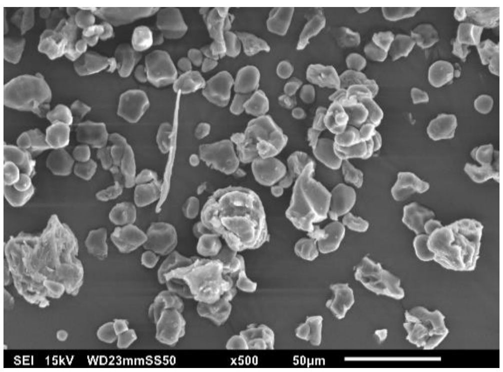

Starch 1500

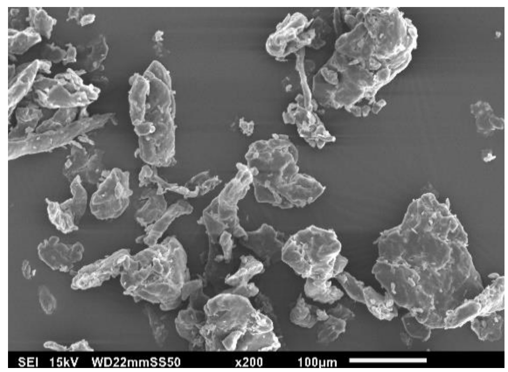

Tylopur 603 ® HPMC

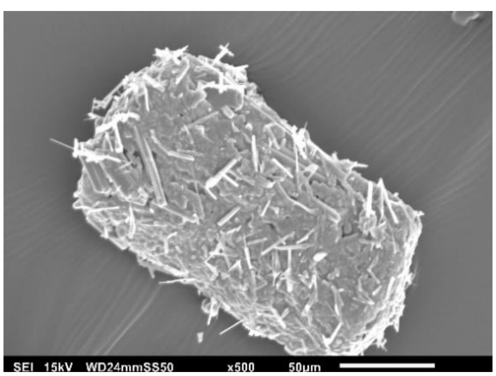

Light Sodium Carbonate

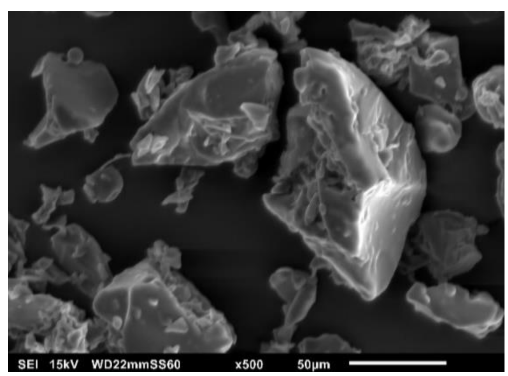

Maltodextrin DE6

Figure 3-1: Particle morphology by scanning electron microscopy (SEM).

3.1.3 Angle of repose

Measuring the angle of repose is one method to test powder flowability. The tester (Mark 4 Powder Research, UK) was used to measure the angle of repose. Powder (50 g) gradually falls from a fixed height (30 cm) onto a horizontal platform with scale. The angle between the slope of the heap of the powder and the horizontal platform is determined using Eq (1).

3.1.4 Flow function coefficient and effective angle of internal friction

Ring Shear Testers RST-XS (Dietmar Schulze, Germany) is used for the determination of the flow properties of powders, such as flow function coefficient, internal friction angle and angle of wall friction. The test is to apply a load on the powder to consolidate (pre-shear), then shear the consolidated powder to failure at different normal stress levels which is less than pre-shear stress as shown in Figure 3-2 (a). The yield limit of consolidated powder is also named a yield locus. Mohr stress circle is used to characterise the normal and shear stress when the consolidated powder is sheared at steady-state flow, as shown in Figure 3-2 (b). The major principal stress σ_1 is regarded as the consolidation stress for the yield locus, and unconfined strength σ_c is the compressive strength from the yield locus (Schulze, 2007). The consolidation stress σ_1 and unconfined strength σ_c are used to carry out the flow function coefficient (ffc) in Eq (15). A straight line through the origin of the σ, τ diagram, tangent to the larger Mohr circle (steady-state flow), is the effective yield locus. The slope of the effective yield locus is called the effective angle of internal friction, θ_e (Schulze, 2007). During the measurement, the maximum preload used is 8000 Pa, and the minimum is 30% of the maximum pre-shear in the shear cell based on the application of a range of materials (Schulze, 2007).

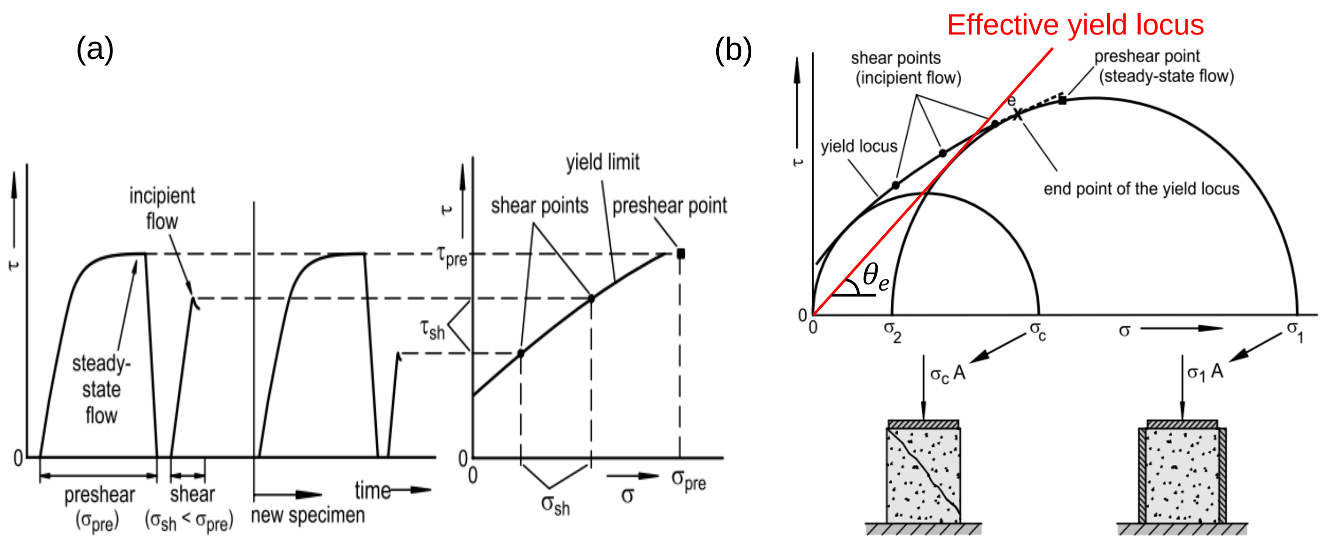

Figure 3-2: Determination of yield limit, consolidation stress σ_1 and unconfined strength σ_c : (a) Determined yield limit from measured shear stress; (b) consolidation stress σ_1 and unconfined strength σ_c determined by yield locus and Mohr stress circle (Schulze, 2007).

$$ffc = \frac{\sigma_1}{\sigma_c} \qquad \text{Eq (15)}$$

where σ_1 is the consolidation stress;

σ_c is the unconfined strength.

3.1.5 Angle of wall friction

In the measurement of wall friction angle, the annular bottom ring contains a sample of the wall material to be tested as shown in Figure 3-3. During the test, a normal force is applied to the bulk powder, which creates the vertical wall normal stress acting between the bulk powder and the wall material sample. To measure wall friction, the shear cell rotates in a direction, while the lid is prevented from rotating by the two tie rods, as shown in Figure 3-3. The bulk powder is moved across the surface of the wall material sample while it is subjected to normal stress. The forces acting on the tie rods (F_1, F_2) are proportional to the wall shear stress (τ_w) (Schulze, 2007).

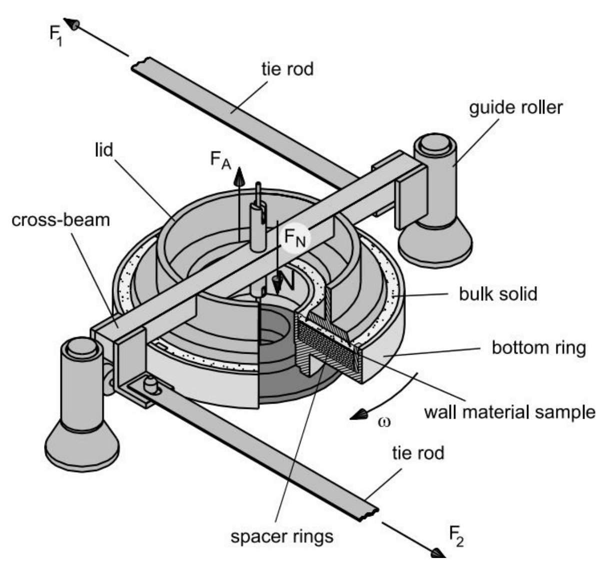

Figure 3-3. Measuring the angle of wall friction with Ring Shear Testers RST-XS (Schulze, 2007).

To quantify wall friction, the coefficient of wall friction (μ_w) and the wall friction angle (φ_x) are used (Schulze, 2007). The coefficient of wall friction, μ_w, is defined as the ratio of wall shear stress (τ_w) to wall normal stress (σ_w) for a point on the wall yield locus shown in Figure 3-4, by following:

$$\mu_w = \frac{\tau_w}{\sigma_w} \qquad \text{Eq (16)}$$

where μ_w is the coefficient of wall friction;

τ_w is the wall shear stress;

σ_w is wall normal stress.

The wall friction angle φ_w is the slope of a line running from the origin of the τ_w, σ_w diagram to a point on the wall yield locus as displayed in Figure 3-4:

$$\varphi_w = \arctan\left(\frac{\tau_w}{\sigma_w}\right) \qquad \text{Eq (17)}$$

where φ_w is the angle of wall friction.

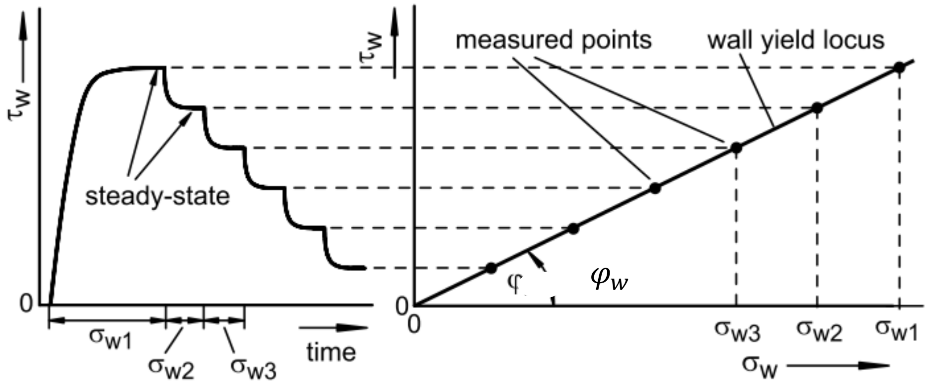

Figure 3-4. Measuring steps of wall friction (Schulze, 2007)

In this study, in order to measure the wall friction, there are two types of wall plates (knurled steel wall plate and POM-C (Polyoxymethylene copolymers) wall plate) built for the Ring Shear Cell as shown in Figure 3-5. Knurled steel plate is built using the same material and surface pattern as the rollers in the roller compactor, which is used for measuring the friction between the roller surface and different powders. Moreover, POM-C plate is built using the same material as the side-sealing cheek plate in the roller compactor, which is used for measuring the friction between the side-sealing cheek plate and different powders. POM-C is a semi-crystalline thermoplastic with high mechanical strength and rigidity. Also, it has good sliding characteristics, excellent wear and chemical resistance and low moisture absorption (Gerdeen and Rorrer, 2011). That is also the reason for the side-sealing cheek plate in the roller compactor.

Knurled steel wall plate

POM-C wall plate

Figure 3-5. Wall plates of Knurled steel and POM-C for Ring shear cell.

3.1.6 Compressibility factor of powder

The compressibility factor of powder is determined by compacting a sample of 0.3 g with a pressure range of 15–200 MPa in a die with internal diameter 10.5 mm by using a testing machine (MTS 810, USA) constant compression rate of 10 mm/min. Then the out-die volume of the compact (tablet) and the weight are measured for each pressure, and the compressibility factor (K) is determined from the logarithmic plot of the pressure versus bulk density and according to Eq (18).

$$log\frac{p_1}{p_2} = K\,log\frac{\rho_1}{\rho_2} \qquad \text{Eq (18)}$$

where p is the pressure (p_1 and p_2 correspond to two values of pressure);

ρ is the bulk density of powder ($\rho_1$and ρ_2 correspond to the bulk density of powder after applying the pressure of p_1 and p_2).

3.2 Roller compaction

The roller compactors used are Alexanderwerk WP120 Pharma and WP200 Pharma (Alexanderwerk AG, Germany), as shown in Figure 3-6. The detailed sketch is seen in Figure 3-7. The vertical feeding hopper is on the top left of rollers, and a clock-wise rotating stir is at the bottom of the hopper. Next, the horizontal screw feeding is clock-wise rotating. The screw feeder carries the powder to the filter zone with speed at range from 18.7 to 80 rpm. A vacuum system is suited at the end of the screw and next to the rollers. The two counter-rotating rollers are vertically parallel to each other with the knurled surface.

The roller diameter is 120 mm for WP120 Pharma and 200 mm for WP200 Pharma. The roller width is 40 mm for WP120 Pharma and 75 mm for WP200 Pharma. The roller gap is changeable from 1 to 4 mm. The upper roller is moving to apply force from 8.29 to 95.38 kN for WP 120Pharma and from 15.54 to 178.83 kN for WP200 Pharma. The conversion between hydraulic pressure and roller force is shown in Appendix 3. There is a flake chopper with 6 blades which rotates anti-clockwise at 100 rpm. The compacted materials coming from flake chopper will go through the crushers. The crushers have 6 blades which rotate clockwise with speed from 24.7 to 107.3 rpm.

WP120 Pharma WP200 Pharma

Figure 3-6. Alexanderwerk WP120 Pharma and WP200Pharma roller compaction (Alexanderwerk AG, Germany).

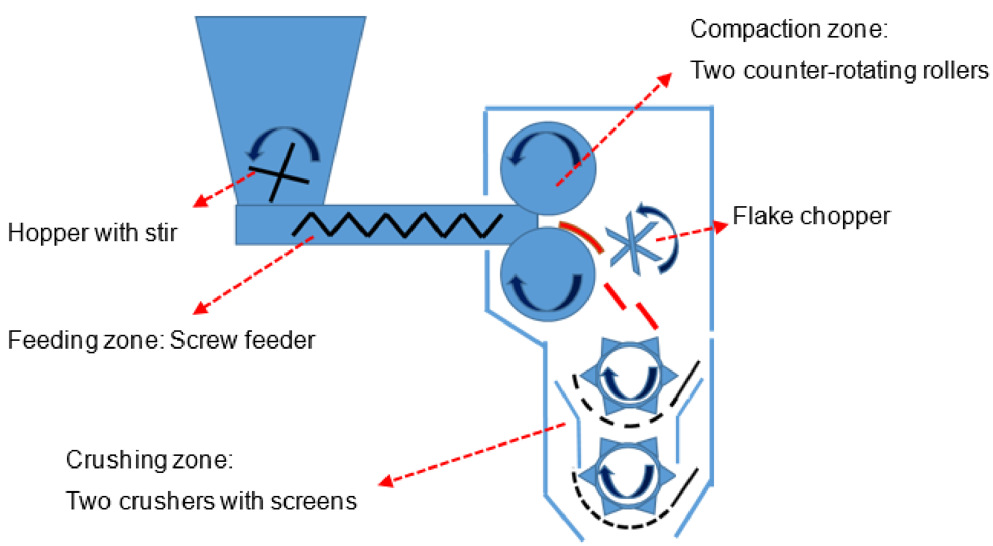

Figure 3-7. Sketch of roller compaction process: feeding, compaction and crushing stage.

The process parameters used in the entire study are roller speed with 3 rpm; roller gap with 2 mm; roller force with a range from 8.29 kN to 49.76 kN (WP120 Pharma) and from 15.9 kN to 93.3 kN (WP200 Pharma). At the same, all experiments are carried out with an automatic gap control system. The automatic gap control means that the screw speed is changing according to the required roller gap.

3.2.1 Nip angle and maximum normal stress from Johanson theory

As detailed explained in the Chapter 2.3.2.1, Johanson (1965) developed the first model to calculate the nip angle and maximum roller stress based on material properties such as compressibility, wall friction angle and internal friction angle. In this study, Johanson theory was used to calculate the nip angle and the maximum normal stress on the powder (step details explained in section 2.3.2.1) (Johanson, 1965). Thus, a range of stress applied on the powder, in which stress is different because of compressibility factor, material flow properties and roller diameter.

3.2.2 Process analytical technology - online thermal imaging in roller compaction

In the roller compaction process, as the powder is under the stress that results in heat generation. The online thermal imaging could represent the temperature of powder and ribbon in the roller compaction that is carried out by using the thermal camera FLIR A655sc (FLIR, Sweden). The recording frame rate is 50 f/s, and the thermal image has 640 x 480 pixels. The camera is connected to the laptop that shows the thermal images when the recording triggered. The analysis tools – FLIR software, are capable of calibrating the temperature to different emissivity and also to measure the temperature on the images at any point. The emissivity is in the range from 0 to 1 (1 is the ideal blackbody) according to Stefan–Boltzmann law (Brownson, 2014). The calibration of emissivity is carried out that the samples were conditioned in the chamber for 12 hours at 60 °C (Yu et al., 2018, Omar et al., 2015). The thermal camera is used to measure the temperature of the selected area on the sample; meanwhile, the thermometer is used to measure the actual temperature of the sample. The FLIR software calibrates these temperatures to get the emissivity. The table of emissivity for different materials used in this study is displayed in Appendix 4.

3.2.2.1 Determining the temperature across the width of ribbon in roller compaction

As powders are compressed under the stress in the compaction zone, heat is generated. The different amount of heat is generated because of the different mechanic properties of the powder and the different amount of powder fed to the compaction zone. Determining the temperature across the ribbon width is a way to investigate the ribbon properties across the width.

In this method, Figure 3-8 shows thermal camera faces to the direction of ribbon exiting from roller gap, and the setup of the thermal camera is at the same height in front of the recently produced ribbon. The distance between the ribbon and the camera is kept constant at 30 cm (focus distance). During the experiments, roller force and roller gap reach required constant value, video of thermal imaging is recorded for 3 minutes. The experiments are repeated five times when rollers and screw feeder cool down to the room temperature (20°C) which is monitored by the thermal camera.

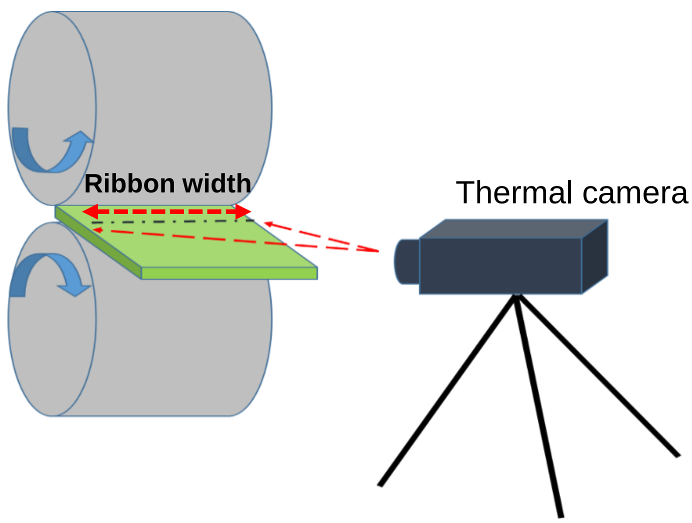

Figure 3-8. Thermal imaging to determine ribbon temperature across the width.

Relative temperature uniformity across the ribbon width

As the temperature of the ribbon surface is measured across the ribbon width, there is a need to determine the value of uniformity. Thus, the relative temperature uniformity is defined as

$$Relative\ temperature\ uniformity = \frac{L}{RW} \times 100\ \% \qquad \text{Eq (19)}$$

where L is the corresponding length of the uniform temperature section from the temperature profile (the difference between the maximum and the nearby temperature is less than the average deviation of temperature) (Omar et al., 2019);

RW is the complete ribbon width.

The deviation of temperature (δ) across the ribbon width was calculated using,

$$\delta_{Temp} = \frac{T_{max} - T_{min}}{T_{ave}} \qquad \text{Eq (20)}$$

where T_{max} is the maximum temperature of the profile across the ribbon width;

T_{min} is the minimum temperature of the profile across the ribbon width;

T_{ave} is the average temperature of the profile across the ribbon width.

3.2.2.2 Thermal imaging of powder temperature from feeding to compaction zone in roller compaction

As the powder is fed towards the compaction zone, the powder is flowing under stress from rollers. The purpose is to determine the change of powder temperature from the feeding to the compaction zone. For this purpose, a modified design cheek plate was built with two Germanium thermal glass windows with a DLC coating (Umicore company) with a transmission rate of 98 %. The dimension (Length x Height) of Window 1 is 35 mm x 20 mm, and Window 2 is 35 mm x 10 mm. The thermal camera 1 is positioned in front of the modified cheek plate at the same level of the screw feeder to monitor the powder temperature along the feeding direction to the compaction zone as shown in Figure 3-9 and Figure 3-10. While the thermal camera 2 is positioned normal to the ribbon production direction to monitor the ribbon surface temperature, as displayed in Figure 3-10. Once the feeding begins, the recording starts and lasts for 3 minutes. Also, the experiments are repeated five times when the screw feeder and rollers cool down to the room temperature (20°C) which is monitored by the thermal camera.

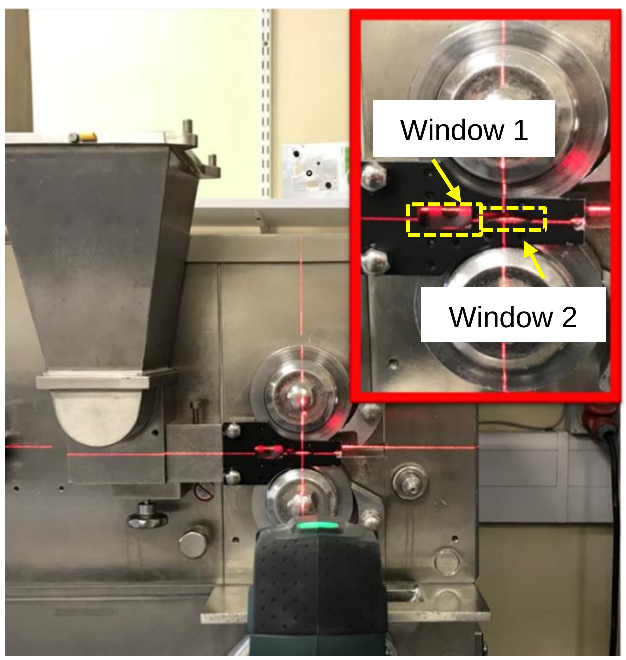

Figure 3-9. Thermal imaging from feeding to compaction zone and the focus area of two thermal windows (yellow squares).

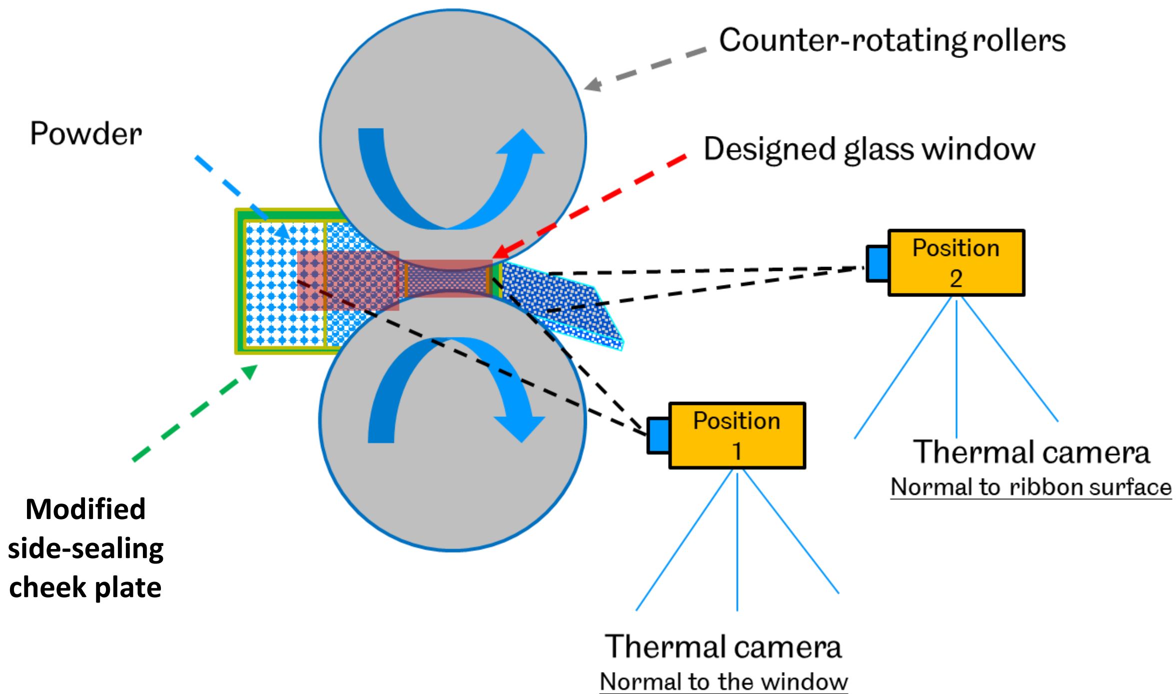

Figure 3-10. Thermal imaging from feeding to compaction zone and across the width of the ribbon surface.

3.2.3 Off-line measurement of the ribbon properties from roller compaction

As the ribbons are produced from the compaction process, the ribbon properties could be measured offline, such as porosity by X-ray. The porosity of ribbon is measured by using the X-ray tomography scanner - µCT 35 (SCANCO MEDICAL, Switzerland) that offers scanned images of the sample. The data is carried out by using Image J software.

3.2.3.1 Porosity distribution across the ribbon width from roller compaction

The X-ray passes through ribbon samples, as shown in Figure 3-11 (a). The ribbon samples were from the same batch in the thermal imaging experiments. The slice of ribbon sample is 5 mm on the ribbon length direction with full width that is measured at different symmetrical positions across the width. For instance, the scanned ribbon sample from WP120 Pharma is with one position for the centre, two positions for both between centre and side, and two positions for both sides (edges), as seen in Figure 3-11 (a). These include 233 scanning slices for each position from top to bottom. The scanned ribbon is as shown in Figure 3-11 (b), the white spot presents the solid of the ribbon while the black spot represents void.

The porosity is the ratio of the void area and the total area based on the measured parts of the ribbon. In each scanned slide, there is a fixed black area (4 x 1.5 mm) around the sample, which is used to be calibrated as a value of 99.99% (void area) by using Image J software. At the same time, the software will carry out a value of the void area on the measuring area (4 x 1.5 mm), as shown in Figure 3-11 (b). The porosity is then calibrated by measuring the porosity of the tablets in the same X-ray scans (the same material with known density and tablet produced from compressibility test in Section 3.1.6). When one scan section of sample finishes, the sample will be moved up for the next section of scanning.

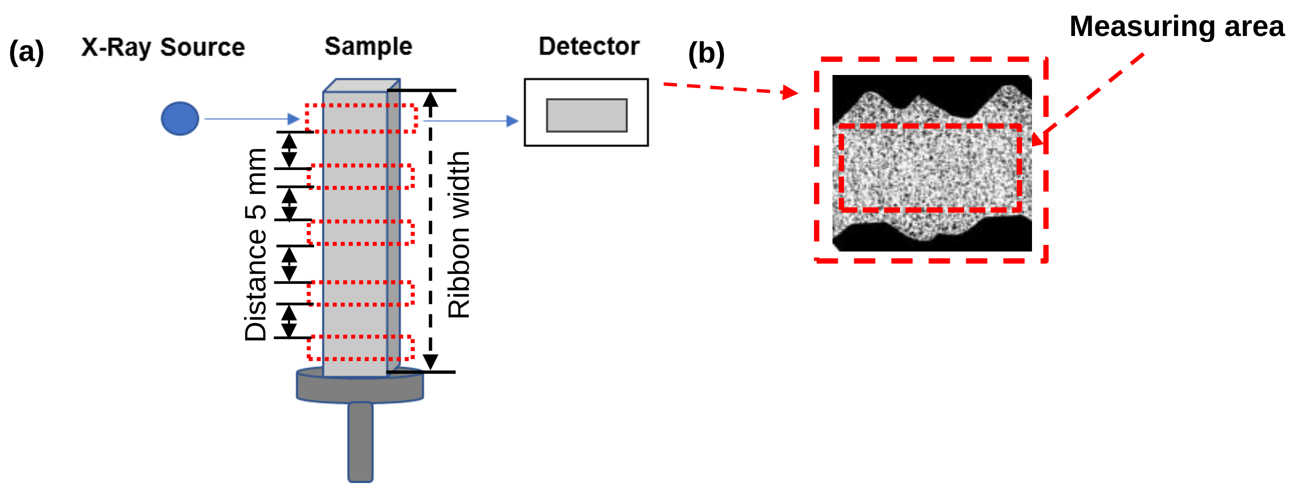

Figure 3-11. X-ray scanning method across the ribbon width.

The density can be calculated with the porosity (from X-ray results) and true density of powder (from powder manufactures) by Eq (21) (Litster and Ennis, 2004):

$$\varepsilon_p = 1 - \frac{\rho_{ribbon}}{\rho_{true}} \qquad \text{Eq (21)}$$

where ε_p is the porosity of the ribbon;

ρ_{ribbon} is the density of the ribbon;

ρ_{true} is the true density of powder.

3.2.3.2 Porosity distribution of compacted body along feeding to compaction direction from roller compaction

In this method section, samples are from the same batch of ribbons in the thermal imaging experiments. The compacted powder body is continuously scanned by plane through the centreline across the ribbon width and normal to the feeding to the compaction direction, as seen with X-ray image in Figure 3-12 (a), and the optical image by microscope (Keyence VHX5000) in Figure 3-12 (b).

The maximum scanning diameter of the sample holder is 37 mm. The samples of the compacted body were with different length because of the strength of the compacted body under difference roller forces. Calibration is carried out in the same method described in Section 3.2.3.1. Each measurement includes 233 slices and 10 continuous scans are carried out for each sample, as shown in Figure 3-12.

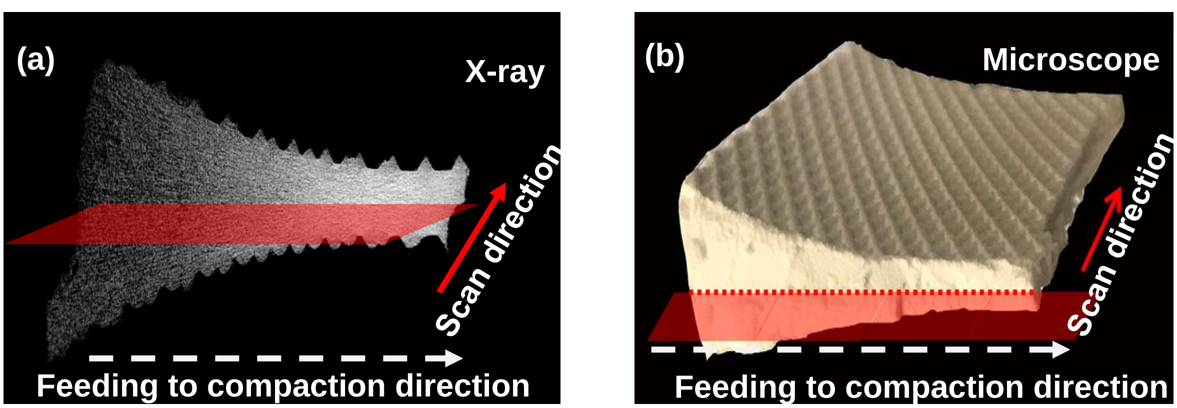

Figure 3-12. Scanning compacted powder sample along feeding direction: (a) Scanned image from X-ray; (b) Optical image from Microscope.

Chapter 4 Preliminary study of powder flow with newly designed setups

4.1 Introduction

Effective powder flow is crucial for the powder processing steps. Different powders have different flow properties, which is also influenced by other factors, such as relative humidity condition.

In this Chapter, the study will focus on how powder flows while discharging and investigate the methods to improve the distribution of powder flow using different new designs.

4.2 Methodology

4.2.1 Preparation of powders

Before each experiment, all powders were stored and conditioned in the humidity chamber at 20°C, 40% and 60% of relative humidity for 72 hours (equilibrium condition).

4.2.2 Design of new guiding setups for improving powder flow

The flowability of any powder in a system depends on some properties of the powder and the interaction with the stationary container/surrounding. The friction between the particles and the friction of the particles with the stationary wall during flowing has a significant effect on the way the powder flows. These interactions are illustrated in Figure 4-1. The particle flow rate is not uniform because of the friction (internal and wall), which could be referred to fluid flow (maximum shear close to the stationary wall and minimum shear at the centre (Rhodes, 2008)). Thus, the amount of particles coming from different positions are different. More particles pass through the central cross-section part due to higher flow rate at the central part in comparison to the sides where wall friction is at its maximum.

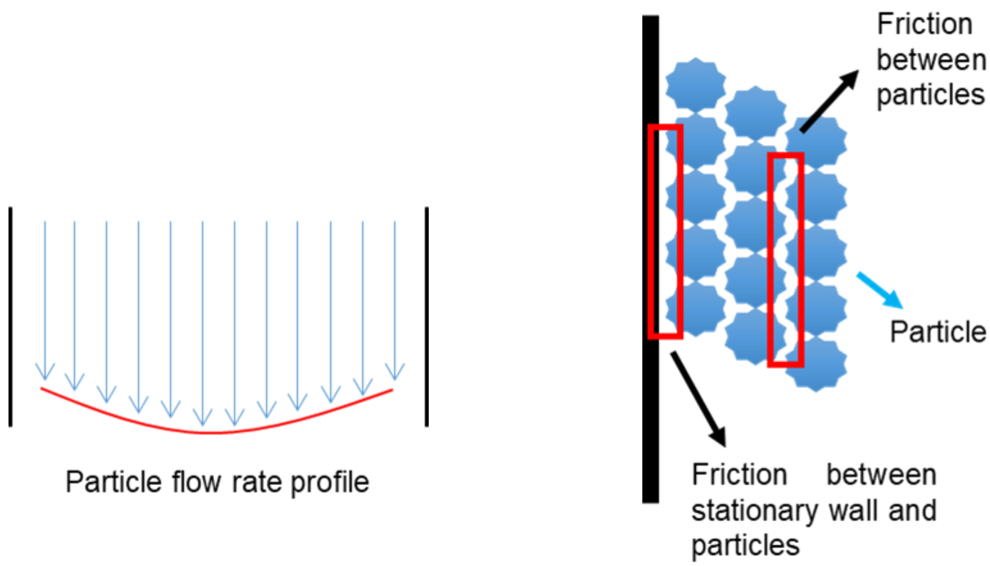

Figure 4-1: Particle flow rate profile and friction during flowing.

In order to improve the uniformity of powder distribution at different positions over the cross-section area, a method was purposed to control the amount of powder at different parts across the cross-section. Figure 4-2 shows the new design that is used to control the amount of powder flows at different positions. In order to achieve a uniform powder flow, the design allows more powder to flow at the side part and less powder at the centre of the design. 40 g of powder was used in the experiments. The diameters of straws increase from 2, 3 to 4 mm from the centre to the outside, as shown in Figure 4-2 (a). The setup is shown in Figure 4-2 (b). The experiment involves flowing of powder through the straws from the top to the bottom container. The height of powder in the bottom container was measured with a fixed scale across the container diameter to investigate the performance of the new design.

(a) (b)

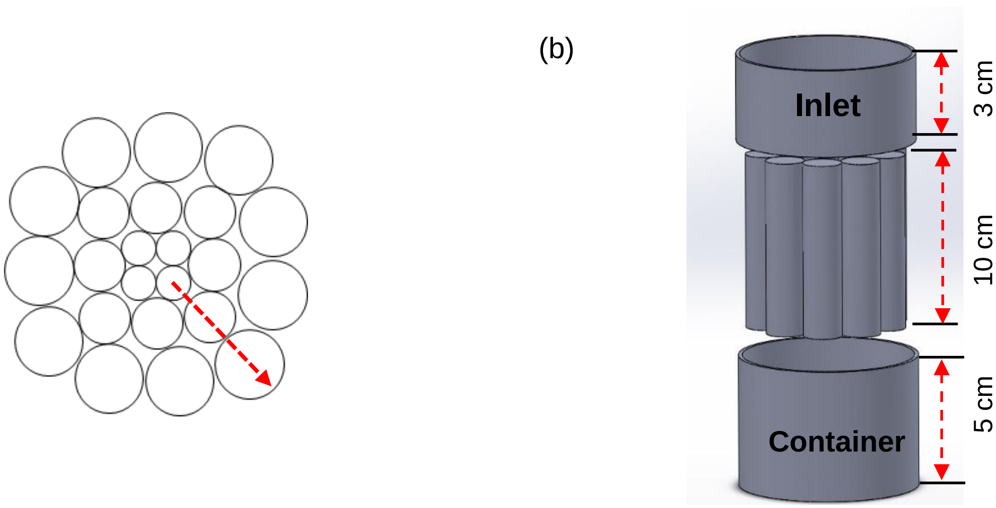

Array design of straws Setup sketch of straws

Figure 4-2: Array design of straws for controlling the particle flow.

As the diameter of some straws in this design is relatively small, there is a potential of blockage, especially with a cohesive powder such as calcium carbonate. Therefore, another guiding setup was designed to improve the powder flow, as shown in Figure 4-3 (a), which is capable to examine powder with different flowability by changing the angle of guiding flights. The height of the guiding setup is 10 cm, and the cross-section area is 4 x 4 cm^{2,} as shown in Figure 4-3 (b).

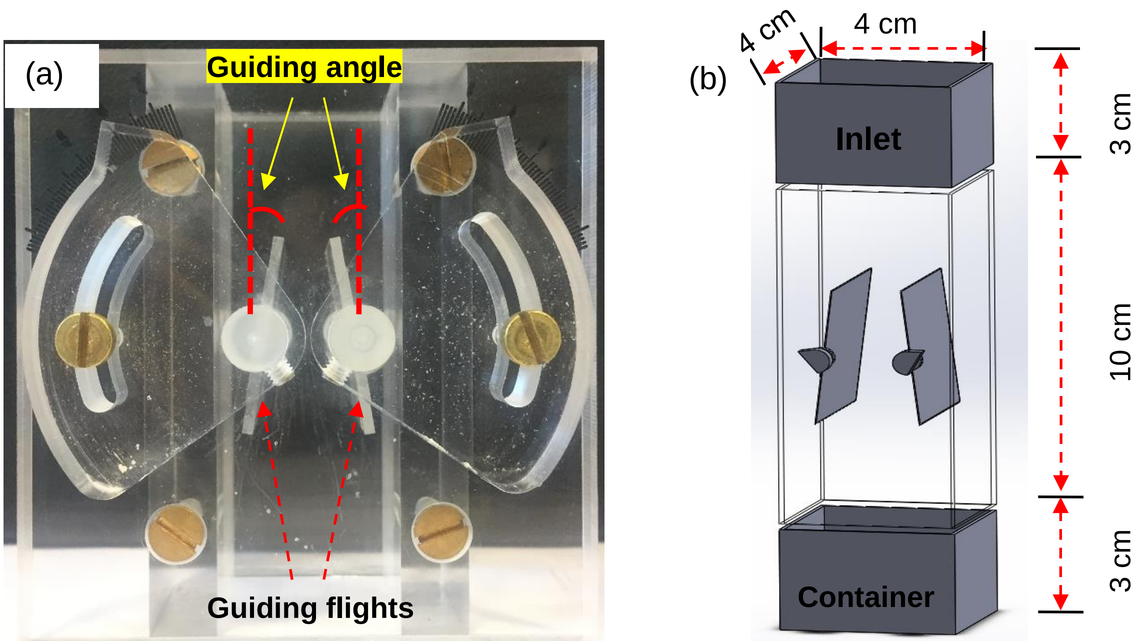

Figure 4-3: Guiding setup with two symmetrical flights and setup sketch.

Similar to the principles of the array design, this design also allows more powder through the sides and less at the centre. In the guiding setup, there are two symmetrical rotating guiding flights (4 cm height) which could rotate to control the amount of powder. When the guiding flights rotate towards the centre, this means less powder passing between the guiding flights and more powder could pass through the sides. Thus, the amount of powder could be guided to be the same at different cross-sectional positions. The powder is falling to the container, and the distribution of powder could be monitored at different positions in the container.

Based on this method which controls the amount of powder during discharge, the hypothesis is to apply this method in the roller compaction to improve the powder flow to the compaction stage.

4.3 Results

4.3.1 Flow properties of powder

4.3.1.1 Angle of repose

The angle of repose is one way of representing the powder flowability. The higher the angle, the poorer the flowability of the powder. The angle of repose varies when the relative humidity changes, as shown in Table 4-1. Overall, the increase of relative humidity results in the increase of repose angle. For example, Maltodextrin powders are sensitive to moisture, which causes the particles to clump together and form liquid bridges. The repose angle of light sodium carbonate did not change significantly with varying relative humidity.

Table 4-1: Angle of repose of powder at the relative humidity of 40 % and 60 %.

Materials	Angle of repose (40%)	Angle of repose (60%)
Starch 1500	31.3 ± 0.3	35.8 ± 0.4
GLUCIDEX ® Maltodextrin DE6	35.8 ± 1.2	39.8 ± 1.1
Avicel ® PH101 MCC	38.4 ± 1.2	48.4 ± 0.4
Tylopur ® 603 HPMC	43.3 ± 0.3	47.3 ± 0.3
Pharmatose ® 200 M	44.5 ± 0.5	48.6 ± 1.2
Light Sodium Carbonate	44.8 ± 1.4	43.6 ± 1.1

4.3.1.2 Flow function coefficient (ffc) measurement by shear cell

The shear cell is another way to examine the powder flowability. The flow function coefficient (ffc) is introduced as the powder flowability as using the shear cell. When the value of ffc is between 2 and 4, powders are considered to be cohesive, such as Pharmatose 200 M. If the ffc is between 4 and 10, the powder is easy flowing (Fitzpatrick et al., 2004). This is the case for Avicel ® PH101 MCC, Tylopur ® 603 HPMC, Light Sodium Carbonate, GLUCIDEX ® Maltodextrin DE6 and Starch 1500. Starch 1500 particles are the most flowable powder compared to others.

Based on the SEM image in Figure 3-1, starch particles are spherical compared to the particles of other materials, which contributed to better flowability.

The flow function coefficient (ffc) of materials are also influenced by relative humidity as shown in Table 4-2. The increase of relative humidity results in the decrease of flow function coefficient of most types of powder.

Table 4-2: Flow function coefficient (ffc) of powder at relative humidity (RH) of 40 % and 60 %.

Materials	ffc - 40 % (RH)	ffc - 60 % (RH)
Pharmatose ® 200 M	3.23 ± 0.13	3.04 ± 0.02
Avicel ® PH 101 MCC	3.70 ± 0.20	2.68 ± 0.12
Tylopur ® 603 HPMC	4.33 ± 0.13	3.55 ± 0.11
Light Sodium Carbonate	5.09 ± 0.43	4.39 ± 0.23
GLUCIDEX ® Maltodextrin DE6	6.50 ± 0.25	3.43 ± 0.23
Starch 1500	8.05 ± 0.25	3.66 ± 0.33

4.3.2 Controlling powder flow by an array design of straws

As the powder flowability has been investigated, the idea is proposed to control the powder flow by designing the guiding setups. The array design of straws with varying diameters is designed to improve the powder flow as shown in Figure 4-2. The purpose is allowing less amount of powder pass through the centre and more amount of powder pass through the side of the setup.

Figure 4-4 shows the powder distribution with and without the design of straws. As shown in Figure 4-4 (a), powders flowed to the container without the array design of straws that results in the cone shape of the powder bed. This illustrates that the amount of powder is not uniform at different positions of the cross-sectional area. Figure 4-4 (b) displays the powder distribution via an array of straws with increasing diameter from the centre to the side of the array design. Powders are uniformly distributed with similar height at different positions of the powder bed surface. The array of straws can allow less powder to pass through the centre by using the small diameter and more powder at the side by using the large diameter of straws.

Comparing Figure 4-4 (a) and (b), the powder was uniformly distributed by using the array design of straws. Although this works for some powders, but for some cohesive powder with poor flowability, which is not easy to pass through the straws because of friction that causes a blockage. Also, there is still non-uniform powder distribution to some extent after discharge, and small cones of distributed powder happen. Therefore, another setup was introduced with more control options for a range of powder in the following section.

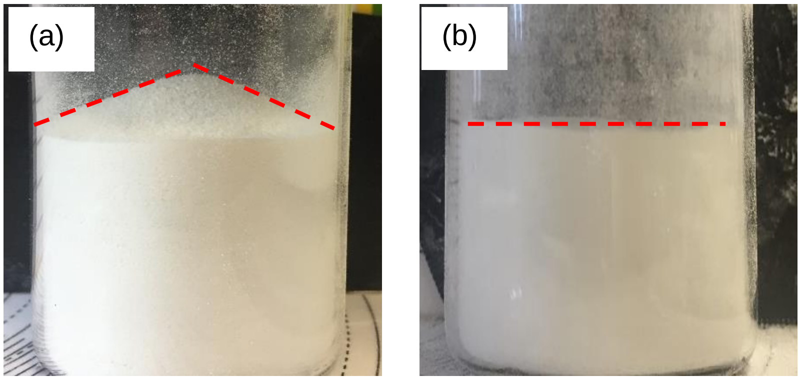

(a) Powder distribution without an array of straws

(b) Powder distribution with an array of straws

Figure 4-4: Powder distribution by flowing to the container (Avicel ® PH101 MCC powder is used in the figure).

4.3.3 Controlling powder flow by a new guiding setup

The powder flow in the new guiding setup can be influenced by powder flowability. Thus, a guiding setup with adjustable flights was designed to investigate the effect of powder flowability on the improvement of powder flow as shown in Figure 4-3. This could overcome the limitation of the design of array straws.

By changing the angle of guiding flights, the amount of powder distributed is found to be improved at different parts of the cross-section area. When the powders are uniformly discharged and distributed in the container by changing the angle of guiding flights, the angle is defined as the optimum guiding angle.

Figure 4-5 shows that the improvement in the flow for Avicel ® PH101 MCC powder; the height of the powder bed surface was measured by the scales on the inner wall of the container. Figure 4-5 (a) shows the powder flow into the container without adjusting the guiding angle in the setup, the height of powder bed at the centre and sides is not the same. Figure 4-5 (b) shows the powder flow into the container with an adjusted optimum guiding angle in the setup, the height of powder bed at the centre and sides are in the similar distribution level.

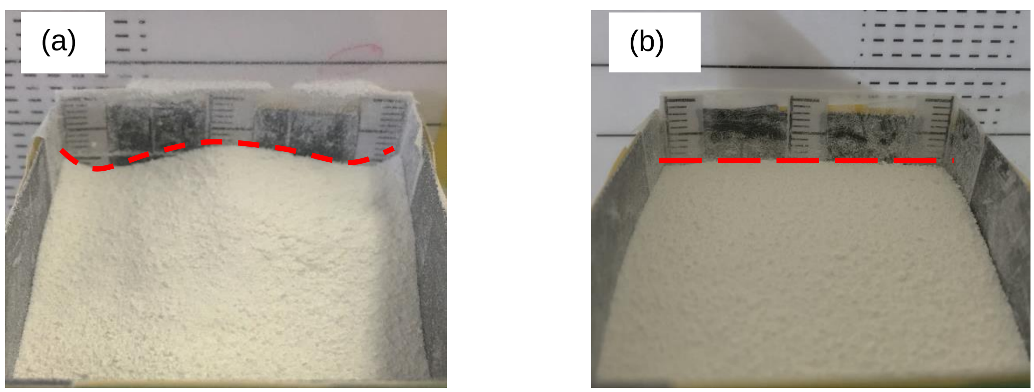

(a) Powder distribution without adjusting the guiding angle

(b) Powder distribution with an adjusted optimum guiding angle

Figure 4-5: Powder distribution of Avicel ® PH101 MCC.

The other materials are also examined using different guiding angles as the powder is conditioned at the two relative humidity conditions (40% and 60%), as shown in Figure 4-6. As the angle of repose increase, the optimum guiding angle decreased.

The reason is that the more flowable the powder, the larger guiding angle needed to adjust in order to allow less powder to pass through the centre and guide more powder to the sides of the setup. The increase of relative humidity results in the increase of the angle of repose. At two conditions of relative humidity, as the angle of repose increases, the optimum guiding angle decreases, as shown in Figure 4-6. When the powder is more flowable, a high value of guiding angle is needed and vice versa. In addition, other examined materials are also plotted in the graph shown in Appendix 7.

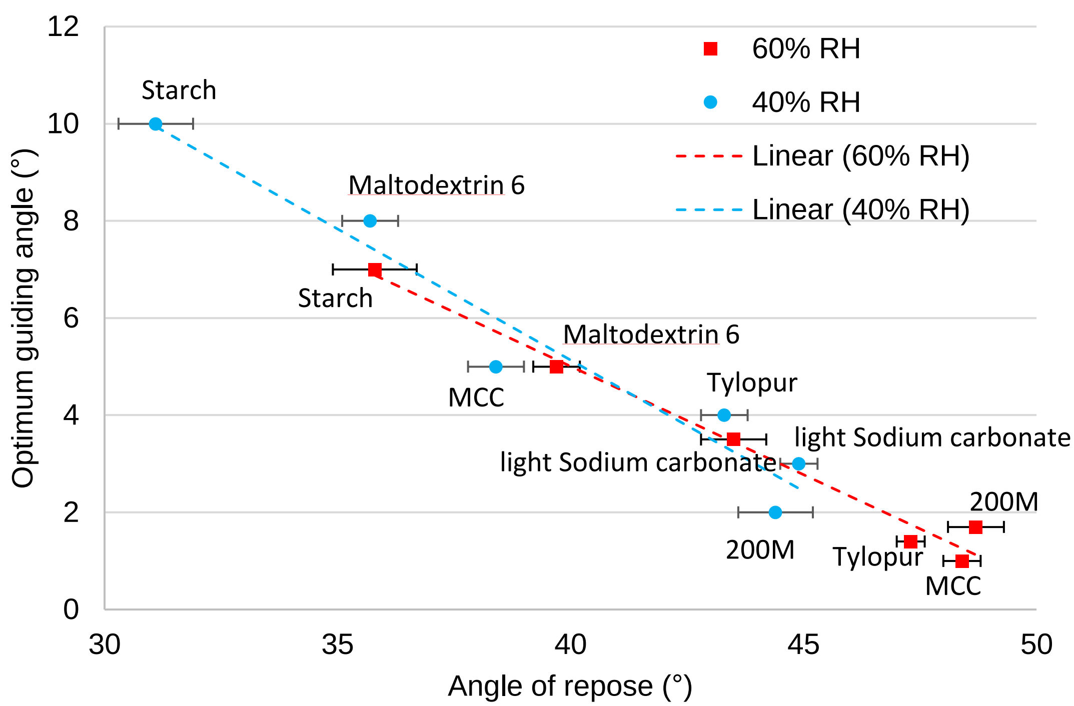

Figure 4-6: Optimum guiding angle as a function of repose angle (from powder flowability measurement) at 20°C and the relative humidity of 40% and 60%.

4.4 Conclusions

In this study, the powder flow performance has been assessed by examining the powder distribution after the discharge. An array design of straws and guiding setup were developed and found to be useful to improve the uniformity of the powder distribution after flowing across the whole cross-sectional area at a different relative humidity (40% and 60%).

In the array design of straws, the amount of powder discharged is controlled by the diameter of straws. The larger diameter of straws contributes to more amount of powder pass through. Overall, the powder distribution after the array design of straws became better than the single pipe or free discharge.

In the design of the guiding setup, the amount of the powder to the centre and the side is guided to be uniform by adjusting the guiding flights with varying angles. Also, the utilisation of guiding setup with flights shows that general decrease trend of optimum guiding angle with the increase of repose angle. That means powder with good flowability needs a higher guiding angle to achieve the uniform powder distribution during the discharge.

Chapter 5 Implement of novel feeding guiders in lab and pilot plant scale of roller compactors

5.1 Introduction

This chapter investigates the effectiveness of novel feeding guiders in adjusting the powder flow and improving the uniformity of product quality (ribbon), and the way can be applied in WP120 Pharma (lab scale) and WP200 Pharma (pilot plant scale) roller compactors. The feeding guiders are located in the feeding zone before the rollers. The ribbon will be produced by using different primary powders. The temperature and porosity temperature distribution across the ribbon width will be used to evaluate the contribution of the feeding guiders in improving the powder feeding uniformity across the roller width.

5.2 Methodology

5.2.1 Design of novel feeding guiders in two scales of roller compactors

The WP120 Pharma guiders are made of PLA (polylactic acid) materials; however, WP200 Pharma guiders are made of ABS (acrylonitrile butadiene styrene) materials which consider the industrial-scale use. There are two types of guider used in the section of the study: one type of guiders (Guider A) is with the convex contact across the central width (half-length of roller width); the other one (Guider B) is with the convex contact across the full width (full-length of roller width) as shown in Figure

5-1. The dimension of feeding guiders used in WP200 Pharma, is equal to multiply the dimension of feeding guiders used in WP120 Pharma with a ratio of WP200 Pharma roller diameter to WP120 Pharma roller diameter, which is 1.66.

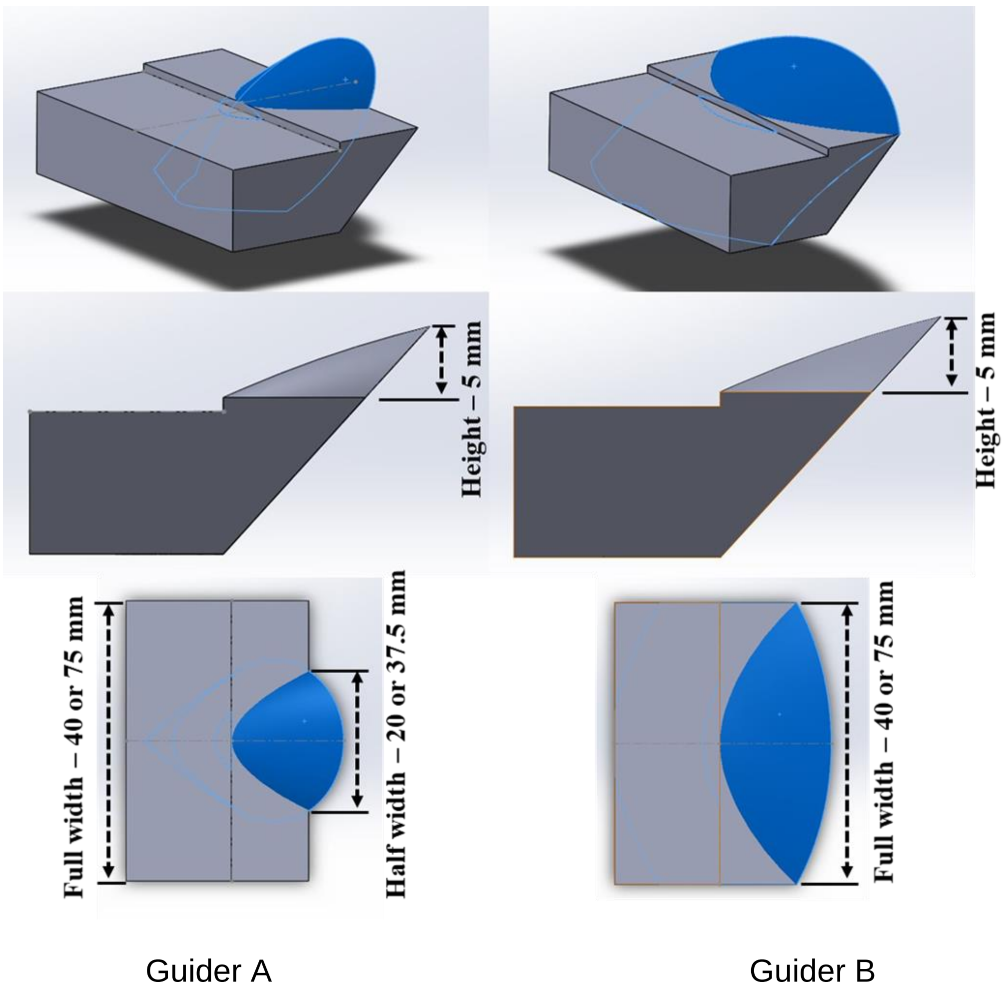

Figure 5-1. Designs of novel feeding guiders in lab scale and pilot plant scale of roller compactors.

The feeding guiders are designed to be used in the feeding zone. They are located between the screw feeder and rollers in the roller compactor, as seen in Figure 5-2 (a). The original feeding guider has a flat surface, as shown in Figure 5-2 (b). The feeding guiders with the convex surface, as shown in Figure 5-2 (c) aim to redirect the powder from the centre to the side between the rollers. Powder coming from the screw feeder will pass through the space between the feeding guiders. Therefore, the feeding guiders can push powders from the centre towards the sides between the rollers, which can improve the uniformity of powder distribution, as shown in Figure 5-3.

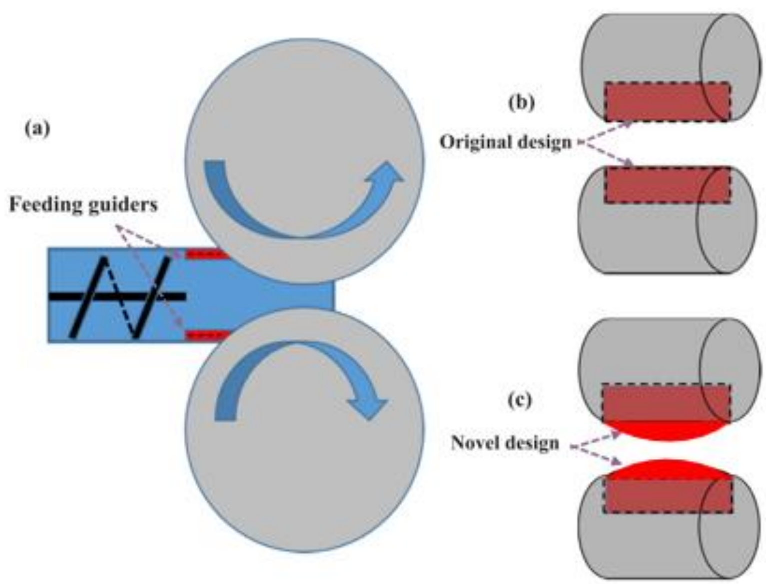

Figure 5-2. Location of the novel feeding guiders in the roller compaction process.

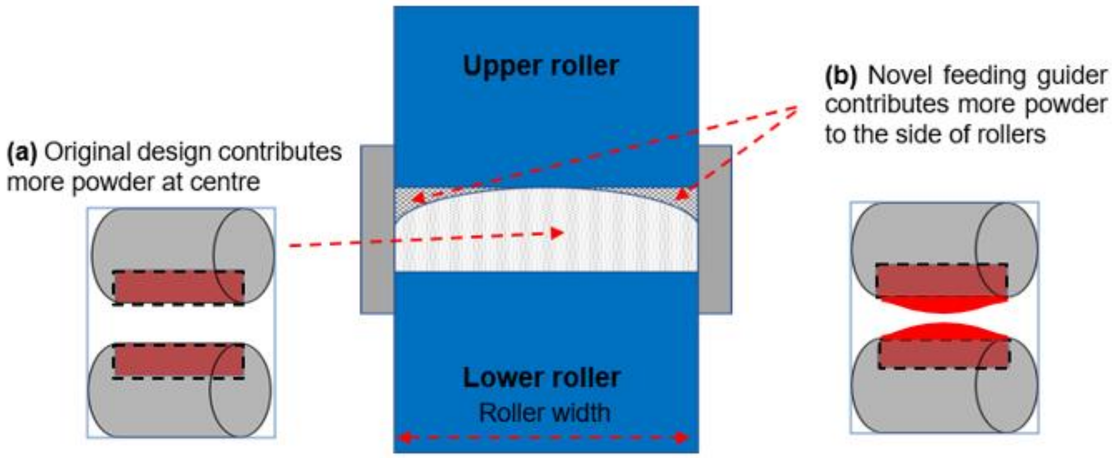

Figure 5-3. Amount of powder fed across the roller width.

5.2.2 Design of roller compaction experiments

In this study, a range of maximum stress applied to the powder is calculated from Johanson theory with process parameters used in lab and pilot plant scale of roller compaction, including roller force, roller diameter and roll gap; and materials' properties, including compressibility factor and material flow properties as shown in Table 5-1.

Table 5-1. Materials' properties used in the Johanson theory.

Materials	Internal friction angle (°)	Angle of wall friction (°)	Compressibility factor
Pharmatose ® 200M	41.2 ± 0.3	33.8 ± 0.2	12.5
Avicel ® PH101 MCC	40.6 ± 0.2	31.6 ± 0.2	4.1
GLUCIDEX ® Maltodextrin DE 6	38.0 ± 0.2	29.2 ± 0.3	5.0

The maximum stresses are used to compare the effects on the product properties in WP120 Pharma and WP200 Pharma, as shown in Figure 5-4 and Table 5-2. As shown in Table 5-2, the nip angle calculated from the Johanon theory is not changing regarding the different roller forces.

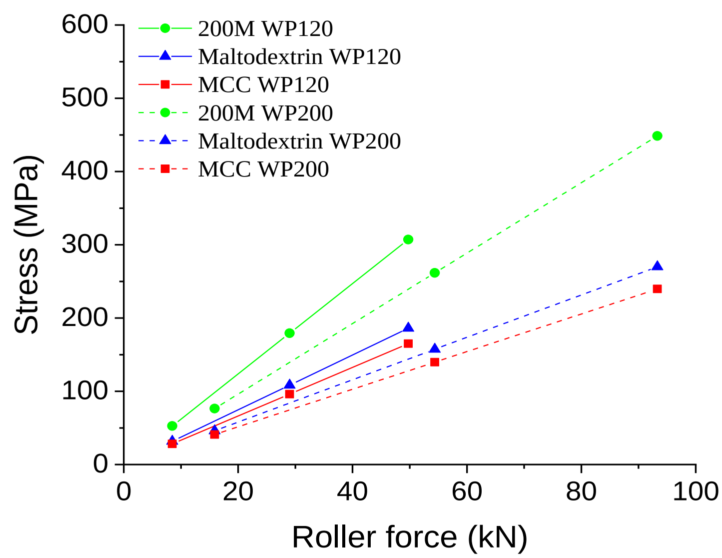

Figure 5-4. Maximum stress applied to the powder.

Table 5-2. Roller maximum stress and nip angle of three materials calculated from Johanson theory.

Roller force (kN)	WP 120 Pharma						WP 200 Pharma					
	200 M		MCC		Maltodextrin		200 M		MCC		Maltodextrin	
	Maximum roller stress (MPa)	Nip angle (°)	Maximum roller stress (MPa)	Nip angle (°)	Maximum roller stress (MPa)	Nip angle (°)	Maximum roller stress (MPa)	Nip angle (°)	Maximum roller stress (MPa)	Nip angle (°)	Maximum roller stress (MPa)	Nip angle (°)
8.5	52.6	13.1	28.2	22.8	31.8	18.2	N/A					
15.9	N/A						76.5	12.4	40.9	22.1	46.1	17.4
29	179.4	13.1	96.1	22.8	108.3	18.2	N/A					
49.8	307.9	13.1	165.0	22.8	186.1	18.2	N/A					
54.4	N/A						261.6	12.4	139.8	22.1	157.5	17.4
93.3	N/A						448.6	12.4	239.7	22.1	270.1	17.4

5.3 Results

In this study, experiments are carried out by investigating powder with different flowability. Thus, feeding guiders (Guider A and Guider B) are used in order to achieve the powder more uniformly fed to the compaction zone. The result section starts with the poor flowability powder Pharmatose 200M, followed by the medium flowability powder MCC and finally the good flowability powder Maltodextrin DE6. For the poor flowability powder Pharmatose 200M, experiments mainly use the guiders with central convex (Guider A), which contributes to more powder guided to the sides between the rollers comparing to the guiders with the full-width convex (Guider B) used for MCC and Maltodextrin DE6.

5.3.1 Pharmatose 200M

5.3.1.1 Temperature distribution profiles across the ribbon width

The temperature of the ribbon during production is recorded by the thermal camera. The thermal images are analysed to determine the temperature distribution across the width of the ribbon produced at different roller stresses using the original design and the feeding guiders. The temperature distribution profiles of the ribbon produced in WP120 Pharma and WP200 Pharma roller compactors are shown in Figure 5-5 (a) and (b) by using the original guiders, and Figure 5-5 (c) and (d) by implementing feeding guiders (Guider A).

Comparing Figure 5-5 (a) and (c) for the WP120 Pharma, it shows that the feeding guiders contribute to more uniform temperature distribution across the ribbon central width (showing as the flatter part of the profile in Figure 5-5 (c) compared to the original design as shown in Figure 5-5 (a). Also, Figure 5-5 (c) shows that the flattest part of temperature profiles is corresponding with the lowest roller stress (52.6 MPa);

less flat parts of temperature profiles are obtained when higher roller stresses are applied (179.4 MPa and 307.9 MPa).

Additionally, Figure 5-5 (b) shows in the WP 200 Pharma, higher ribbon temperature occurs at the side of minus axis because of the rotating feeding screw, which is pushing relatively more powder to the side of the minus axis in comparison to the other regions (positive axis). As the Pharmatose 200M powder has poor flowability properties, there will be a higher discrepancy in the amount of powder across the roller width during the feeding process. Consequently, the higher amount of powder results in a higher temperature of ribbons at the side of the minus axis.

While in Figure 5-5 (d), it is almost a flat temperature profile across the width under the 76.5 MPa of roller stress with Guider A. When the roller stress increases, the flat part of temperature profiles is still over half the ribbon width for the WP 200 Pharma, which showed more improvement than the results for the WP120 Pharma when Guider A is implemented.

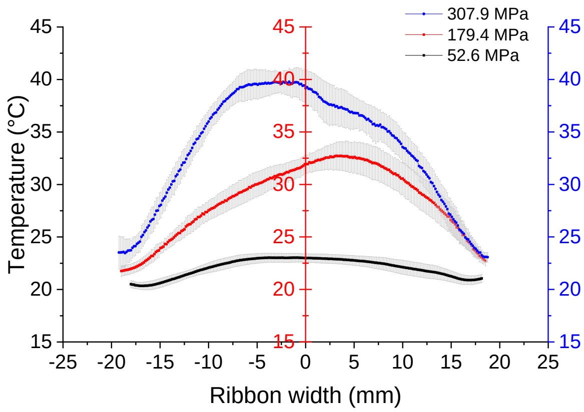

(a) WP120 Pharma Original design guider

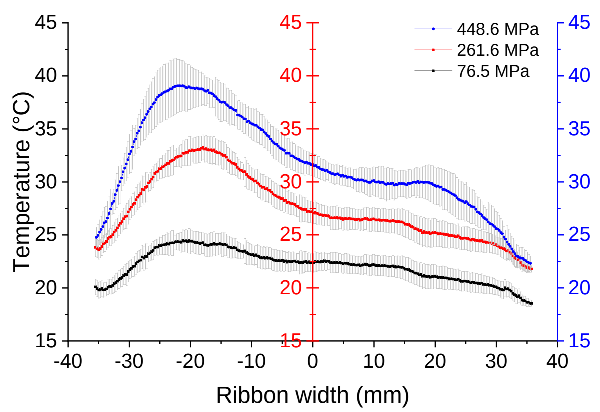

(b) WP200 Pharma Original design guider

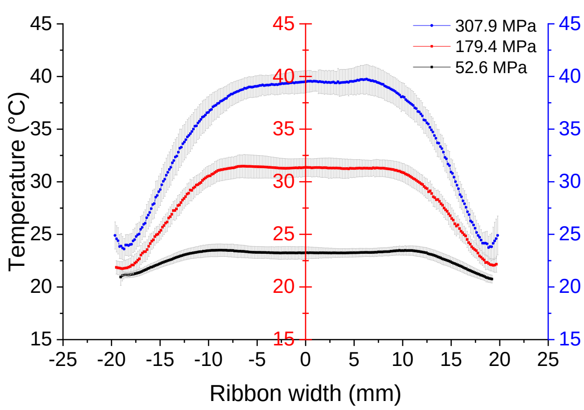

(c) WP120 Pharma - Guider A

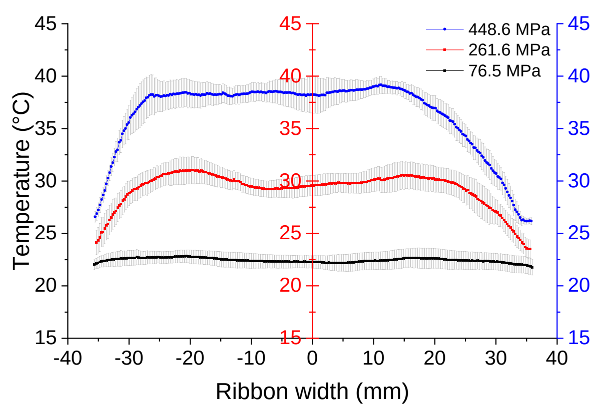

(d) WP200 Pharma - Guider A

Figure 5-5. Temperature distribution across the ribbon width in WP120 Pharma and WP200 Pharma with Pharmatose ® 200 M.

To quantify the uniformity of temperature distribution (the flat part of temperature profiles) across the ribbon width and to make a comparison between the original and feeding guiders, a term – relative temperature uniformity is proposed in Section 3.2.2.1.

Figure 5-6 (a) shows that the feeding guiders (Guider A) in WP120 Pharma improved the relative temperature uniformity of the ribbon to 67.0%, 52.0% and 41.0% as the roller stress increases when compared with the original guiders. Also, Figure 5-6 (b) displays that in the WP200 pharma, the feeding guiders contribute to the increase of the relative temperature uniformity of the ribbon to 92.0%, 68.0% and 61.0% respectively with the increase of roller stress comparing with original guiders. Therefore, the feeding guiders significantly improve (2-3 times) the uniformity of ribbon property across the width when compared to the original design.

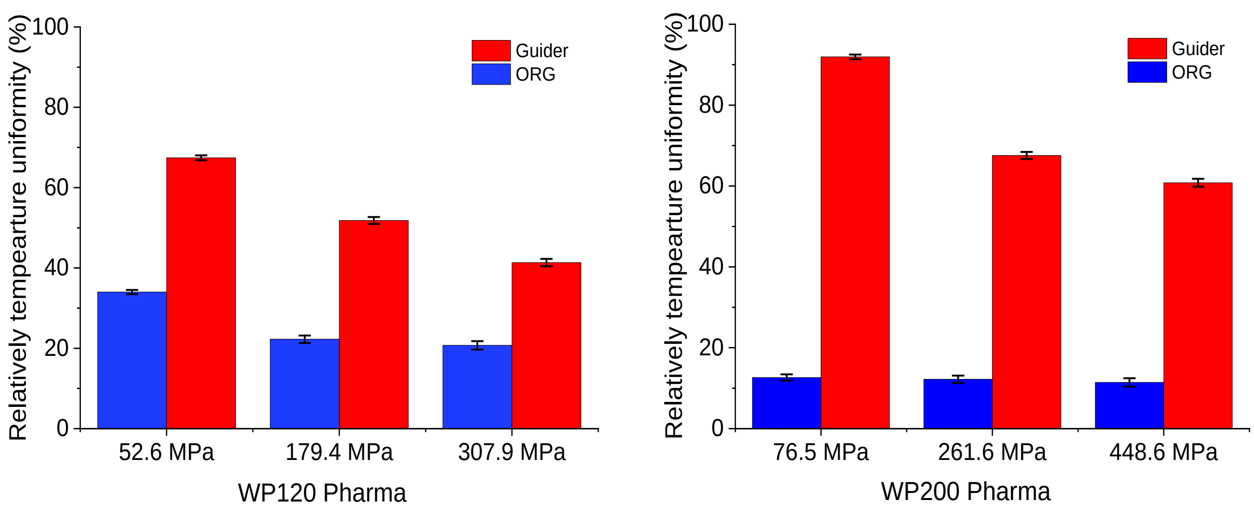

(a) (b)

Figure 5-6. Relatively uniformity of temperature across the ribbon width in WP120 Pharma and WP200 Pharma – Pharmatose 200M.

5.3.1.2 Porosity distribution profiles across the ribbon width

In addition to the temperature profile, the ribbon porosity distribution is another way to present the uniformity of property across the ribbon width. Ribbons for Pharmatose 200M are not produced with a consistent width, and the width of the ribbons was less than the roller width. The sections of ribbons are based on the equal distance around 9.5 mm width per section for WP120 Pharma and WP200 Pharma.

Figure 5-7 shows the porosity distribution across the ribbon width in WP120 Pharma and WP200 Pharma. As for WP120 Pharma, Figure 5-7 (a) and (c) shows the difference of porosity between the ribbon centre and side have been reduced from approximately 17% to 10% using feeding guiders.

While Figure 5-7 (b) and (d) illustrate that in WP200 Pharma, the feeding guiders have contributed to a decreasing difference of porosity across the ribbon width, which is from 12% to 5% under the roller stress of 261.6 MPa and from 16% to 10% under the roller stress of 448.6 MPa.

Comparing to the original design of guiders, the feeding guiders result in a decrease of porosity between the ribbon centre and side and more uniform porosity distribution across the ribbon width.

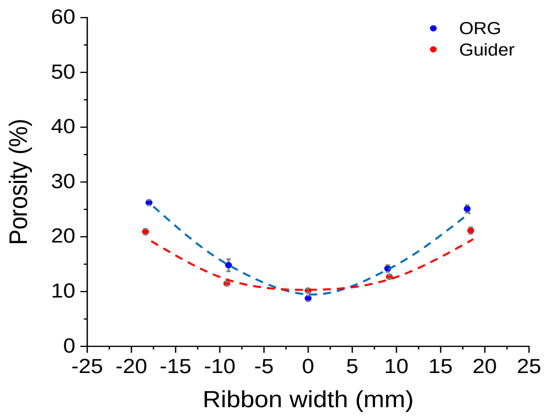

(a) WP120 Pharma – 179.4 MPa

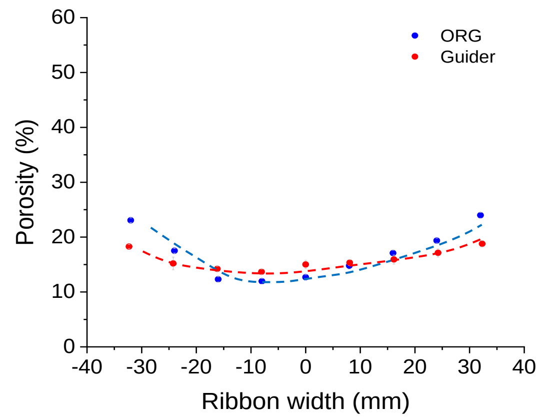

(b) WP200 Pharma – 261.6 MPa

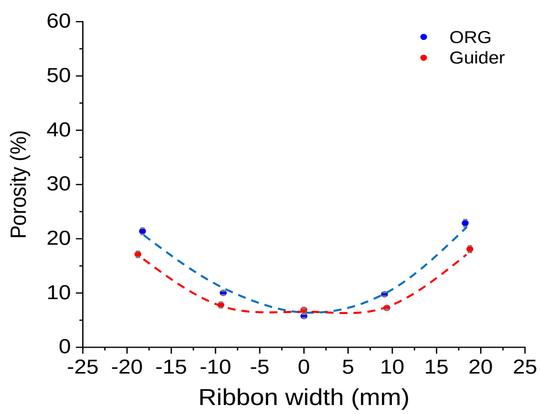

(c) WP120 Pharma – 307.9 MPa

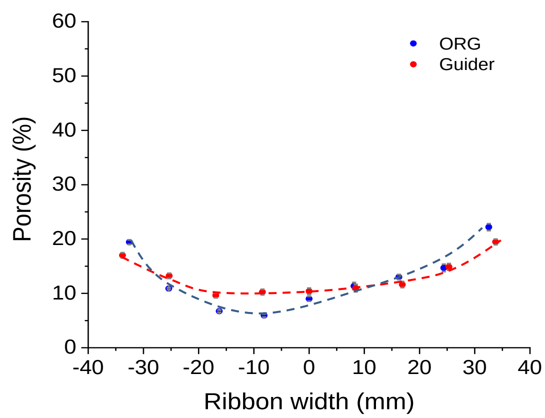

(d) WP200Pharma – 448.6 MPa

Figure 5-7. Porosity distribution across the ribbon width – Pharmatose ® 200M.

5.3.2 Avicel ® PH101 MCC

5.3.2.1 Temperature distribution profiles across the ribbon width

Microcrystalline Cellulose (MCC) is a deformable material (Inghelbrecht and Remon, 1998). This means that at the same stress, it will result in more heat being generated in comparison to a hard material, such as lactose (Pharmatose ® 200M). Figure 5-8 (a) and (b) show temperature profiles from the original design of guiders under different roller stress and Figure 5-8 (c) and (d) show the temperature profiles from the feeding guiders (Guider B) under the different roller stress in WP120 Pharma and WP200 Pharma respectively.

The feeding guiders (Guider B) improved the uniformity of feeding powder fed across the roller width. This resulted in more uniform temperature distribution across the ribbon width, as shown as the flat part of the temperature profiles in Figure 5-8 (c) and (d). Regarding WP120 Pharma, the uniformity of temperature improved to approximately 73.0%, 59.0% and 58.0% under the 28.2 MPa, 96.1 MPa and 165.0 MPa of roller stress, which is higher than the uniformity of temperature from original guider in WP120 Pharma as shown in Figure 5-9 (a). Also, in the WP200 Pharma, the feeding guiders (Guider B) contributed to the relative temperature uniformity of the ribbon reaching around 65.0%, 53.0% and 45.0% as illustrated in Figure 5-9 (b).

Overall, the feeding guiders (Guider B) in WP120 Pharma and WP200 Pharma contribute to a remarkable improvement in the uniformity of ribbon property when compared to the original feeder design.

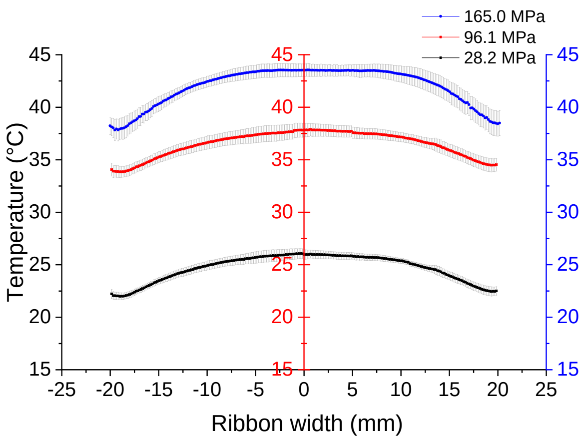

(a) WP120 Pharma Original guider

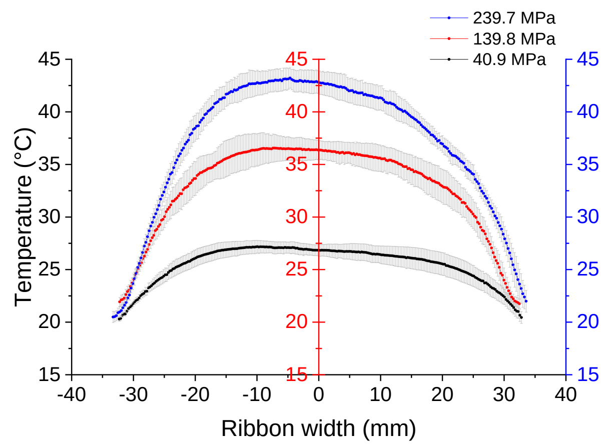

(b) WP200 Pharma Original guider

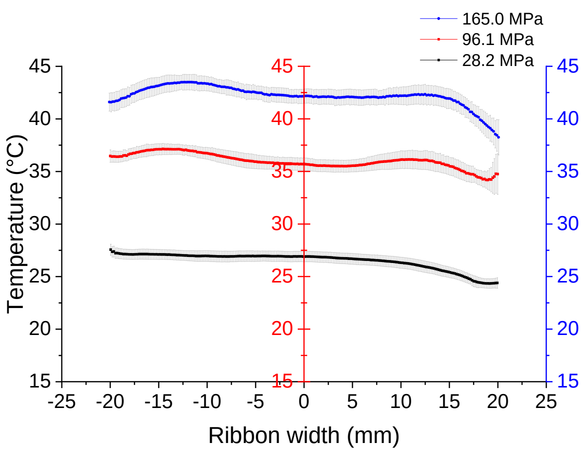

(c) WP120 Pharma - Guider B

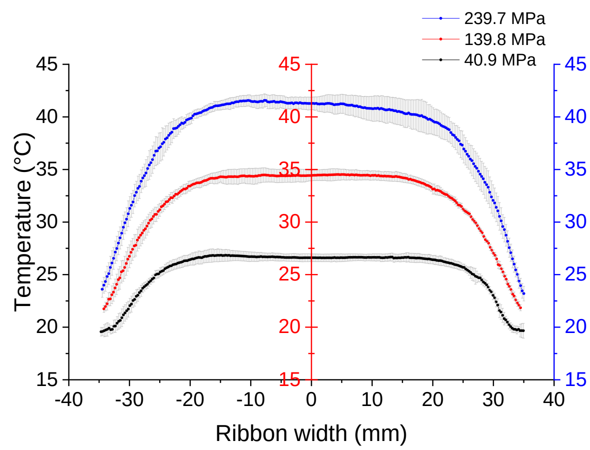

(d) WP200 Pharma - Guider B

Figure 5-8. Temperature distribution across the ribbon width with guider designs in WP120 Pharma and WP200 Pharma with Avicel ® PH101 MCC.

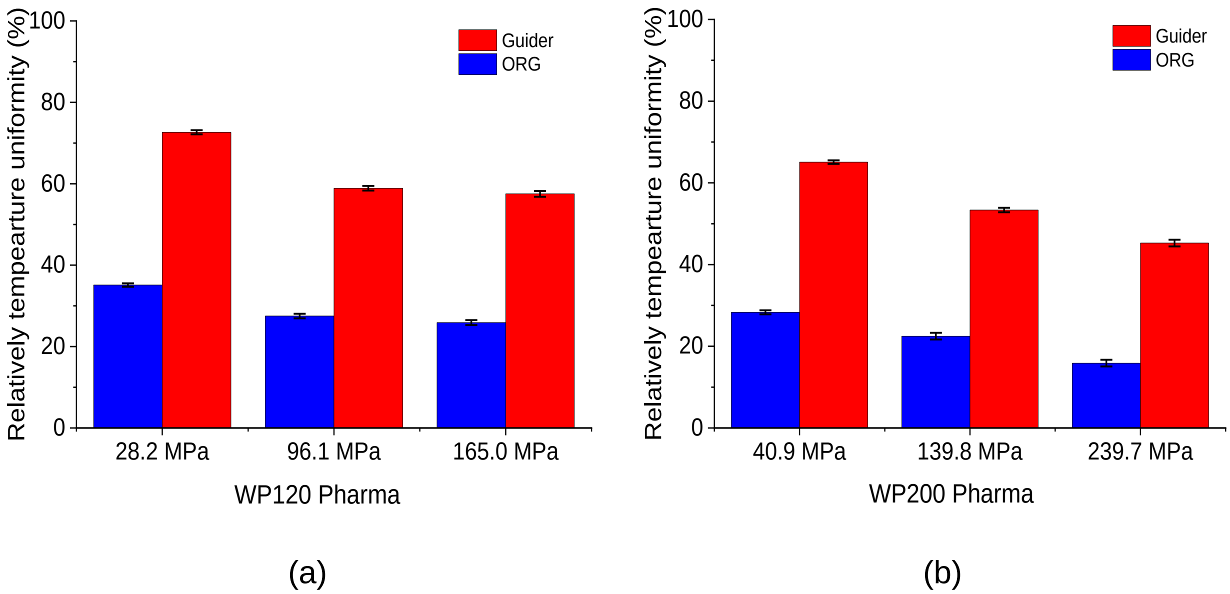

Figure 5-9. Relatively uniformity of temperature across the ribbon width in WP120 Pharma and WP200 Pharma – Avicel ® PH101 MCC.

5.3.2.2 Porosity distribution profiles across the ribbon width

Full-width ribbons are produced for MCC powder, and the ribbons have almost the same width as the roller width. The porosity is measured across the ribbon width. In Figure 5-10, the porosity distribution from the feeding guiders (shown as red scatters) is more uniform than the ones from the original guider (which are shown as blue scatters). Figure 5-10 (a) and (c) shows that feeding guiders lead to more uniform porosity around the ribbon centre comparing to that from the original guiders. The difference of porosity between ribbon centre and side decreases from around 23% to 18% respectively under the roller stress of 96.1 MPa and from 27% to 22% under the roller stress of 165.0 MPa using the feeding guiders in the WP120

Pharma. As for WP200 Pharma, Figure 5-10 (b) and (d) illustrate that feeding guiders contribute to the difference of porosity across the ribbon width reducing from approximately 28% to 15% and from about 36% to 25% respectively under the roller stress of 139.8 MPa and 239.7 MPa.

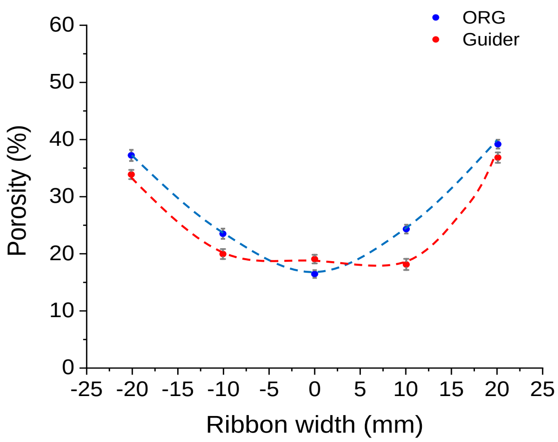

(a) WP120 Pharma – 96.1 MPa

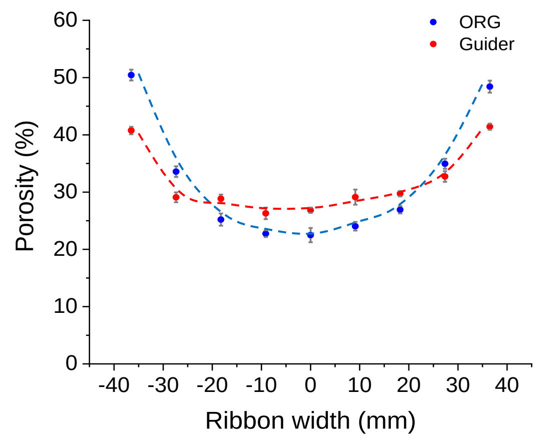

(b) WP200 Pharma – 139.8 MPa

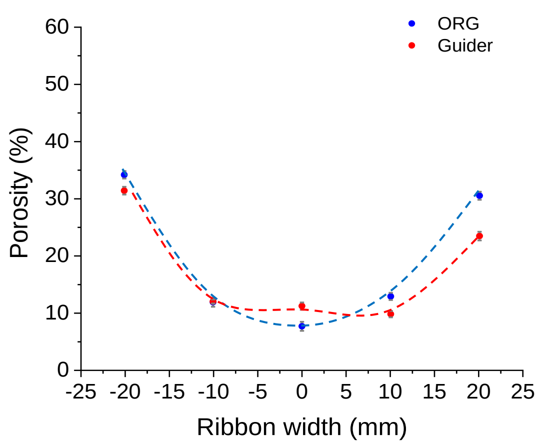

(c) WP120 Pharma – 165.0 MPa

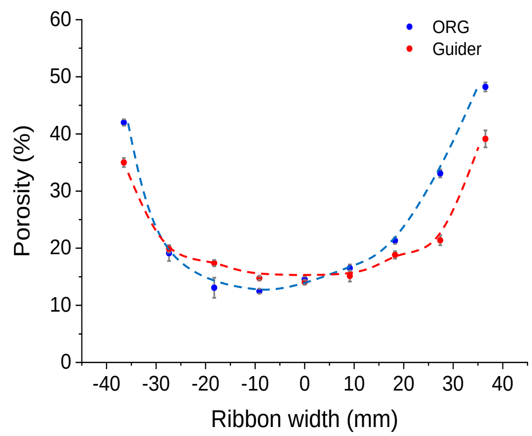

(d) WP200 Pharma – 239.7 MPa

Figure 5-10. Porosity distribution across the ribbon width – Avicel ® PH101 MCC.

5.3.3 GLUCIDEX ® Maltodextrin DE6

5.3.3.1 Temperature distribution profiles across the ribbon width

As Maltodextrin powder has good flowability, the feeding guiders (Guider B) are more helpful to reduce the difference in the amount of powder between the centre and side of rollers comparing to the powder with poorer flowability. Figure 5-11 (a) and (b) show temperature profiles from the original design of guiders. Figure 5-11 (c) and (d) show the temperature profiles from the feeding guiders (Guider B).

Figure 5-11 (a) and (b) show that the temperature distribution is less uniform by applying original guiders than the temperature distribution by using feeding guiders as shown in Figure 5-11 (c) and (d). However, Figure 5-11 (c) shows that feeding guiders (Guider B) contribute to the significant improvement of ribbon temperature distribution under the different roller stresses in WP120 Pharma. The relative temperature uniformity of the ribbon has been improved to 44.5%, 39.5% and 27.5% with the increase of the roller stress, as shown in Figure 5-12 (a). Also, Figure 5-11 (d) illustrates that feeding guiders (Guider B) in WP200 Pharma, result in better distribution of ribbon temperature compared to the original ones as shown in Figure 5-11 (b). The relative temperature uniformity of the ribbon has improved to 76.0%, 55.0% and 53.5% as displayed in Figure 5-12 (b). As a result, feeding guiders improve the relative temperature uniformity across the ribbon width, in comparison to the original feeder design.

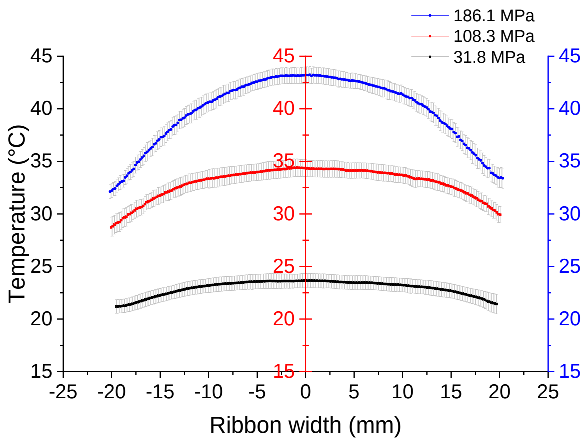

(a) WP120 Pharma Original guider

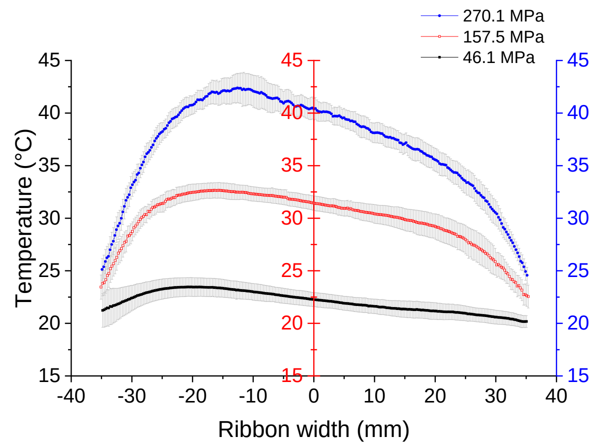

(b) WP200 Pharma Original guider

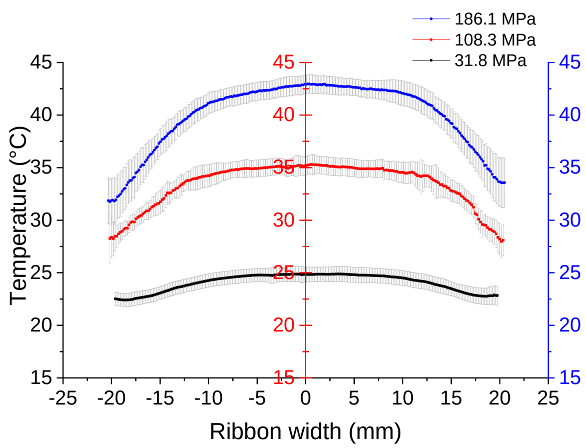

(c) WP120 Pharma - Guider B

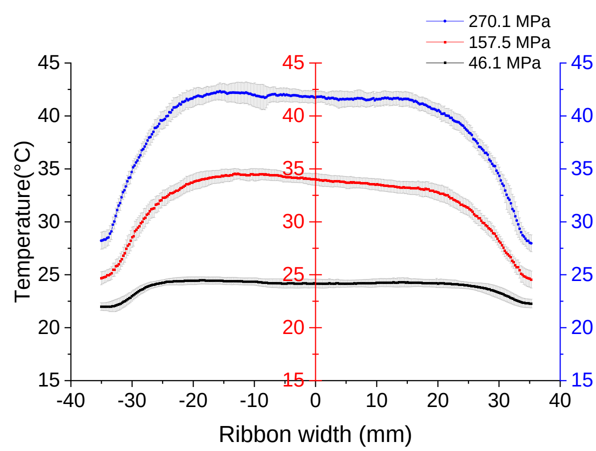

(d) WP200 Pharma - Guider B

Figure 5-11. Temperature distribution across the ribbon width in WP120 Pharma and WP200 Pharma with GLUCIDEX ® Maltodextrin DE6.

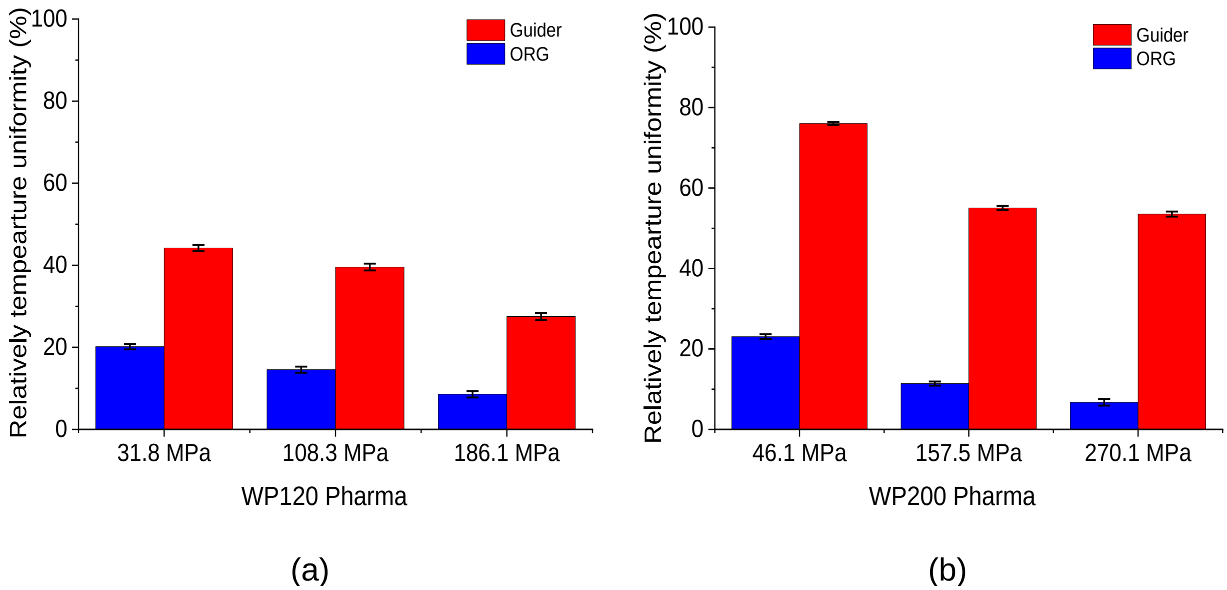

Figure 5-12. Relatively uniformity of temperature across the ribbon width in WP120 Pharma and WP200 Pharma – GLUCIDEX ® Maltodextrin DE6.

5.3.3.2 Porosity distribution profiles across the ribbon width

The porosity distribution across the ribbon width for Maltodextrin powder is shown in Figure 5-13. Comparing the results of feeding guider to original guider as shown in Figure 5-13 (a) and (c), the difference of porosity between the ribbon centre and side decreases from 14% to 11% and from 23% to 12% under the roller stress of 108.3 MPa and 186.1 MPa in WP120 Pharma. As for the results from WP200 Pharma, as shown in Figure 5-13 (b) and (d), the feeding guiders improved the uniformity of porosity distribution across the ribbon width. The difference of porosity between the ribbon centre and side reduces from 16% to 9% and from 19% to 12% respectively under the roller stress of 157.5 MPa and 270.1 MPa.

Overall, Figure 5-13 shows that the feeding guiders contribute to the decrease of porosity at the ribbon sides, which also means more powder compressed at the sides between the rollers.

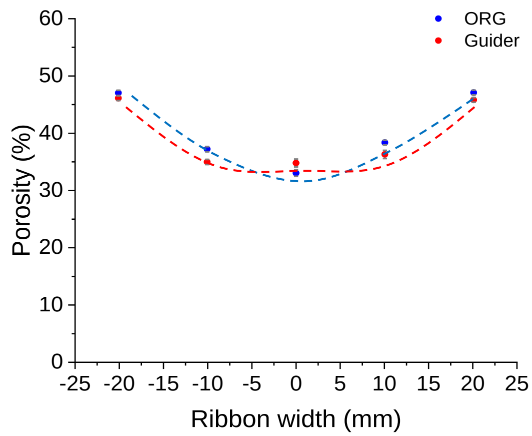

(a) WP120 Pharma – 108.3 MPa

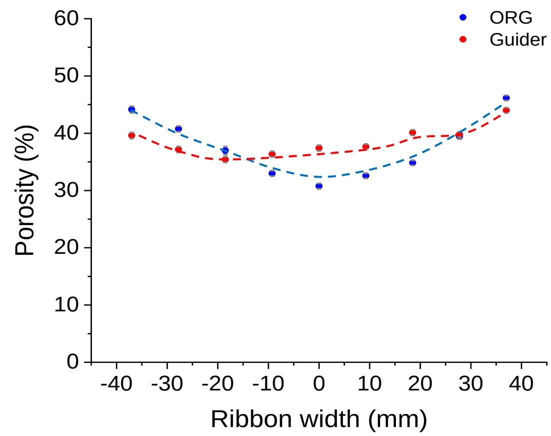

(b) WP200 Pharma – 157.5 MPa

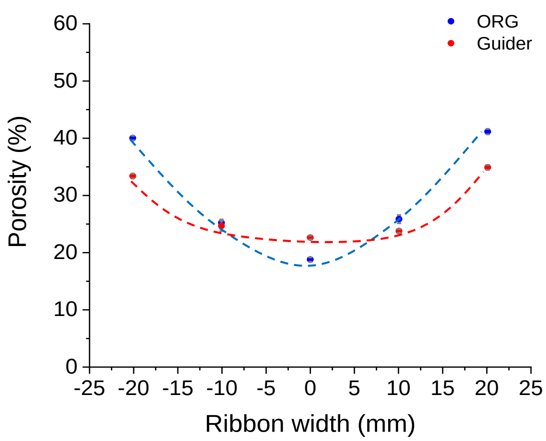

(c) WP120 Pharma – 186.1 MPa

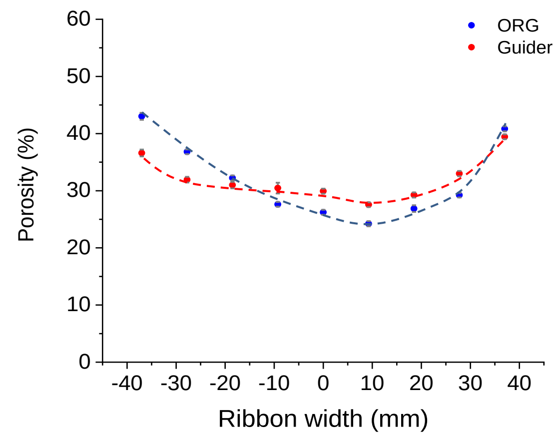

(d) WP200 Pharma – 270.1 MPa

Figure 5-13. Porosity distribution across the ribbon width – GLUCIDEX ® Maltodextrin DE6.

5.4 Conclusions

The feeding guiders are scaled up from WP120 Pharma to WP200 Pharma in order to improve the uniformity of feeding powder to the compaction zone. As the original design of guiders used in WP120 Pharma and WP200 Pharma, the increase of roller stress contributed to the increase of ribbon temperature. The highest temperature is at the ribbon centre and the lowest temperature at the side of the ribbon. This results in a non-uniform temperature distribution (ribbon property) across the ribbon width. However, using the feeding guiders, an improvement has been seen in the uniformity of ribbon temperature across the ribbon width in WP120 Pharma and WP200 Pharma. Consequently, the porosity distribution has also been improved to be more uniform across the ribbon width.

Chapter 6 Improving feeding powder distribution to the compaction zone by novel designed feeding guiders in roller compaction

6.1 Introduction

The powder flow properties make a difference in the product quality in the roller compaction (Yu et al., 2018). In addition, cheek plates (side sealing) have frictional effects on the powder feeding process before the compaction. Thus, the powder is not uniformly fed and distributed in the compaction zone; the different amount of powder is compacted across roller width under different roller forces.

This chapter focus on investigating the uniformity of ribbon temperature with the implementing novel feeding guiders (a series of grades) under different roller forces. The results showed the temperature profiles and relative uniformity with six types of materials.

6.2 Materials preparation

Materials used in the chapter are Pharmatose ® 200M, Avicel ® PH101 MCC, Tylopur ® 603 HPMC, Light Sodium Carbonate, GLUCIDEX ® Maltodextrin DE6, and Starch 1500, which are conditioned in the humidity chamber at 20°C and 40% of relative humidity for 72 hours.

6.3 Methodology

6.3.1 Design of novel feeding guiders in the feeding zone of roller compaction

Powders are not fed uniformly across the width (more at the centre, less at the sides) between rollers. Therefore, the idea is to design feeding guiders with a convex surface to improve the uniformity of feeding powder distribution across the roller width, as shown in Figure 6-1. All feeding guiders are produced by 3D printing technology. A 3D printer - Ultimaker 3 (Ultimaker, Netherlands) is used for printing the guiders with PLA filament (polylactic acid).

The suggested designs of feeding guiders are convex surface designs with varying dimension grades. The convex surfaces can be described as a slope plane with maximum tip height from 1 mm to 15 mm. Figure 6-1 showed the examples of feeding guiders with a maximum tip height of 5 mm (T - 5). Each grade means 1 mm difference for the tip height of feeding guiders.

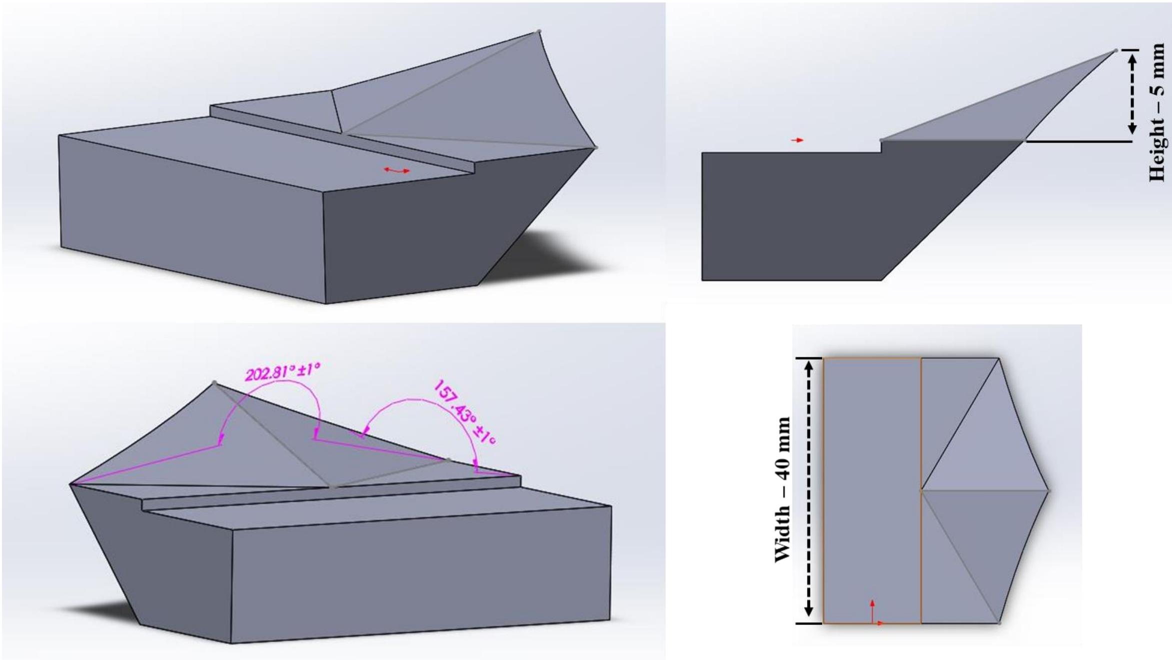

Figure 6-1. Novel feeding guider design example (3D printing).

The feeding guiders are designed to be used in the feeding zone. They are located between the screw feeder and rollers in the roller compactor, as seen in Figure 6-2 (a). The original feeding guider has a flat surface, as shown in Figure 6-2 (b). The feeding guiders with the convex slope surface, as shown in Figure 6-2 (c), aim to redirect the powder from the centre to the side between the rollers. Powder coming from the screw feeder will pass through the space between the feeding guiders. Therefore, the feeding guiders can guide powders from the centre towards the sides between the rollers, which can improve the uniformity of powder distribution, as shown in Figure 6-3.

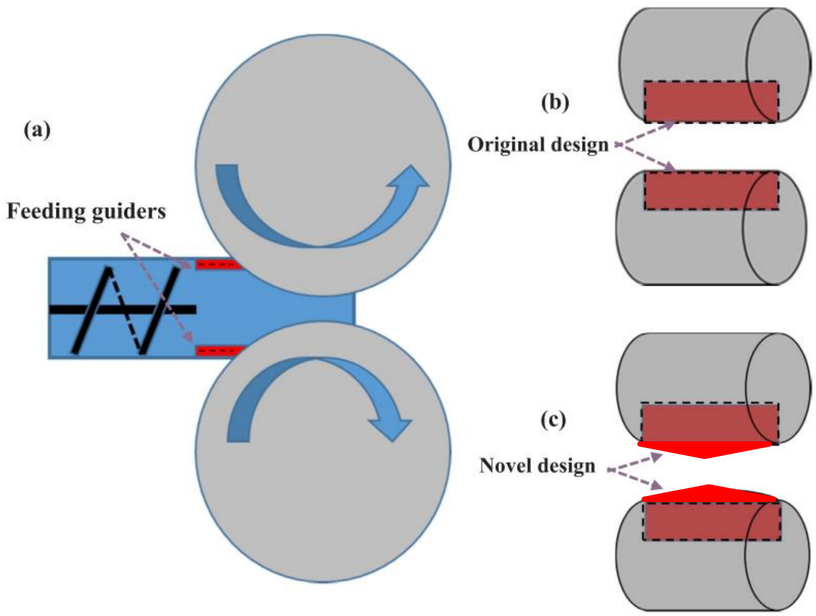

Figure 6-2. Location of the novel feeding guiders in the roller compaction process.

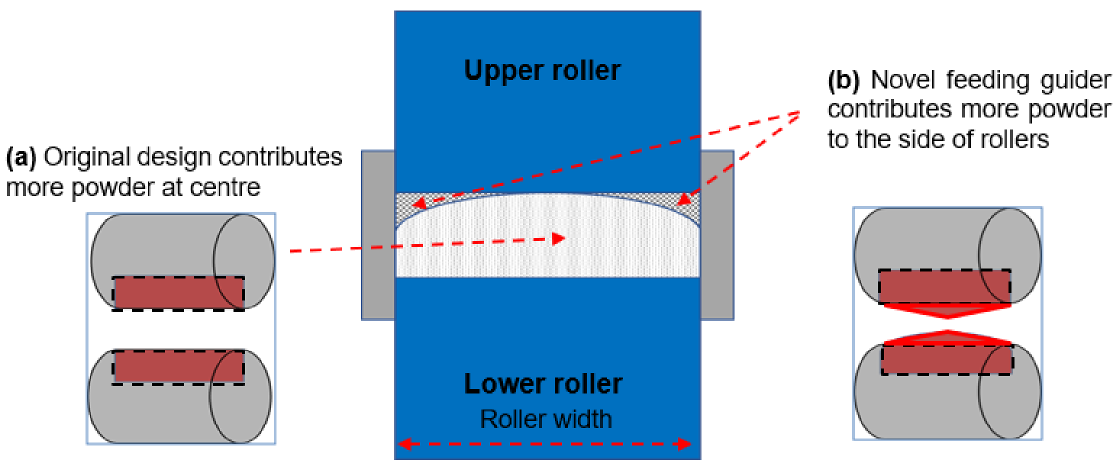

Figure 6-3. Amount of powder fed across the roller width.

6.3.2 Setup of online thermal imaging in roller compaction

Figure 6-4 shows that the thermal camera is set up in the direction where ribbons are produced from the roller gap. The distance between the ribbon and the camera is kept constant at 30 cm (focus distance). During the experiments, as roller force and roller gap achieve a steady state, video of thermal imaging starts to record for 3 minutes. The experiments are repeated five times after the rollers and screw feeder cool down. The measuring methods of emissivity and ribbon temperature have been explained in detail in Section 3.2.2.

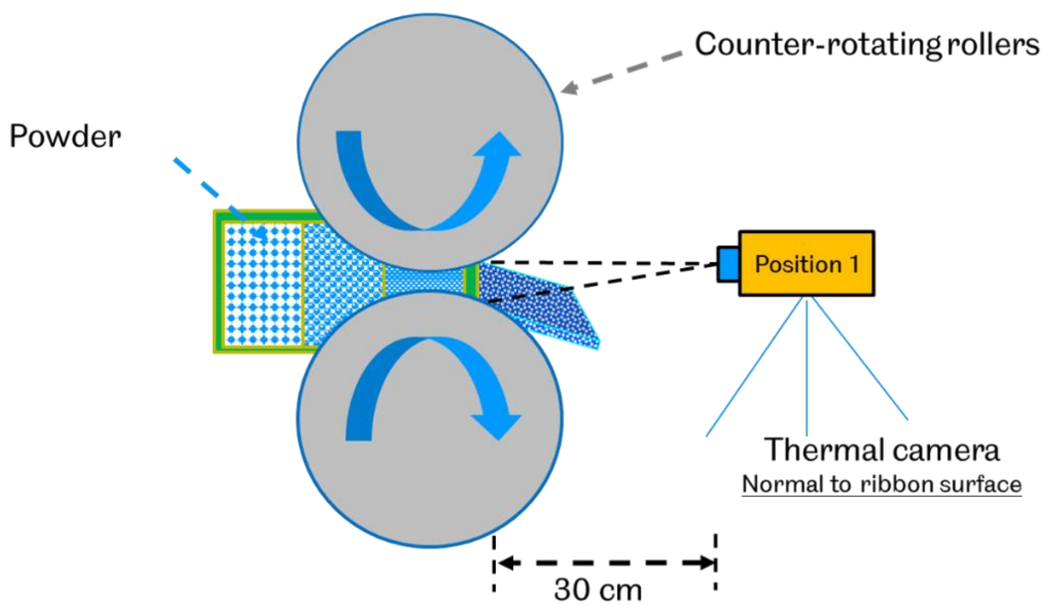

Figure 6-4. Setup of thermal imaging to online monitor the ribbon temperature.

6.3.3 Design of roller compaction experiments

Process parameters in the roller compaction process are 3 rpm of roller speed, 2 mm of roller gap and screw speed which is controlled by the roller gap control mode. The roller forces used are 8.29 kN, 20.72 kN, 29.02 kN and 49.76 kN. The feeding guiders (as shown in Figure 6-1) used in the experiments could be different in height because of various materials' properties and process parameter (roller force).

A range of height grades of guiders has been used for different materials, which is from 1 mm to 14 mm. Optimum design is defined as the guiders contributing to the most uniform temperature distribution across the ribbon width. To figure out the optimum design of the feeding guiders, Table 6-1 shortlists a range of the feeding guiders, which caused the obvious changes of the product properties (temperature distribution across the ribbon width).

In Table 6-1, the grade number ("T – No.") represents the tip height of the feeding guider. For example, "T – 4" grade means 4 mm of tip height for the feeding guider; original guider means 0 mm of tip height. The different colour refers to the different temperature profiles presented in the section of results.

Table 6-1 Grade and dimension of feeding guiders used with process parameters.

Materials	Roller force			
	8.59 kN	20.72 kN	29.02 kN	49.76 kN
Pharmatose ® 200M	Original T – 9 T – 10 T – 11	Original T – 9 T – 10 T – 11	Original T – 9 T – 10 T – 11	Original T – 8 T – 9 T – 10
Avicel ® PH101 MCC	Original T – 10 T – 11 T – 12	Original T – 6 T – 7 T – 8	Original T – 5 T – 6 T – 7	Original T – 3 T – 4 T – 5
Tylopur ® 603 HPMC	Original T – 10 T – 11 T – 12	Original T – 9 T – 10 T – 11	Original T – 8 T – 9 T – 10	Original T – 7 T – 8 T – 9
Light Sodium Carbonate	Original T – 12 T – 13 T – 14	Original T – 9 T – 10 T – 11	Original T – 7 T – 8 T – 9	Original T – 7 T – 8 T – 9
GLUCIDEX ® Maltodextrin DE6	Original T – 9 T – 10 T – 11	Original T – 6 T – 7 T – 8	Original T – 5 T – 6 T – 7	Original T – 4 T – 5 T – 6
Starch 1500	Original T – 12 T – 13 T – 14	Original T – 9 T – 10 T – 11	Original T – 8 T – 9 T – 10	Original T – 7 T – 8 T – 9

6.4 Results

6.4.1 Materials' properties

6.4.1.1 Flow function coefficient (ffc) of powder under different stress

Different powders have different flow properties under different stress, as shown in Figure 6-5. As mentioned in Chapter 3.1.4, the flow function coefficient is one of the parameters representing flowability. Pharmatose ® 200M has the poorest flowability with the lowest value of flow function coefficient under three stress values. On the other hand, Starch 1500 has the highest value of the flow function coefficient. As the normal stress increases, the flowability of powder increased as illustrated, therefore increasing the value of the flow function coefficient. Sun (2016) mentioned that at higher normal stress, it was easier to initiate powder flow than that at lower normal stress.

Figure 6-5 shows that at 2000 Pa of normal stress, Starch has the highest value of flow function coefficient with 6.1, while Pharmatose 200M has the lowest value with 2.3. Flow function coefficient of Maltodextrin with 5.2 is higher than that of Light Sodium Carbonate (LSC) with 4.2 and HPMC with 3.9, followed by MCC with 3.8. The same trend is also showing in normal stress at 5000 Pa and 8000 Pa.

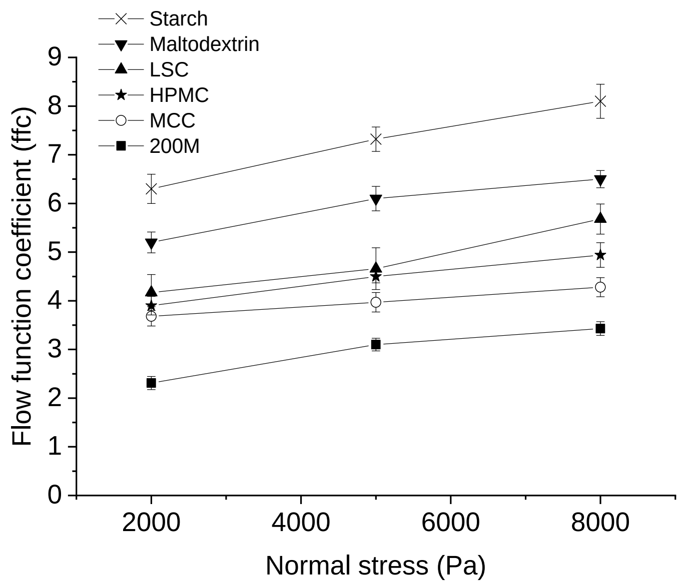

Figure 6-5. Flow function coefficient (ffc) under different normal stress.

6.4.1.2 Angle of wall friction for powder under different stress

The angle of wall friction is measured out by the Ring Shear cell, as mentioned in Chapter 3.1.5. Figure 6-6 shows the angle of wall friction using POM-C wall plates for six materials under different normal stresses.

Figure 6-6 illustrates that at 2000 Pa of normal stress, Pharmatose ® 200M and HPMC have the highest angle of wall friction around 26°; however, Maltodextrin has the lowest value of 12.5°. Light Sodium Carbonate (LSC) has a higher wall friction angle about 23° than MCC with 22° and Starch with 21°. At low values of consolidation stress, powders have not undergone appreciable deformation, and their surface roughness remains relatively intact, resulting in increased friction with the wall material (Jager et al., 2015). As the normal stress increases, the angle of wall friction decreases as shown in Figure 6-6, which is in agreement with results from Sun (2016).

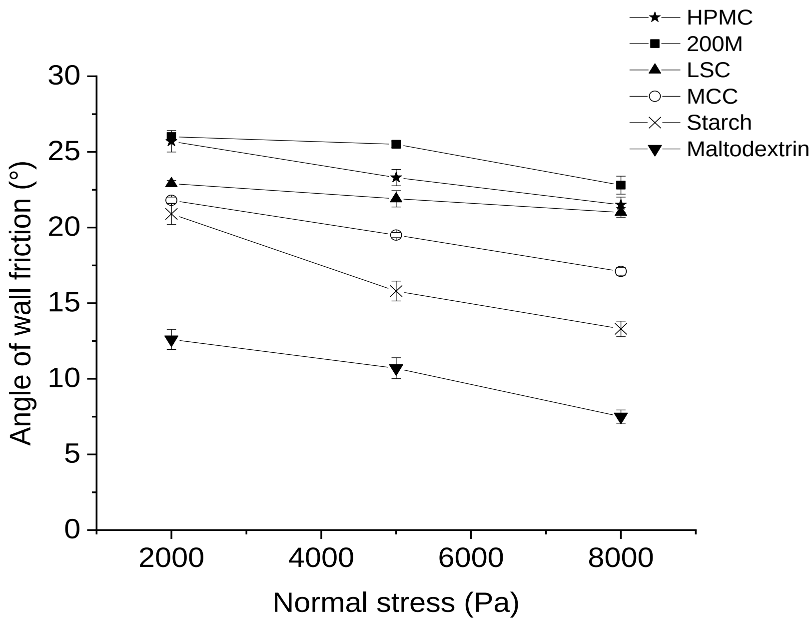

Figure 6-6. Angle of wall friction under different normal stress.

6.4.2 Temperature distribution and relative temperature uniformity across the ribbon width

In this section, it involves the temperature distribution profiles and temperature uniformity for the six materials with original and feeding guiders. The data have been carried out by determining the ribbon temperature captured using the thermal camera. The thermal images of the ribbon temperature surface are shown in the Appendix 8.

6.4.2.1 Pharmatose ® 200M

Temperature distribution profiles across the ribbon width

Pharmatose ® 200M has a poorer flowability than the other materials used in this study, which was used to start the analysis. In Figure 6-7 (a), it is showing the temperature distribution across the ribbon width under the roller force of 8.29 kN. The original guiders result in the ribbon temperature not well uniformly distributed across the ribbon width because of the non-uniform powder distribution in the compaction zone. The more powder compressed by the rollers, the more heat generated (higher temperature) of the ribbon (compacted powder). When the feeding guiders are applied in the feeding zone, they help push more powders to the sides between the rollers, which contributes to more uniform powder distribution during the compaction process. As powders are more uniformly distributed using feeding guiders in the compaction zone, the ribbon temperature from the compaction process becomes more uniform, which is displayed in Figure 6-7 (a). The feeding guiders result in 1 °C decrease in temperature difference between the ribbon centre and side compared to original guiders. In summary, the feeding guiders have improved the powder distribution across the roller width in the compaction zone.

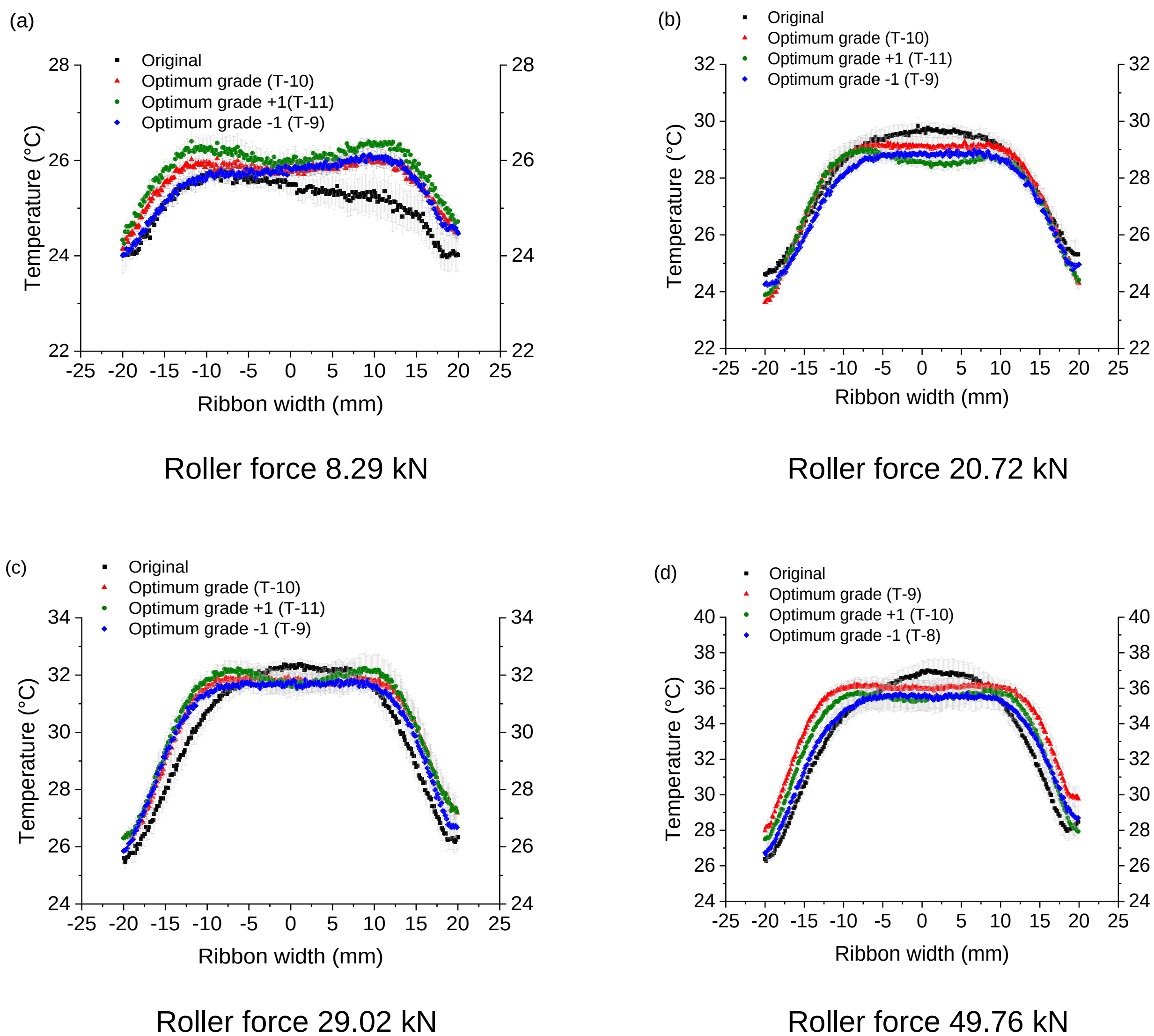

Figure 6-7. Temperature distribution profiles of Pharmatose ® 200M under different roller forces.

As the roller force increases to 20.72 kN as shown in Figure 6-7 (b), more stress has been applied to the powder, which results in the increase of the ribbon temperature (more heat generated in the compaction process). Comparing to the temperature distribution profiles of original guiders, the three feeding guiders contribute to a wider range of flat profiles which indicates the more uniform temperature distribution across the ribbon width. Moreover, when the feeding guiders of optimum grade +1 (T-11) are used, the temperature drops significantly at the centre of the ribbon. That means powders are over guided from the centre to the sides between the rollers, and it becomes non-uniform distribution again. Thus, the optimum grade of feeding guiders is T-10, which gives the flattest temperature profile under the roller force of 20.72 kN.

Figure 6-7 (c) illustrates that the original guiders result in about 7°C difference between the maximum and minimum temperature across the ribbon width under the roller force of 29.02 kN. That temperature difference decreases to around 6°C as the feeding guiders are used. The temperatures at the ribbon centre of original guiders are higher than that of the three feeding guiders. Meanwhile, the temperature at the parts between the centre and side of the ribbon for the original guiders are lower than those from feeding guiders. The reason is that non-uniform powder distribution from original guiders causes more powder compressed at the roller centre and less at the roller sides; feeding guiders improve the powder distribution by pushing them from the centre to the sides of the rollers. Thus, the temperature increases at the parts between the centre and side of the ribbon using the feeding guiders. Overall, Figure 6-7 (c) showed that the temperature profiles of optimum grade (T-10) have a wider range of flat parts across the ribbon width.

Figure 6-7 (d) shows a significant temperature difference among each profile of original guiders and feeding guiders under the roller force of 49.76 kN. As the feeding guiders of optimum grade -1 (T-8), optimum grade (T-9) and optimum grade +1 (T-10) are used, the temperature difference between the centre and side of the ribbon decrease to approximate 8°C, which is lower than the original guiders with about 11°C. Optimum grade (T-9) contributes to a more uniform temperature distribution than that of optimum grade -1 (T-8) and optimum grade +1 (T-10), which is displayed as the broader range of flat temperature profile.

Relative temperature uniformity across the ribbon width

Relative temperature uniformity is a way to indicate the uniformity of ribbon quality across the width. Figure 6-8 shows relative temperature uniformity of original guiders and feeding guiders under different roller forces. Overall, it is clear that the feeding guiders contributed to a significant increase in the relative temperature uniformity comparing to the original guiders. With an increase of the roller force from 8.29 kN to 49.76 kN as shown in Figure 6-8, feeding guiders of optimum grade -1 result in an increase of the relative temperature uniformity to around 28%, 38%, 50% and 45%, which is higher than that of the original guiders. Optimum grade contributes to the relative temperature uniformity increasing to approximately 72%, 62%, 57% and 55% with the increasing roller force. However, optimum grade +1 result in an increase in the relative temperature uniformity to about 40%, 45%, 28% and 50% under the four roller forces.

Therefore, the optimum grades of feeding guiders are T-10, T-10, T-10 and T-9, respectively for the roller force of 8.29 kN, 20.72 kN, 29.02 kN and 49.76 kN.

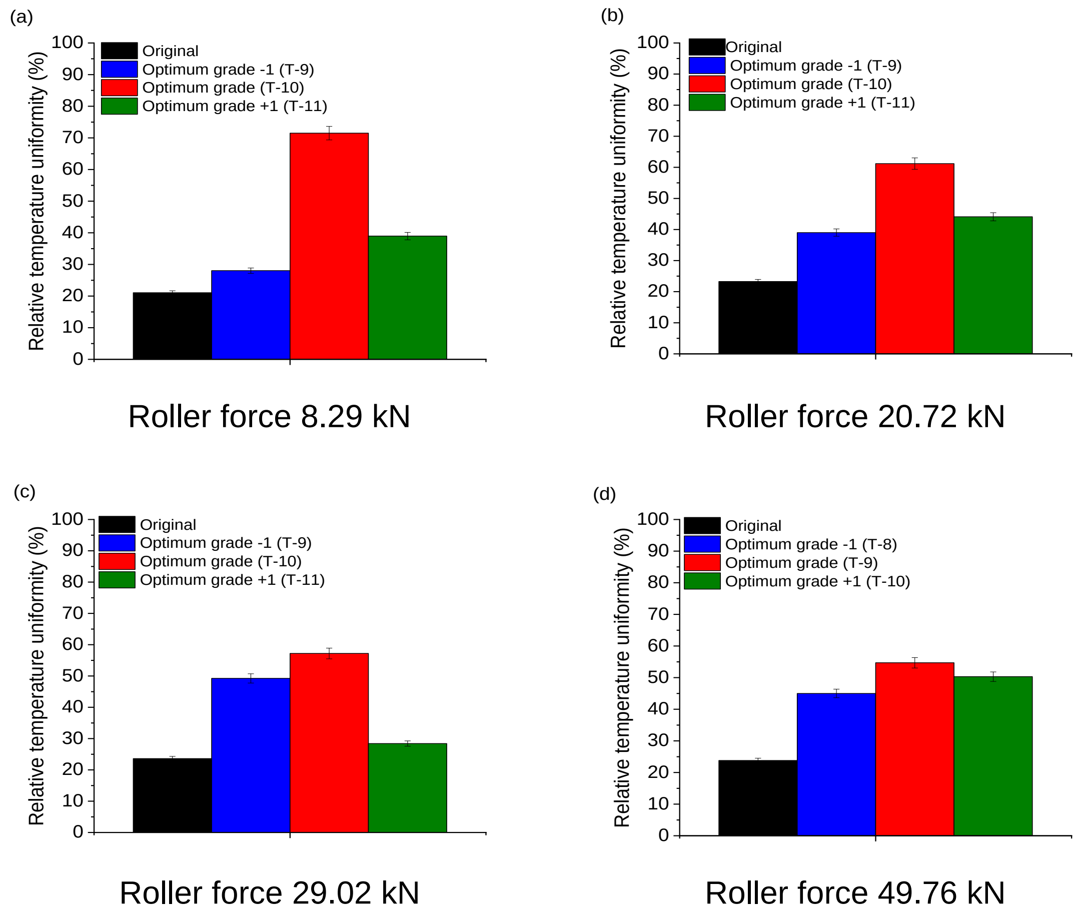

Figure 6-8. Relative temperature uniformity of Pharmatose ® 200M under different roller forces.

6.4.2.2 Avicel ® PH101 MCC

Temperature distribution profiles across the ribbon width

The feeding guiders contribute more uniform temperature profiles than the original guiders, as shown in Figure 6-9. For instance, Figure 6-9 (a) illustrates that there is about 4°C difference between the centre and side of the ribbon from the original guiders because of non-uniform powder distribution in the compaction zone. The feeding guiders of optimum grade (T-10) contribute to more uniform powder distribution, which is represented as a flatter temperature profile (red scatters) than the other feeding guiders (optimum grade -1 (T-9) and optimum grade +1 (T-11)). Optimum grade (T-10) results in an approximate 1°C difference between the centre and side of the ribbon.

As the roller force increases to 20.72 kN, comparing Figure 6-9 (b) to Figure 6-9 (a), the temperature of the ribbon increases due to more powders fed and compressed in the compaction zone than that at a lower roller force. In Figure 6-9 (b), the difference between the maximum and minimum ribbon temperature reduces from about 5°C (original guiders) to 2°C (feeding guiders). Comparing to original guiders The feeding guiders of optimum grade -1 (T-6) and optimum grade (T-7) contribute to a flatter temperature distribution profile. Moreover, as the grade of feeding guiders increases to T-8, the temperature distribution profile shows a bimodal trend which indicates that less powders are compressed at the roller centre than that at the parts close to the centre.

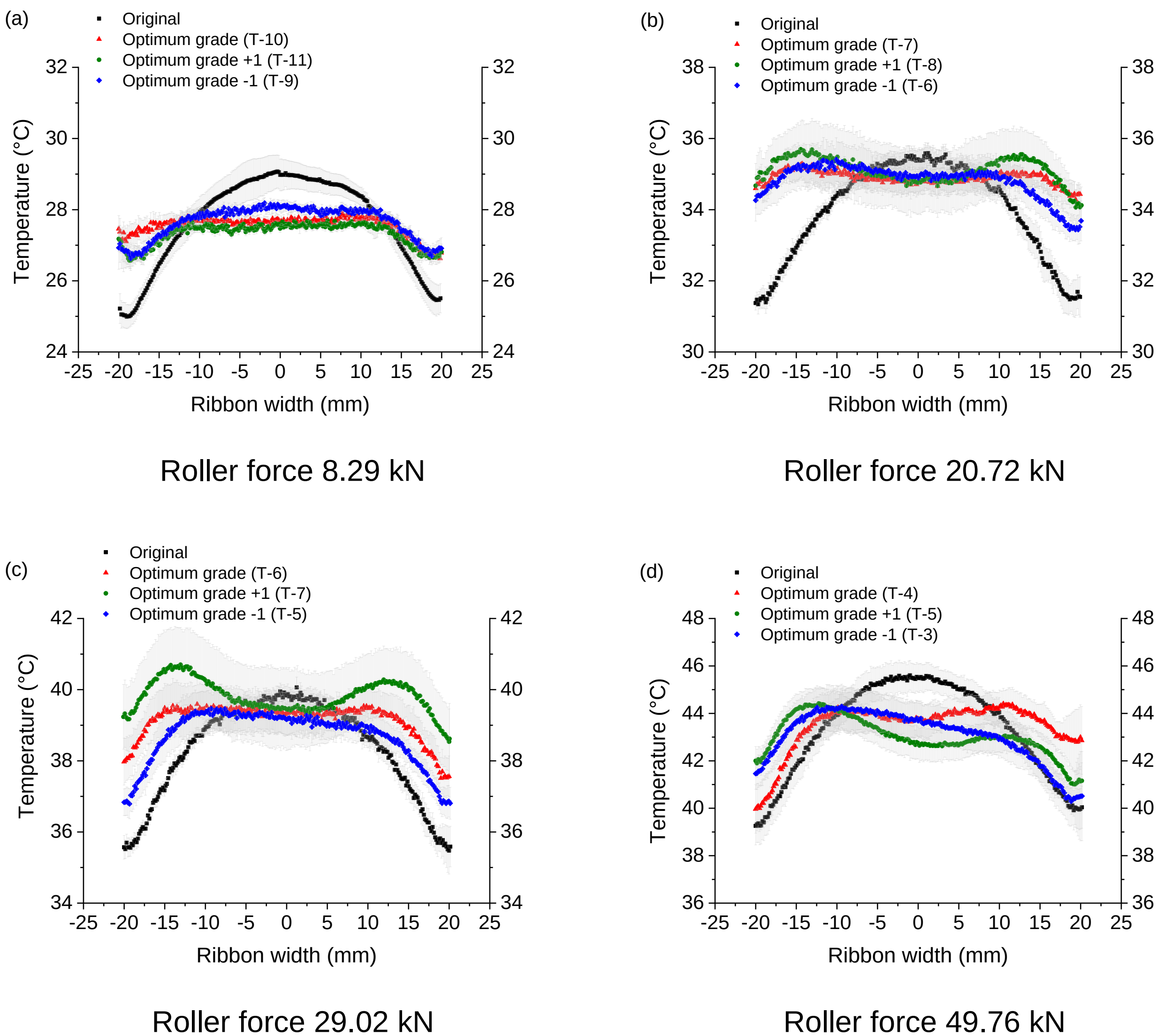

Figure 6-9. Temperature distribution profiles of Avicel ® PH101 MCC under different roller forces.

When it comes to the roller force of 29.02 kN and 49.76 kN, as shown in Figure 6-9 (c) and (d), feeding guiders contribute to a more uniform temperature distribution across the ribbon width in comparison to that of the original guiders. The original guiders result in the differences about 5°C and 7°C between the maximum and minimum ribbon temperature under the roller force of 29.02 kN and 49.76 kN. Feeding guiders of optimum grade -1 and optimum grade lead to a more uniform temperature distribution across the ribbon width than that of the original guiders. Figure 6-9 (c) shows that the differences between the maximum and minimum ribbon temperature are approximate 2°C and 1.5°C respectively for the optimum grade -1 and optimum grade. Figure 6-9 (d) illustrates that the differences between the maximum and minimum ribbon temperature are approximate 4°C for the optimum grade -1 and optimum grade. However, the optimum grade +1 show bimodal temperature distribution across the ribbon width in Figure 6-9 (c) and (d), which is beyond the optimum limit of optimising the powder uniform distribution in the compaction zone.

Relative temperature uniformity across the ribbon width

In Figure 6-10, it is clear to see that by using feeding guiders, the relative temperature uniformity has been improved to about twice than that of the original guiders. Moreover, the increase of roller force results in the decrease of the temperature uniformity using the original guiders, which decreased from approximately 30%, 23%, 18%, to 15% respectively from Figure 6-10 (a), (b), (c) to (d).

Figure 6-10 (a) illustrates that under the roller force of 8.29 kN, the feeding guiders of optimum grade -1 (T-9), optimum grade (T-10) and optimum grade +1 (T-11) contribute to 48%, 80% and 70% of relative temperature uniformity, which are higher than that from original guides with 30%. Figure 6-10 (b) displays that under the roller force of 20.72 kN, the feeding guides of optimum grade -1 (T-6), optimum grade (T-7) and optimum grade +1 (T-8) contribute to 55%, 75%, 35% of relative temperature uniformity, which is higher than that of original guiders with 23%.

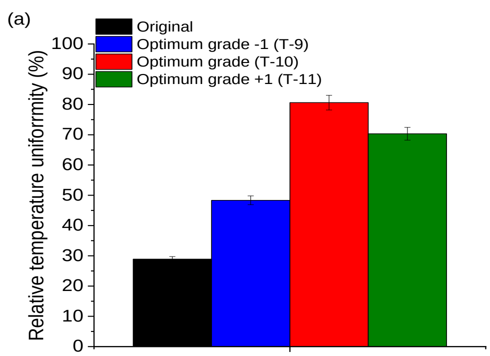

Roller force 8.29 kN

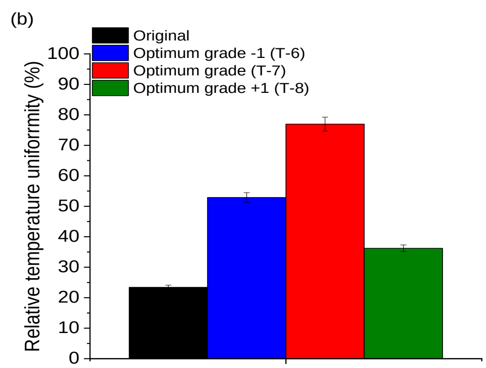

Roller force 20.72 kN

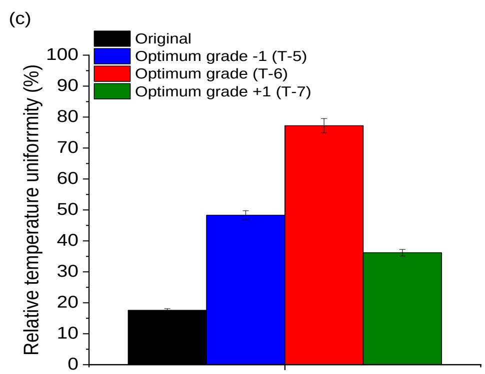

Roller force 29.02 kN

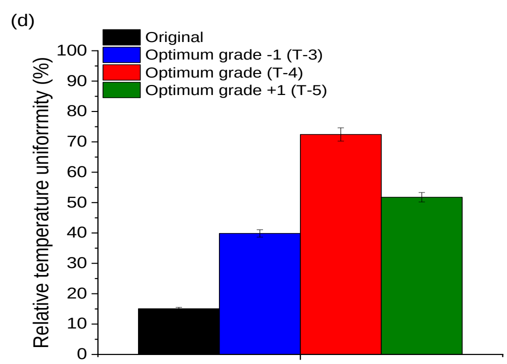

Roller force 49.76 kN

Figure 6-10. Relative temperature uniformity under different roller forces of Avicel ® PH101 MCC.

Similarly, under the roller force of 29.02 kN as shown in Figure 6-10 (c), the relative temperature uniformity has been improved to 50%, 75%, 35% using the feeding guiders of optimum grade -1 (T-5), optimum grade (T-6) and optimum grade +1 (T-7) which is more than two times than that of original guiders. Figure 6-10 (d) shows a significant increase in relative temperature uniformity with 40% (T-3), 70% (T-4) and 50% (T-5) under the roller force of 49.76 kN, that is higher than original guiders. As a result, the optimum grades of feeding guiders are T-10, T-7, T-6 and T-4, respectively for the roller force of 8.29 kN, 20.72 kN, 29.02 kN and 49.76 kN.

6.4.2.3 Tylopur ® 603 HPMC

Temperature distribution profiles across the ribbon width

Figure 6-11 shows that as the roller force increases from 8.29 kN to 49.76 kN, the original guiders contribute to an increase of temperature difference between the maximum and minimum ribbon temperature across the width. For instance, under the roller force of 8.29 kN, the original guiders result in about 3°C difference between the centre and side of the ribbon. When the roller force increases to 20.72 kN, 29.02 kN and 49.76 kN, the temperature difference increases to approximate 6°C, 7°C, and 10°C respectively. Thus, the non-uniform temperature distribution (powder distribution) becomes more significant as the roller force increases.

Figure 6-11 (a) shows that feeding guiders contribute to more uniform temperature than that of original guiders under the roller force of 8.29 kN. The temperature profile of the feeding guiders of optimum grade (T-11) is showing more flat/uniform than that of optimum grade -1 (T-10) and optimum grade +1 (T-12). When it comes to the roller force of 20.72 kN as shown in Figure 6-11 (b), the feeding guiders of optimum grade -1 (T-9) and optimum grade (T-10) lead to a flatter temperature profile comparing to the original guiders. However, the optimum grade +1 (T-11) results in a significant bimodal temperature profile across the ribbon width.

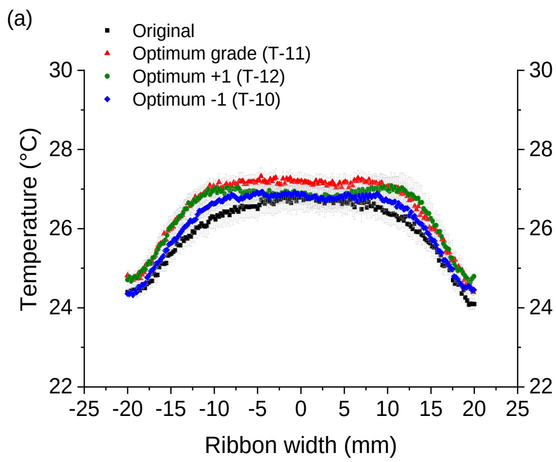

Roller force 8.29 kN

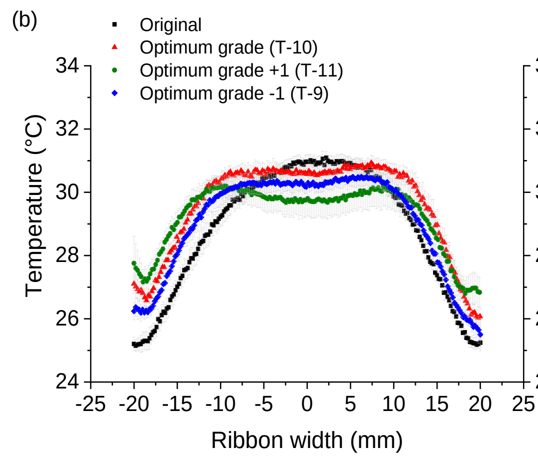

Roller force 20.72 kN

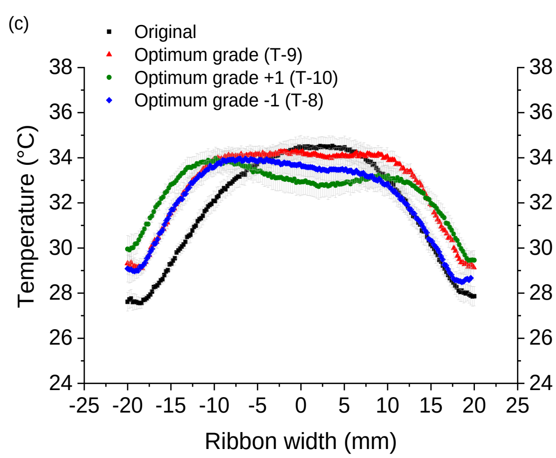

Roller force 29.02 kN

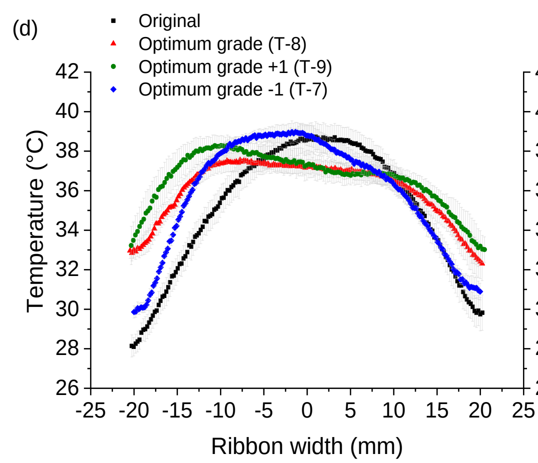

Roller force 49.76 kN

Figure 6-11. Temperature distribution profiles of Tylopur ® 603 HPMC under different roller forces.

As for the roller force of 29.02 kN, as shown in Figure 6-11 (c), feeding guiders of optimum grade (T-9) contribute to the broader range of flat parts in temperature profile in comparison to that of original guiders, optimum grade -1 (T-8) and optimum grade +1 (T-10). While under the roller force of 49.76 kN as displayed in Figure 6-11 (d), the feeding guiders of optimum grade -1 (T-7), optimum grade (T-8) and optimum grade +1 (T-9) lead to an increase on the temperature at the parts between the centre and side of ribbon compared to that of original guiders. Moreover, the feeding guider of optimum grade (T-8) contributes to more uniform temperature distribution across the ribbon width comparing to the other two feeding guiders.

Relative temperature uniformity across the ribbon width

Figure 6-12 shows that the improvement of the relative temperature uniformity using feeding guiders. The relative temperature uniformity of feeing guiders increases at least twice than that of the original guiders. For example, Figure 6-12 (a) illustrates that under the roller force of 8.29 kN, the feeding guiders of optimum grade -1 (T-10), optimum grade (T-11) and optimum grade +1 (T-12) have improved the relative temperature uniformity to about 55%, 65% and 60% compared to the original guiders with 25%. Overall, the three feeding guiders contribute to more than half width of the ribbon, achieving uniform temperature.

Figure 6-12 (b) demonstrates that under the roller force of 20.72 kN, the relative temperature uniformity has been improved to about 35%, 55%, 35% respectively using optimum grade (T-10), optimum grade -1 (T-9) and optimum grade +1 (T-11), which is more than twice than the original guiders with around 22%.

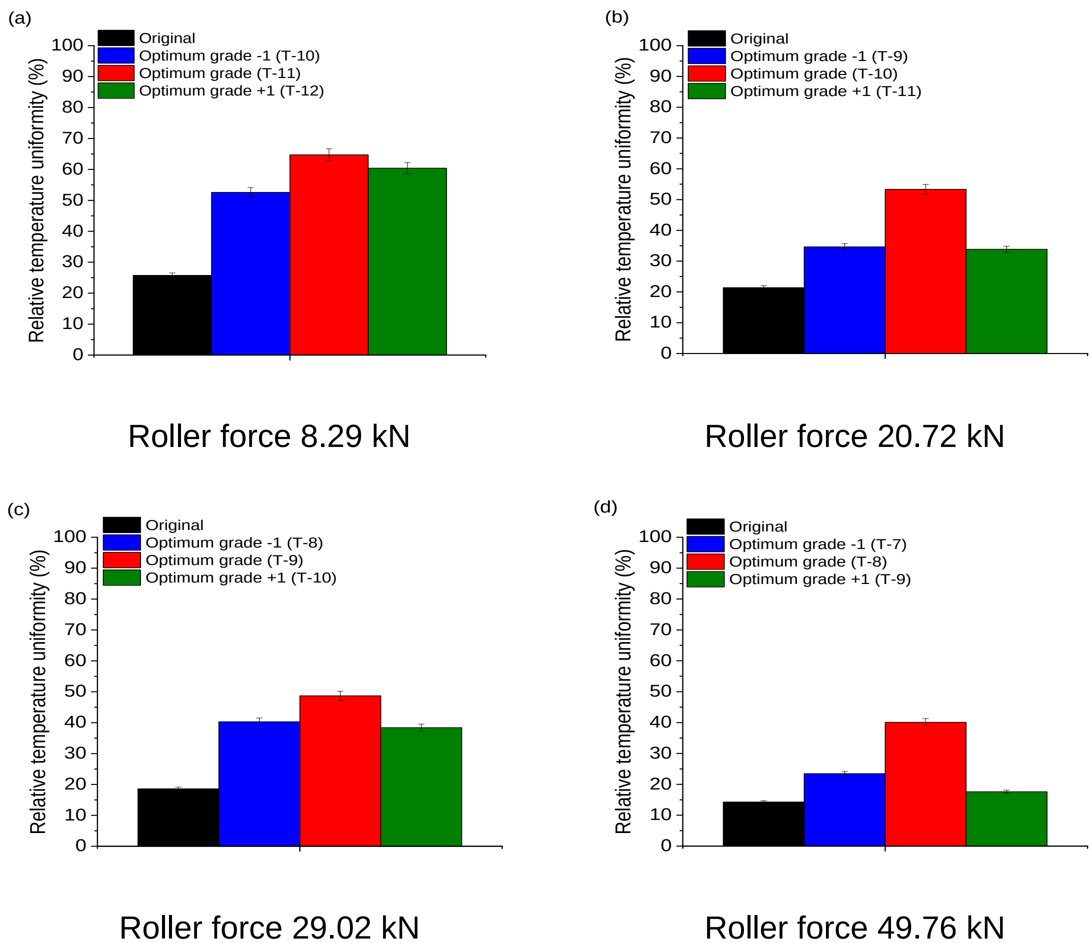

Figure 6-12. Relative temperature uniformity under different roller forces of Tylopur ® 603 HPMC.

As the roller force increases to 29.02 kN and 49.76 kN as illustrated in Figure 6-12 (c) and (d), feeding guiders of optimum grade (T-9, T-8) contribute to the increasing relative temperature uniformity to 50% and 40%. Meanwhile, the optimum grade -1 contributes to the increasing relative temperature uniformity to 40% and 30%; the optimum grade +1 (T-10, T-9) contributes to the increasing relative temperature uniformity to 40% and 18%. However, the relative temperature uniformity of the original guiders are 20% and 15% respectively under the roller force increases of

29.02 kN and 49.76 kN. Furthermore, it can be summarised that T-10, T-9, T-8 and T-7 are the optimum grades respectively for the roller force of 8.29 kN, 20.72 kN, 29.02 kN and 49.76 kN.

6.4.2.4 Light Sodium Carbonate

Temperature distribution profiles across the ribbon width

Under the roller force of 8.29 kN, as shown in Figure 6-13 (a), the temperature profiles of three feeding guiders and original guiders are overlapping with a slight difference. The temperature distribution of T-13 shows more uniform at the centre of the ribbon in comparison to the other feeding guiders. When the roller force comes to 20.72 kN as illustrated in Figure 6-13 (b), feeding guiders of optimum grade -1 (T-9) show that the feeding guiders of optimum grade (T-10) contribute to a wider range of flat parts of the temperature profile comparing to the optimum grade -1 (T-9). However, the bimodal temperature profile is displayed for the optimum grade +1 (T-11).

Similarly, in Figure 6-13 (c) under roller force of 29.02 kN, comparing the feeding guiders of optimum grade -1 (T-7), optimum grade (T-8) and optimum grade +1 (T-9) to the original guiders, both of them contribute to more uniform temperature distribution at the ribbon centre than that of the original guiders. Moreover, the optimum grade (T-8) results in most uniform temperature distribution around the ribbon centre, which is better than the other feeding guiders.

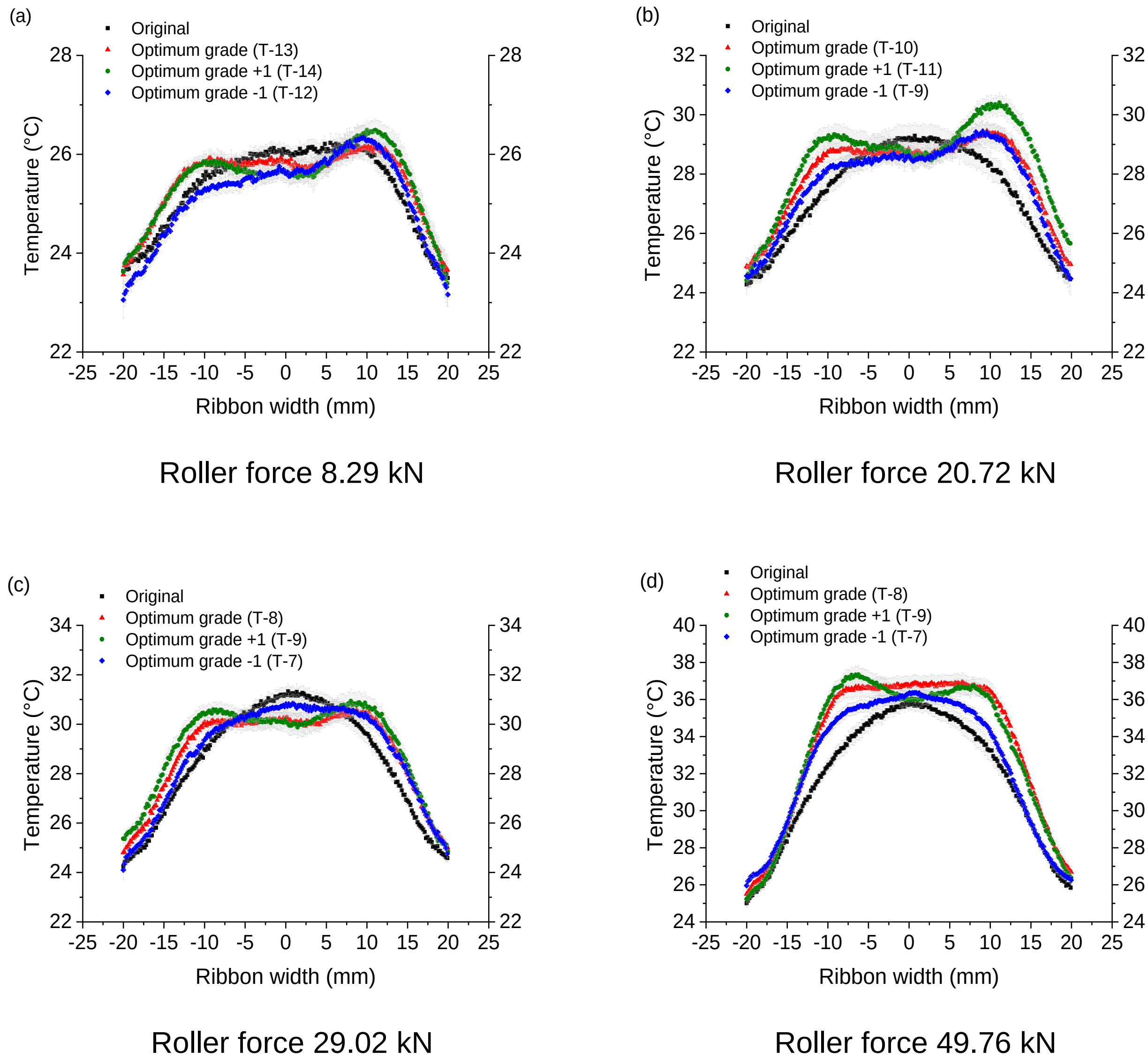

Figure 6-13. Temperature distribution profiles of Light Sodium Carbonate under different roller forces.

Additionally, Figure 6-13 (d) shows that the feeding guiders lead to more uniform temperature distribution across the ribbon width comparing to that of the original guiders. The optimum grade (T-8) results in the most uniform temperature distribution across the ribbon width comparing to the optimum grade -1 (T-7) and optimum grade +1 (T-9).

Relative temperature uniformity across the ribbon width

Figure 6-14 shows that as the roller force increases, the relative temperature uniformity of the original guiders decreases. In details of Figure 6-14 (a) with the roller force of 8.29 kN, the optimum grade -1 (T-12) and optimum grade (T-13) contributes to approximate 34% and 56% of relative temperature uniformity, which is higher than that of the original guiders (30%). Moreover, although the optimum grade +1 (T-14) causes bimodal temperature distribution across the ribbon width, it results in approximately 48% of relative temperature uniformity.

Figure 6-14 (b) shows that under the roller force of 20.72 kN, there is a significant difference in the relative temperature uniformity between three grades of feeding guiders and original guiders. For instance, the optimum grade -1 (T-9), the optimum grade (T-10) and optimum grade +1 (T-11) improve the relative temperature uniformity to about 35%, 50% and 30%, which are higher than the original guiders with 25%. As Figure 6-14 (c) and (d) show that under the roller force of 29.02 kN and 49.76 kN, the feeding guiders optimum grade (T-8) achieve the optimum relative temperature uniformity with 47 % and 43 % respectively; however, the original guiders cause less relative temperature uniformity with 12% and 10%. Besides, the feeding guiders optimum grade -1 (T-7) cause the improvement of relative temperature uniformity to 29% and 18% respectively under the roller force of 29.02 kN and 49.76 kN. Optimum grade +1 (T-9) leads to an increase in the relative temperature uniformity to 30% and 15%, in comparison to that of original guiders. Therefore, the optimum grades of feeding guiders are T-13, T-10, T-8 and T-8, respectively for the roller force of 8.29 kN, 20.72 kN, 29.02 kN and 49.76 kN.

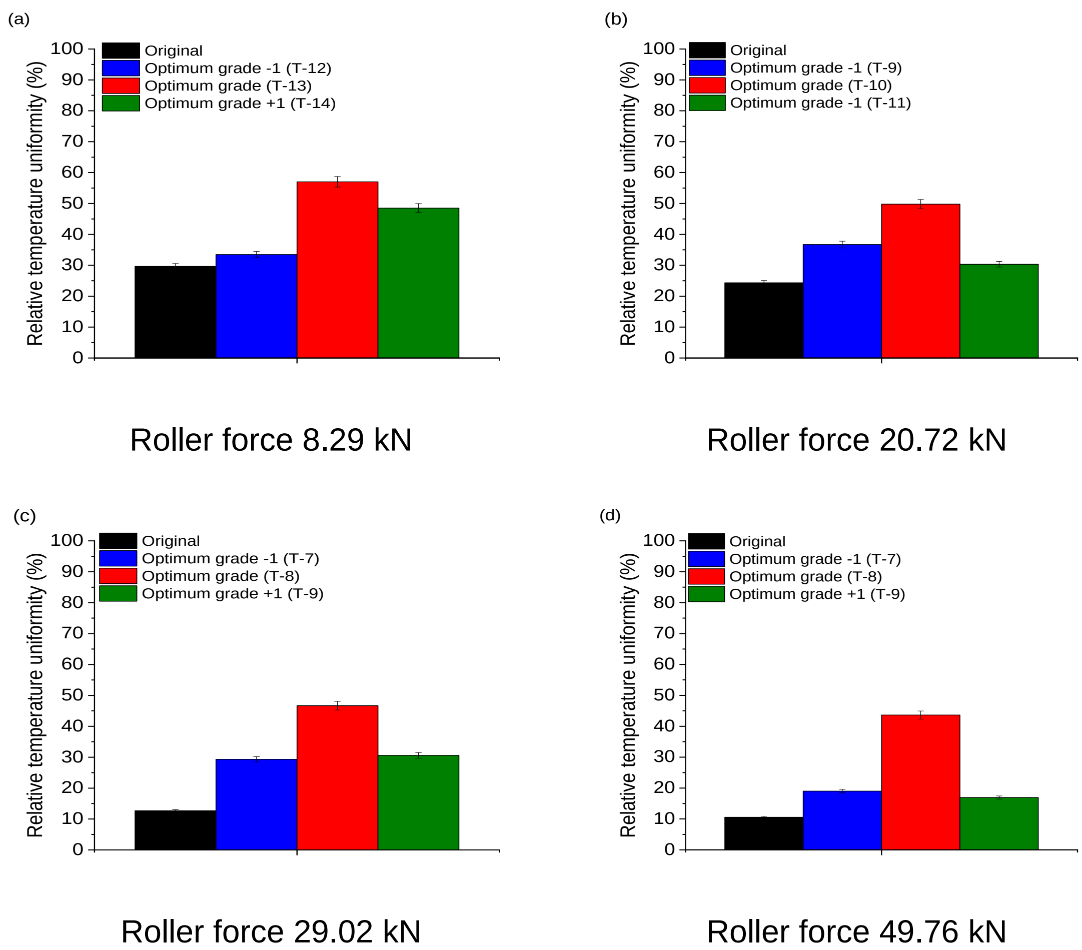

Figure 6-14. Relative temperature uniformity of Light Sodium Carbonate under different roller forces.

6.4.2.5 GLUCIDEX ® Maltodextrin DE6

Temperature distribution profiles across the ribbon width

In Figure 6-15 (a), it shows that under the roller force of 8.29 kN, there is a slight difference (slightly overlapping) in temperature distribution profiles of three feeding guiders and original guiders. The feeding guiders of optimum grade +1 (T-11) result in a slightly bimodal temperature profile (the slightly higher temperature at the parts between the centre and side of ribbon). Optimum grade +1 (T-10) causes a relatively more uniform temperature distribution across the ribbon width comparing to the other feeding guiders under the roller force of 8.29 kN. Next, with the roller force of 20.72 kN, Figure 6-15 (b) illustrates that comparing to the original guiders, three feeding guiders contribute to an increase in the temperature at the parts between the centre and side of the ribbon. The difference between the maximum and minimum ribbon temperature is 1°C using optimum grade (T-7), which is lower than that of the original guiders (2°C). The feeding guiders of optimum grade (T-7) show a wider range of flat temperature profile than the optimum grade -1 (T-6) and optimum grade +1 (T-8). Moreover, the optimum grade +1 (T-8) shows a bimodal temperature profile.

As the roller force increases to 29.02 kN as shown in Figure 6-15 (c), the optimum grade -1 (T-5), optimum grade (T-6) and optimum grade +1 (T-7) contribute to the temperature difference with about 3°C between the maximum and minimum ribbon temperature across the width, which is less than that of original guiders with around

5°C. Optimum grade +1 (T-7) contributes to a more uniform temperature profile across the ribbon width in comparison to that of the other feeding guiders.

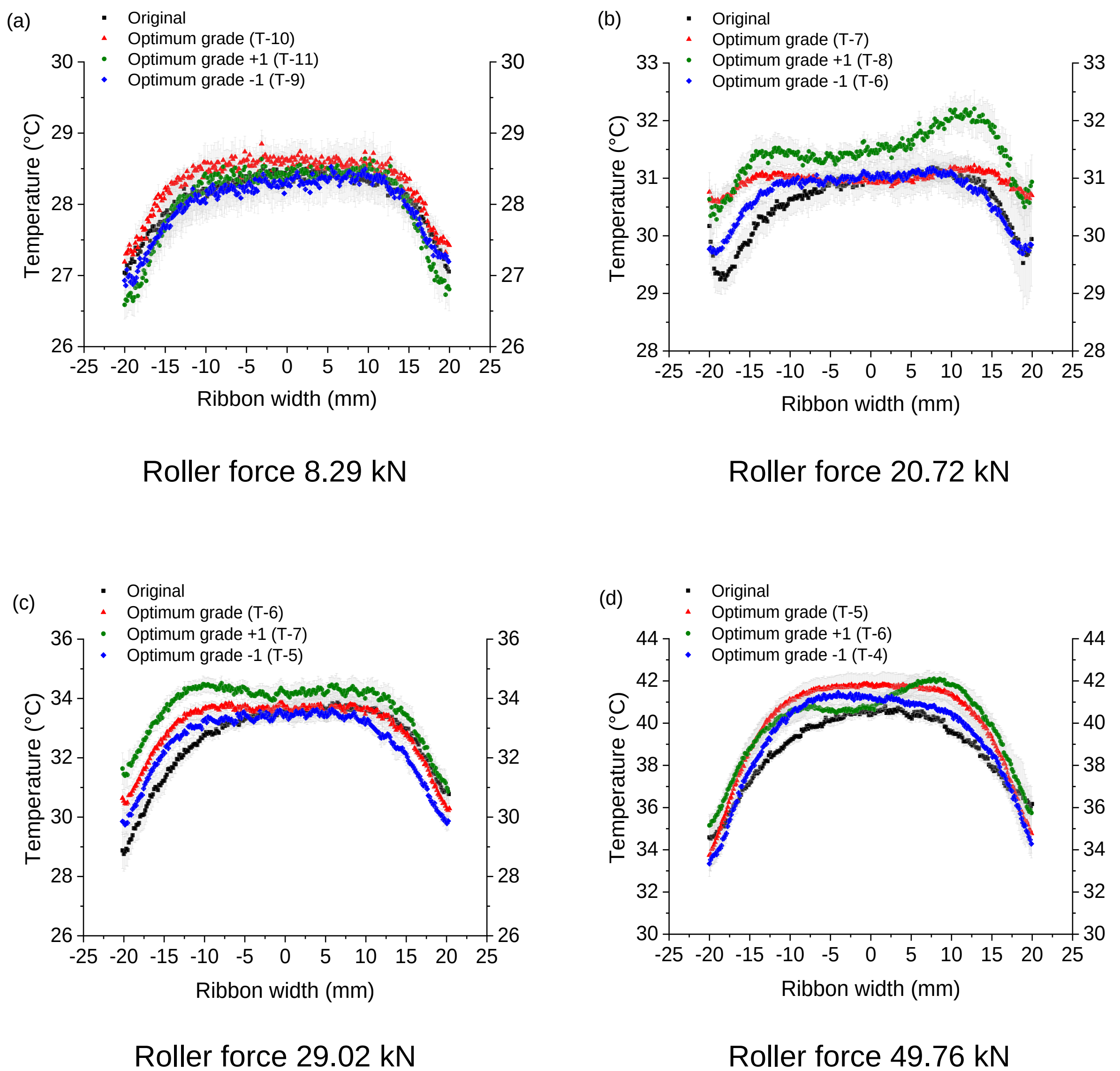

Figure 6-15. Temperature distribution profiles of GLUCIDEX ® Maltodextrin DE6 under different roller forces.

When the roller force comes to the 49.76 kN in Figure 6-15 (d), feeding guiders lead to more uniform temperature distribution across the ribbon width compared to original guiders. For example, feeding guiders of optimum grade (T-5) and optimum grade +1 (T-6), result in a wider range of the increased temperature; however, the optimum grade +1 (T-6) leads to a bimodal temperature profile with the decrease of temperature at the ribbon centre. Thus, the T-5 is the optimum grade of feeding guiders under the roller force of 49.76 kN.

Relative temperature uniformity across the ribbon width

As shown in Figure 6-16 (a) with roller force of 8.29 kN, the feeding guiders of optimum grade -1 (T-9), optimum grade (T-10) and optimum grade +1 (T-11) cause the increases in the relative temperature uniformity to approximate 60%, 67% and 52%, which is higher than that of the original guiders (47%). As the roller force increases, the relative temperature uniformity decreases due to the increasing difference in the amount of feeding powder across the roller width in the compaction zone. When the roller force comes to 20.72 kN as shown in Figure 6-16 (b), the relative temperature uniformity increases to 50% using the optimum grade -1 (T-6), 65% using optimum grade (T-7) and 57% using optimum grade +1 (T-8). Moreover, the original guiders have a lower value with 43% of relative temperature uniformity.

Furthermore, under the roller force of 29.02 kN in Figure 6-16 (c), the feeding guiders of optimum grade -1 (T-5), optimum grade (T-6) and optimum grade +1 (T-7) contribute to 47%, 60% and 38% of the relative temperature uniformity, which is higher than that of the original guiders (37%). In addition, Figure 6-16 (d) illustrates that as the roller force increases to 49.76 kN, the relative temperature uniformity of the original guiders decreases to about 22%. The increase of feeding guider grade (from T-4, T-5 to T-6) results in the relative temperature uniformity increasing to approximately 33%, 41% to 29% as displayed in Figure 6-16 (d). Therefore, the optimum grades of feeding guiders are T-10, T-7, T-6 and T-5, respectively for the roller force of 8.29 kN, 20.72 kN, 29.02 kN and 49.76 kN.

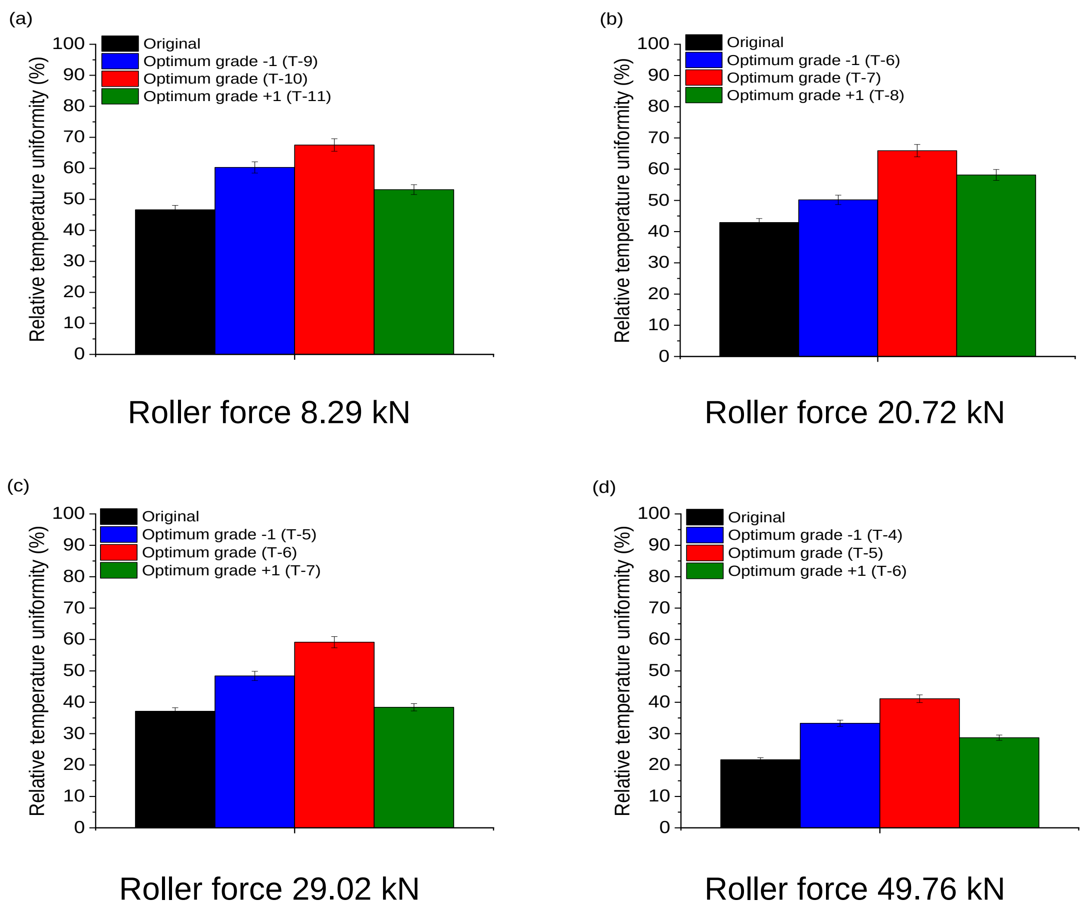

Figure 6-16. Relative temperature uniformity of GLUCIDEX ® Maltodextrin DE6 under different roller forces.

6.4.2.6 Starch 1500

Temperature distribution profiles across the ribbon width

From Figure 6-17, the temperature profile from the original guiders is with a higher temperature at the ribbon centre and lower temperature at the sides of the ribbon. As the three grades of feeding guiders are used in the roller compaction, the temperature distribution across the ribbon width has been improved to be more uniform than that from original guiders under the roller force of 8.29 kN, 20.72 kN, 29.02 kN and 49.76 kN, as shown in Figure 6-17.

Figure 6-17 shows that compared to the optimum grade -1 and optimum grade +1, optimum grade causes the flattest profile (most uniform) of ribbon temperature distribution across the ribbon width. Comparing the original guiders, the difference between the maximum and minimum ribbon temperature decreases to 1°C under the roller force of 8.29 kN and 20.72 kN. Meanwhile, the difference drops to 2°C and 3°C respectively under the roller force of 29.02 kN and 49.76 kN.

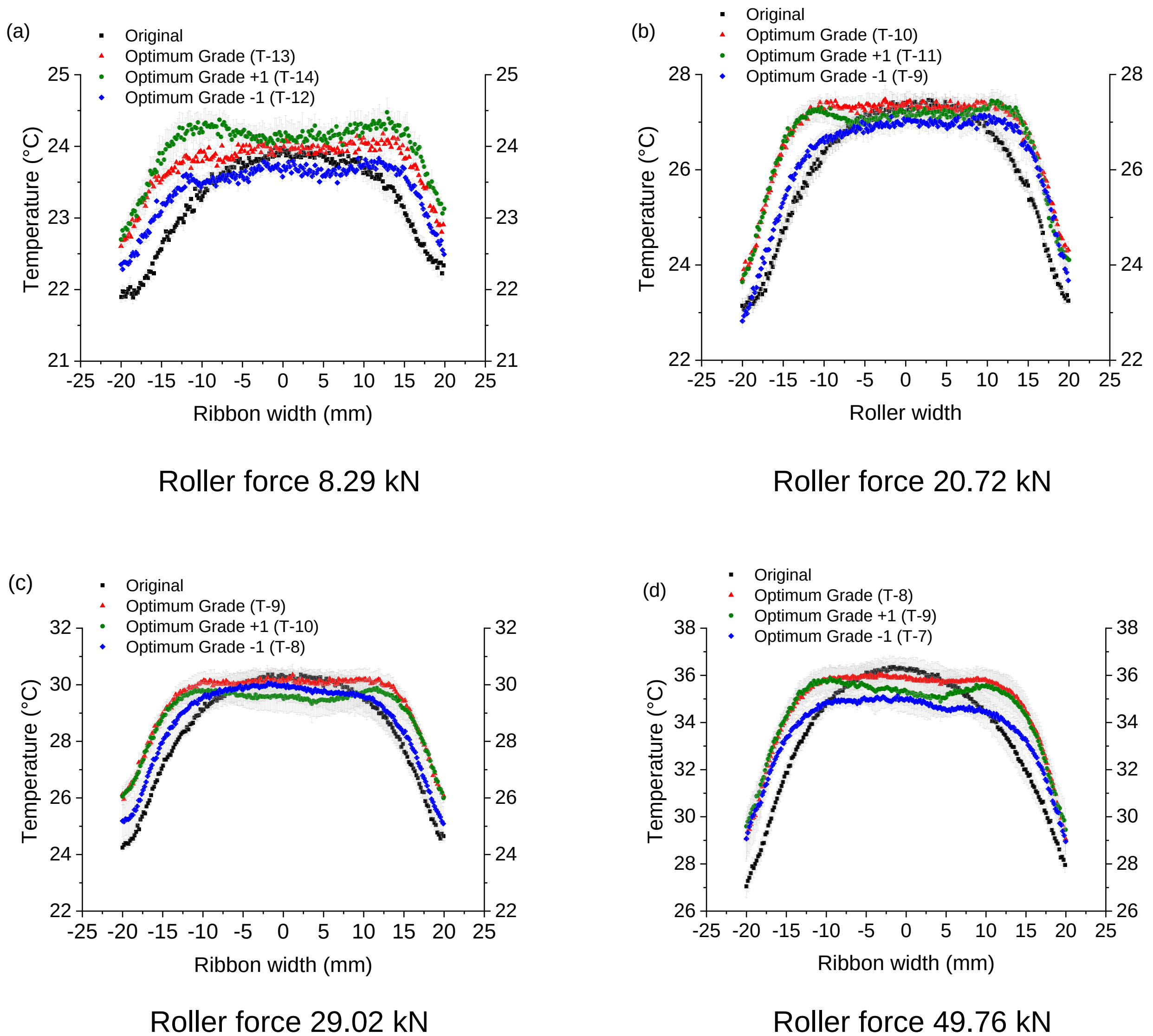

Figure 6-17. Temperature distribution profiles of Starch 1500 under different roller forces.

Relative temperature uniformity across the ribbon width

As displayed in Figure 6-18 (a) with roller force of 8.29 kN, the feeding guiders contribute to significantly higher relative temperature uniformity compared with that of the original guiders. Figure 6-18 (a) shows that the optimum grade -1 (T-12) and optimum grade +1 (T-14) leads to about 50% of relative temperature uniformity which is higher than the original guiders (27%). The optimum grade (T-13) contributes to the highest relative temperature uniformity with 65%.

Figure 6-18 (b) illustrates that the relative temperature uniformity of original guiders and three feeding guiders under the roller force of 20.72 kN. As the grade of feeding guiders increases from T-9 (optimum grade -1), T-10 (optimum grade) to T-11 (optimum grade +1), relative temperature uniformity are approximately 50%, 65%, and 60%, which are 25%, 40% and 35% higher than that of original guiders (25%). Thus, the T-10 is the optimum grade for the feeding guiders under the roller force of 20.72 kN.

As the roller force increases to 29.02 kN, as shown in Figure 6-18 (c), the feeding guiders of optimum grade -1 (T-8), optimum grade (T-9) and optimum grade +1 (T-10) contribute to an increase in the relative temperature uniformity to approximate 45%, 65% and 60% compared with the original guiders (about 25%).

In addition, Figure 6-18 (d) illustrates that under the roller force of 49.76 kN, the feeding guiders of optimum grade -1 (T-7), optimum grade (T-8) and optimum grade +1 (T-9) improve the relative temperature uniformity to about 52%, 60% and 57%, which is higher than the original guider with 25%.

Consequently, the optimum grades of feeding guiders are T-13, T-10, T-9 and T-8, respectively for the roller force of 8.29 kN, 20.72 kN, 29.02 kN and 49.76 kN.

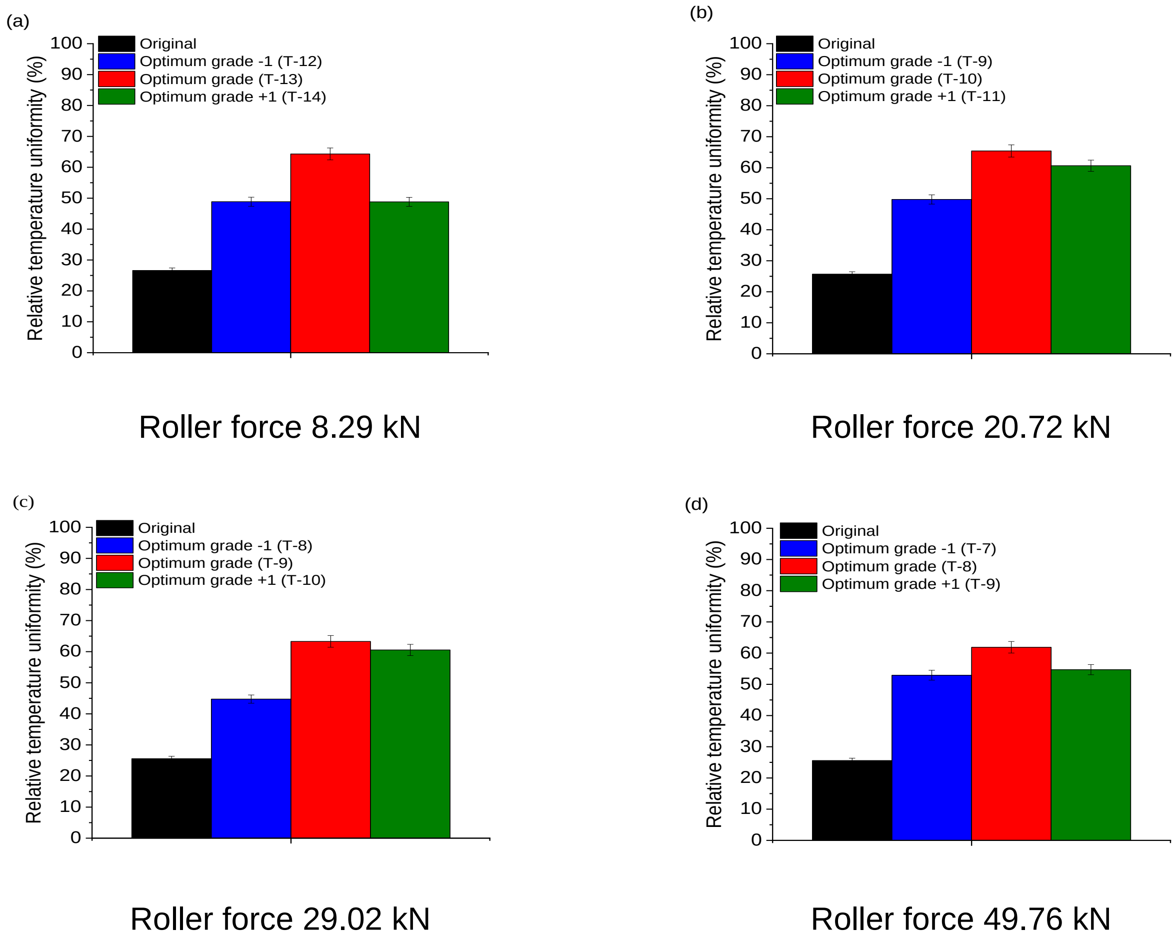

Figure 6-18. Relative temperature uniformity under different roller force of Starch 1500 under different roller forces.

6.4.2.7 Summary on relative temperature uniformity across the ribbon width

The optimum relative temperature uniformity of materials varies with the roller force and material property, as illustrated in Figure 6-19. Figure 6-19 is showing that there is a significant increase in the percentage of relative temperature uniformity using the optimum feeding guider for all powders. This is due to the fact the feeding guiders improve the powder distribution across the roller width in the feeding and compaction zones and result in more uniform stress distribution. The more uniform stress distribution during compaction then results in the more uniform temperature distribution of the ribbon and therefore in a higher percentage of the relative temperature uniformity as shown in Figure 6-19. This improvement in the feeding and compaction behaviours using the guiders will then improve the ribbon and final granules properties.

It is worth noting that the increase in the force applied by the rollers to the powder results in a decrease in the percentage of the relative temperature uniformity. The is because the amount of powder increases with the increasing roller force, which results in a higher difference in the amount of powder exist at the roller centre and side. The feeding guiders push more powder towards the sides of the rollers, and the effect of the friction between the powder and cheek plate cannot be ignored. This decrease of the percentage of the relative temperature uniformity is not significant for Starch powder, which is a free-flowing material with higher flow function coefficient (ffc) in comparison to the other powders.

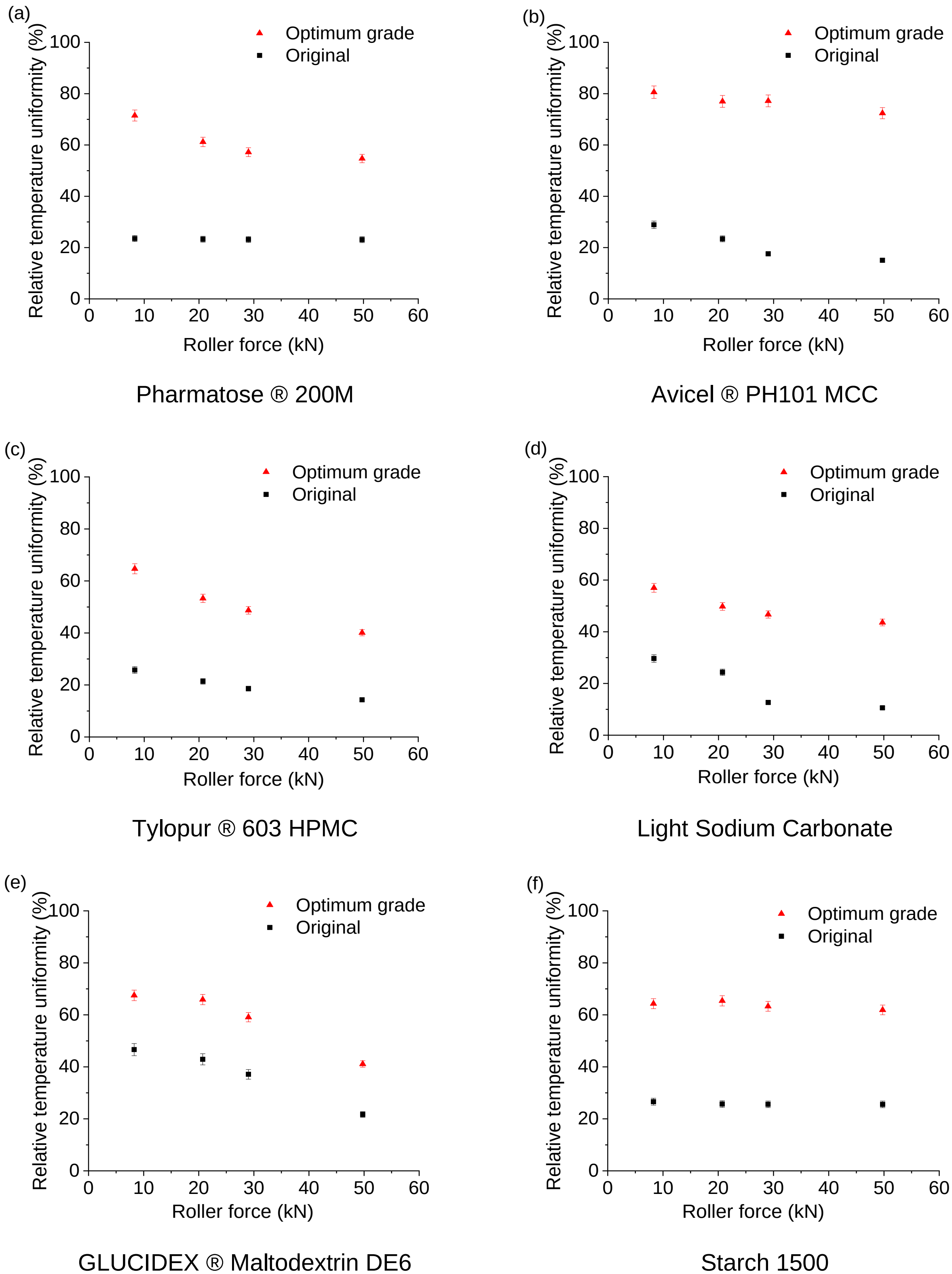

Figure 6-19. Optimum relative temperature uniformity of materials.

Figure 6-20 shows a design space with material flow properties (flow function coefficient - ffc), the dimension of guider height and relative temperature uniformity. This design space can be used to select the dimension of guiders to get the product with the most uniform quality when the powder flow function coefficient and roller forces are known.

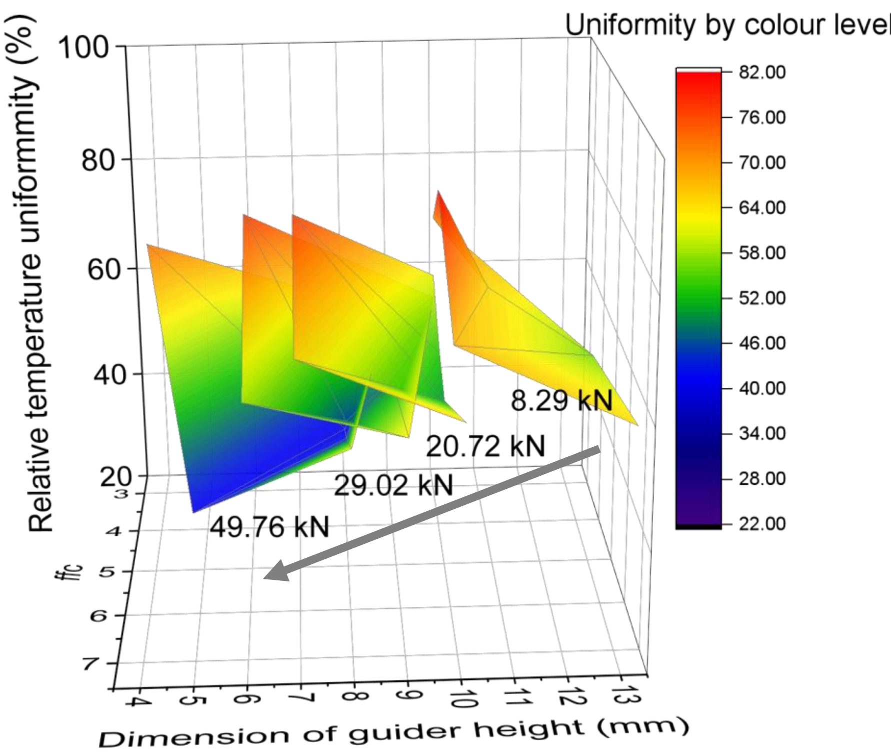

Figure 6-20. Design space of the material property, process parameter and uniformity of properties.

Overall, for a range of powder with different flow function coefficient, the higher the roller force, the smaller dimension of guider height required to achieve an optimum relative temperature uniformity. Besides, as for the same powder, the optimum relative temperature uniformity requires a reduced dimension of guider height as the roller force increased.

6.5 Conclusions

In this chapter, a novel design of feeding guider was proposed and used in the lab-scale roller compactor (side-sealing system) to improve the uniformity of the powder distribution from feeding to the compaction zone. The design of feeding guiders was with a range of grades (height) under the considerations of the powder flowability and process parameters involved in the design of experiments. The results determined the optimum relative temperature uniformity from the temperature distribution across the ribbon width using online thermal imaging.

As a result, the uniformity of the ribbon temperature of all powders has been improved with feeding guiders to a different extent under four roller forces. The overall relative temperature uniformity increased to about at least 40%, which is higher than that of original guiders. To obtain an optimum relative temperature uniformity, a higher flow function coefficient of powder required a lower guiders' height.

Consequently, the feeding guiders contributed to the improvements in the uniformity of the ribbon temperature. A design space graph was also developed for materials with different flowability, grades of feeding guider and roller forces, which is useful for the design of experiments and prediction of relative temperature uniformity of other materials.

Chapter 7 Investigating powder property along feeding to compaction with online and offline measurement in roller compaction

7.1 Introduction

In this chapter, online thermal imaging is used as a Process Analytical Technology (PAT) to monitor powder temperature along feeding to compaction direction with different roller forces in the roller compaction process. Powder temperature is captured online by a thermal camera. Also, X-ray is used as an offline measurement to examine the density distribution of the compacted powder body from the feeding to the compaction. The results of powder temperature profiles and density distribution are used to compare the nip angle with the value calculated from Johanson theory.

7.2 Methodology

7.2.1 Developing online monitoring method with the thermal camera

A modified design of side-sealing cheek plate is developed and assembled with the Germanium glass windows (Umicore company, UK), as shown in Figure 7-1, which could allow the thermal camera to capture the powder temperature, as described in Section 3.2.2.2. The windows locate along the centreline of the cheek plate. Once process parameters have been set up at the beginning, powders start to be driven by the horizontal screw feeder towards rollers. Experiments start to be recorded as the 0 s when powders approach the minimum gap.

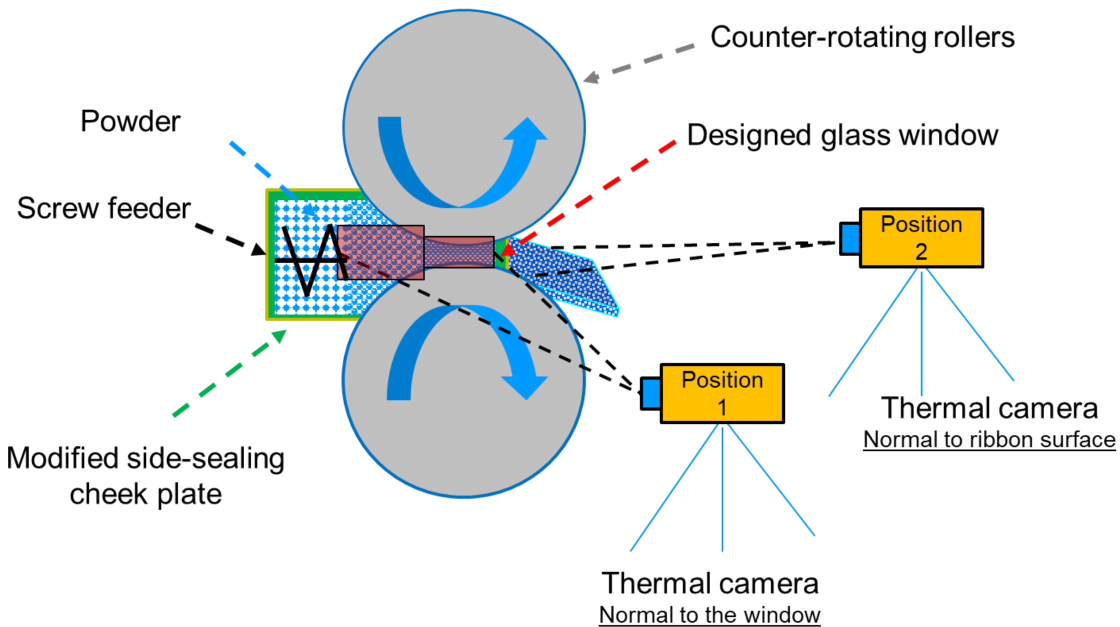

Figure 7-1. Setup design of new PAT method in roller compactor.

7.2.2 Porosity distribution along the feeding to the compaction zone

The porosity of ribbon is measured by X-ray tomography scanner - µCT 35 (SCANCO MEDICAL, Switzerland). The samples are collected when the process achieves the steady state from the same thermal imaging experiments. The compacted powder body is continuously scanned by plane through the centreline across the ribbon width and normal to the feeding to the compaction direction, as described in Section 3.2.3.2.

7.2.3 Roller compaction process parameters

The operating conditions are 3 rpm for the roller speed, 2 mm for the roller gap and roller force of 8.29 kN, 12.44 kN, 16.58 kN and 20.72 kN. The auto gap control system is used, which means that in the beginning, the roller gap starts from 0 mm to 2 mm (setup point) with an adjusting screw speed until the steady state.

7.3 Results

The results include the effects of roller force on the temperature and density distribution of powder along the direction from feeding to the compaction.

7.3.1 Avicel ® PH101 MCC

7.3.1.1 Powder temperature distribution along feeding direction with time

Figure 7-2 to Figure 7-5 show the effect of roller forces on the powder temperature. Those figures are showing the temperature profiles every 10 seconds for the entire measurement from feeding zone (screw ending position) to the compaction zone (until ribbon exit) under the roller force from 8.29 kN to 20.72 kN. In Figure 7-2 to Figure 7-5, from the 0 s, when the roller gap gradually increases to 2 mm, more powders are fed to the roller gap and compacted. The more powders compacted, the more heat generated, which is representing as the increase of the temperature in Figure 7-2 to Figure 7-5. At 40 s, the roller force and roller gap achieve the steady state, the temperature of compacted powder becomes steady.

Figure 7-2 shows that at the roller force of 8.29 kN, the temperature along the measuring line is steady at 0 s, which is the temperature of feeding powder (free of stress from rollers). After 10 s, in the compaction zone, the temperature at the position of 0 mm is higher than that at 0 s, due to the increased stress applied to the powder (resulting in more heat generation). Figure 7-2 illustrates that in the first 40 s, the temperature at the position of 0 mm increases with time and then stays steady, which because the steady state needs time to achieve after initialling the process. As the compacted powder (ribbon) exits from the minimum gap between rollers, the temperature of compacted powder decreases due to the heat loss.

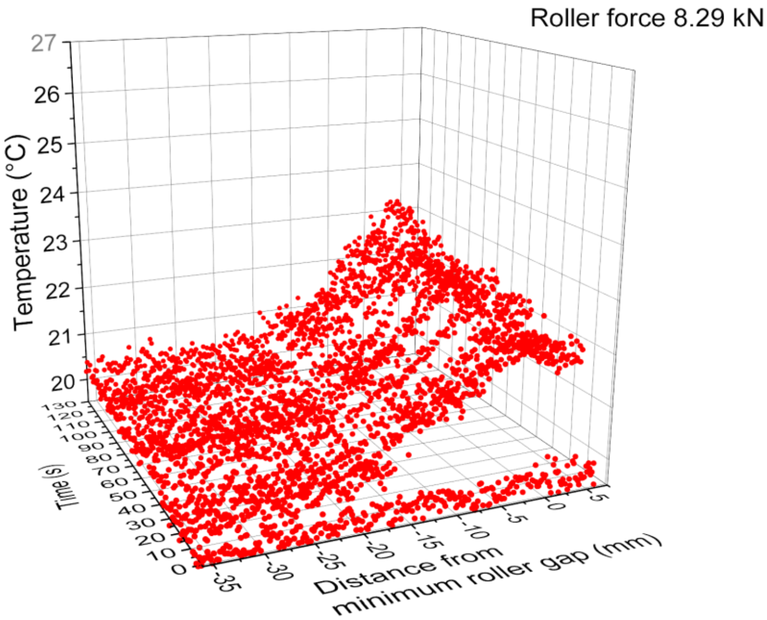

Figure 7-2. Temperature distribution along the feeding direction with time under the roller force of 8.29 kN.

As the roller force increases to 12.44 kN in Figure 7-3, the increase of stress applied to the powder contributes to a higher difference in temperature between the feeding and the compaction zone. The higher the stress applied to the powder, the more deformation of powder occurs, which results in more heat generation during the process.

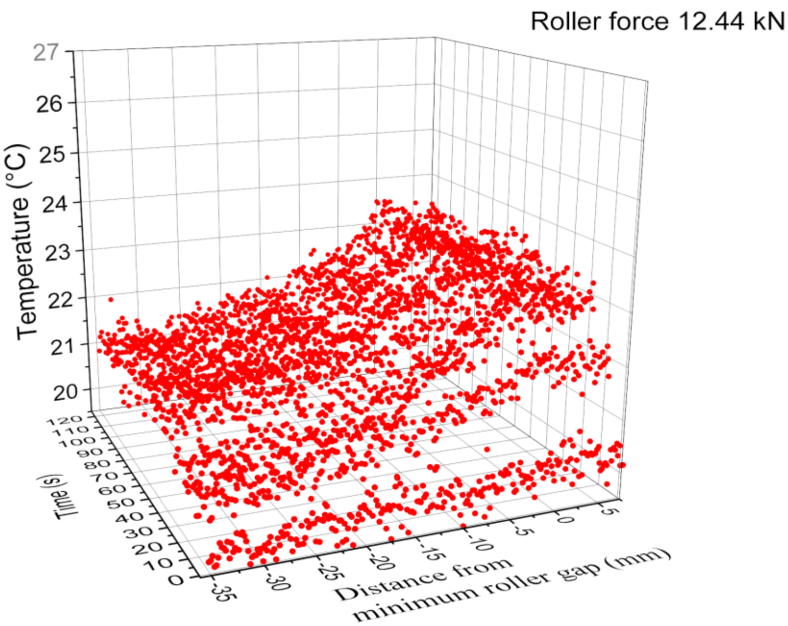

Figure 7-3. Temperature distribution along the feeding direction with time under the roller force of 12.44 kN.

Figure 7-3 shows that the maximum temperature locates at 0 mm on the axis (minimum roller gap). There is an approximate 3°C difference comparing the temperature at the beginning of the feeding zone to that at the minimum roller gap. As the ribbons exit from the minimum roller gap, the temperature decreases significantly. Also, comparing Figure 7-3 to Figure 7-2, the increased screw speed before steady state (28 rpm and 36 rpm respectively under the roller force of 8.29 kN and 12.44 kN) causes the increased powder temperature in the feeding zone.

In Figure 7-4 and Figure 7-5, at the initial status (0 s), powders are fed along the feeding to compaction direction, with a steady temperature. As the roller force increases, the more powders are required to fulfil and compacted between rollers, which contributes to more heat generated. Besides, the friction between the screw and powder contributes to the heat generated in the feeding zone.

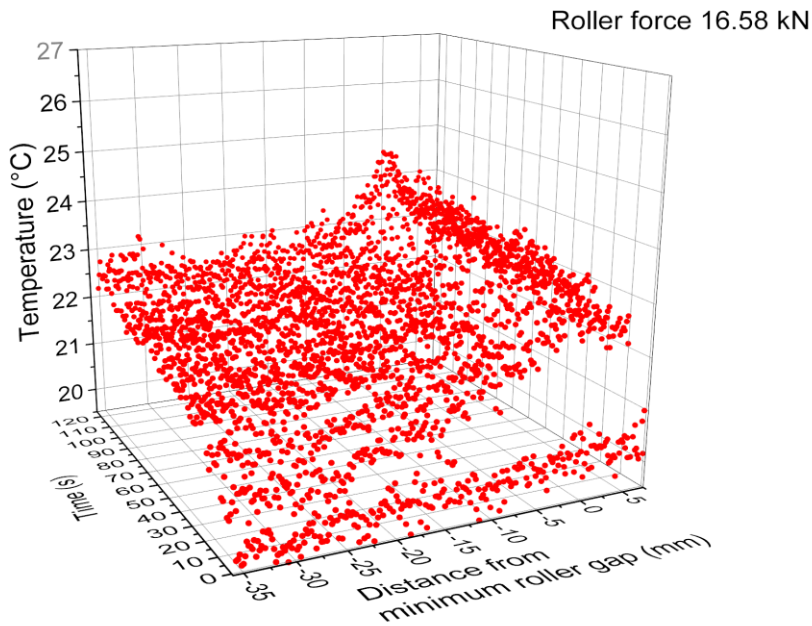

Figure 7-4. Temperature distribution along the feeding direction with time under the roller force of 16.58 kN.

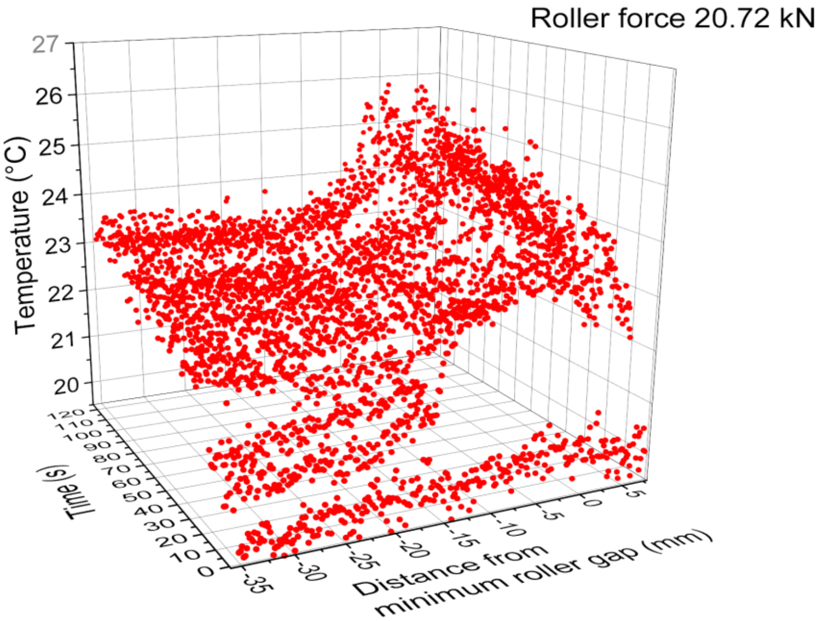

Figure 7-5. Temperature distribution along the feeding direction under the roller force of 20.72 kN.

Figure 7-4 and Figure 7-5 illustrates that the maximum temperature of compacted powder (ribbon) keeps at about 24.5°C and 26°C respectively, under the roller force of 16.58 kN and 20.72 kN. Figure 7-4 and Figure 7-5 indicate that the higher roller force applied, the higher difference of powder temperature between the feeding zone and compaction zone. Moreover, under the roller force of 16.58 kN and 20.72 kN, the screw speed is adjusted to 40 rpm and 43 rpm, which causes the increase of powder temperature in the feeding zone compared with that under the lower roller force.

Comparison of temperature distribution along feeding direction and across the ribbon width

Figure 7-6 shows the powder temperature distribution along the feeding direction and across the ribbon width at the end of 2 minutes (same as the 120 s in Figure 7-2 to Figure 7-5). Along the feeding direction, powders experience the increasing stress from the rollers, which causes an increasing temperature until the minimum roller gap. Then, the temperature of ribbons (compacted powder) deceases as they exit from the roller gap. It is worth to note that the temperature measured across the ribbon width is not the temperature in the compaction zone. In other words, the temperature in the compaction zone is higher than the ribbons (compacted powder) exit from the roller gap, as shown in Figure 7-6.

Figure 7-6 illustrates that as the roller force increases, the temperature of powder increases. As for the powder temperature distribution across the ribbon width, there is a higher temperature at the ribbon centre and lower temperature at the ribbon side, due to more powder fed towards the roller centre than roller sides.

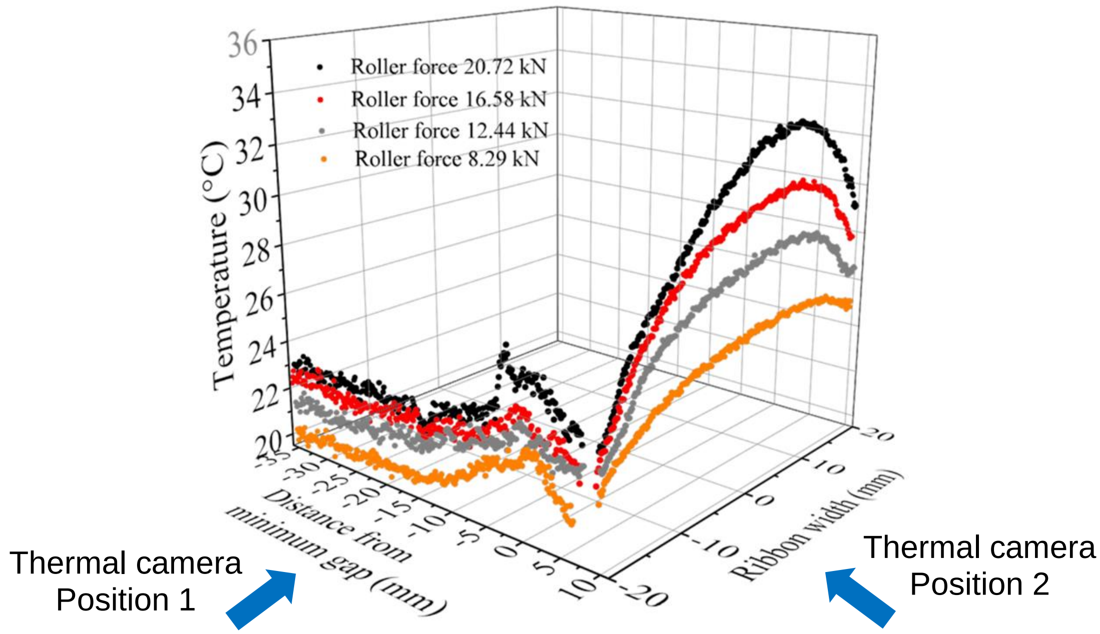

Figure 7-6. The temperature distribution along the feeding direction and across the ribbon width at 2 minutes.

7.3.1.2 Density distribution along the feeding direction

Figure 7-7 (a) shows the X-ray image of compacted powder along feeding to compaction direction. Along feeding to compaction zone, powders have been gradually densified by the increasing stress applied from the rollers. As powders are approaching the narrow roller gap, the compacted powder body become denser comparing to the location away from the narrow roller gap. It is clear to see that the amount of voids decreases along feeding to compaction direction, as displayed in Figure 7-7 (a). The density calculation and calibration of compacted powder by the X-ray are mentioned with details in Chapter 3.2.3.2. Figure 7-7 (b) is showing the top view (an optical image using a microscope) of the compacted powder along feeding to compaction direction. As powders approach the compaction zone (close to the narrow roller gap), higher stress from rollers contributes to a more prominent “diamond” pattern (same as roller surface pattern) on both surface of compacted powder as shown in Figure 7-7 (b), which is also presented in Figure 7-7 (a). Furthermore, Figure 7-7 (a) demonstrates that the parts of compacted powder close to the feeding zone are with more voids and more fragile (weak strength), which are shown as the broken corner on the top and bottom left side of the compacted body in Figure 7-7 (b).

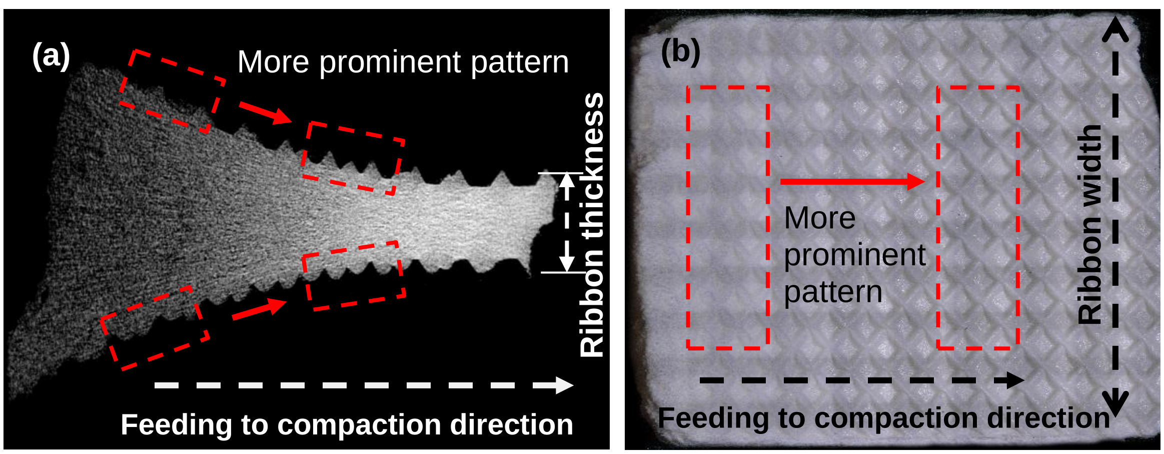

Figure 7-7. The X-ray scan image (a) and optical image (b) of compacted powder (MCC) as the roller speed at 3 rpm, 20.72 kN of roller force, 2 mm of roller gap.

The density of the compacted powder is carried out using Eq (21) with the porosity determined from X-ray scanning results. In order to investigate the effect of roller forces on the density distribution (along the feeding direction and across the ribbon width), the density distribution is plotted in contour graphs with colour ranges as shown in Figure 7-8. In the contour graphs, the value of density is converted into colour levels, where dark blue means low density and bright red indicates high density).

Figure 7-8 shows that the density distributions of compacted powder (along the feeding direction and across the ribbon width) with different roller forces. For example, the density of the compacted powder increases along the feeding direction until the minimum roller gap at 0 mm on the vertical axis. Meanwhile, the density of the compacted powder is higher around the ribbon centre than that at the sides of the ribbon. When the ribbon (compacted powder) exit from the minimum gap, it will expand with the increase of the volume, which causes a decrease of the density on the horizontal minus axis as displayed in Figure 7-8.

Figure 7-8 also illustrates that higher density (presented as red colour) indicates more powders fed between the roller centre in the roller compaction process. For instance, as the roller force increases from 8.29 kN to 20.72 kN, the density of the ribbon centre and ribbon side increases due to the more stress applied to the powder. Comparing to Figure 7-8 (a), Figure 7-8 (b) illustrates that, at 0 mm on the horizontal axis, the density across the ribbon width increases. Moreover, compared with Figure 7-8 (a), more areas of red colour are presenting the higher density in Figure 7-8 (b), (c) and (d). Comparing Figure 7-8 (c) and (d) to Figure 7-8 (a) and (b), as a higher roller force is applied, the density increases along the feeding direction and across the ribbon width.

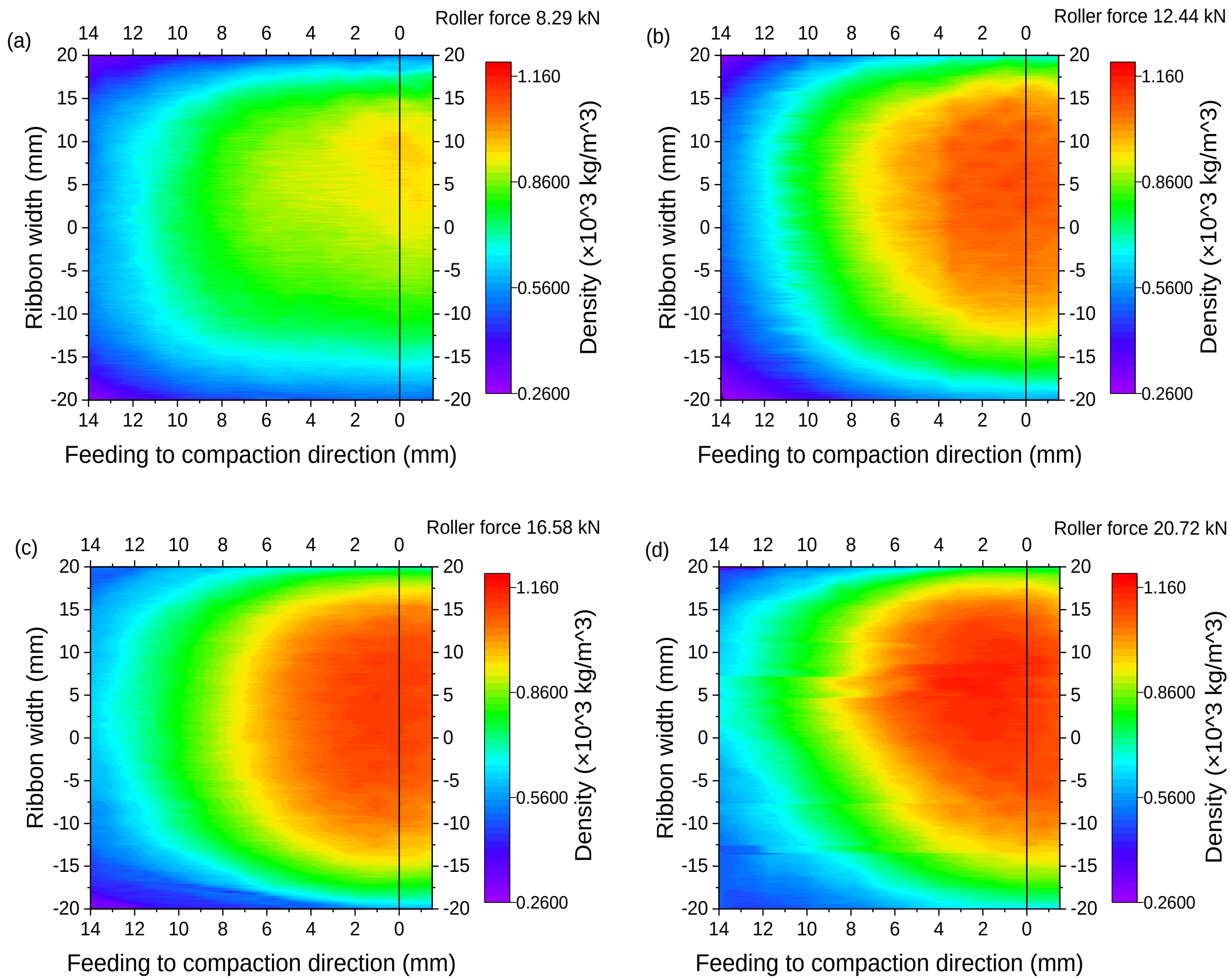

Figure 7-8. The density distribution profiles of compacted powder as the roller speed at 3 rpm, 2 mm of roller gap.

7.3.1.3 Comparisons of temperature profiles and density profiles along the feeding direction

Figure 7-9 shows the temperature profiles and density distribution profiles along the feeding to the compaction zone (including after the exit of minimum roller gap).

Three density profiles are plotted in Figure 7-9: “Centre” shows the maximum density profile, which is close to the centreline of the compacted body; “Side 1” shows the density profile, which is at the inner side of the side-sealing cheek plate (close to machine frame); “Side 2” shows the density profile which is at the side of modified design cheek plate (away from the machine frame). In Figure 7-9, comparing “Centre” profile to “Side 1” and “Side 2” profiles, there is approximate 0.2 to 0.4×10^3 kg/m^3 difference in density along the feeding direction under the roller force of 8.29 kN.

Figure 7-9 shows that the temperature and density distribution correspond to the angular positions. For instance, the angular position of 0° is the minimum roller gap. The significant difference in powder temperature starts at the angular position of 15°; it gradually increases to the maximum temperature until the 0° angular position, then it decreases where ribbons exit from the roll gap. The extended three density profiles reach a joint point at around angular position of 15°. The nip angle from Johanson theory is calculated as 22.3° and plotted as a solid black line, as shown in Figure 7-9. The Johanson theory was proposed with the statement of over-predicted nip angle (Al-Asady et al., 2016; Muliadi et al., 2012), which agrees with the trend shown in Figure 7-9.

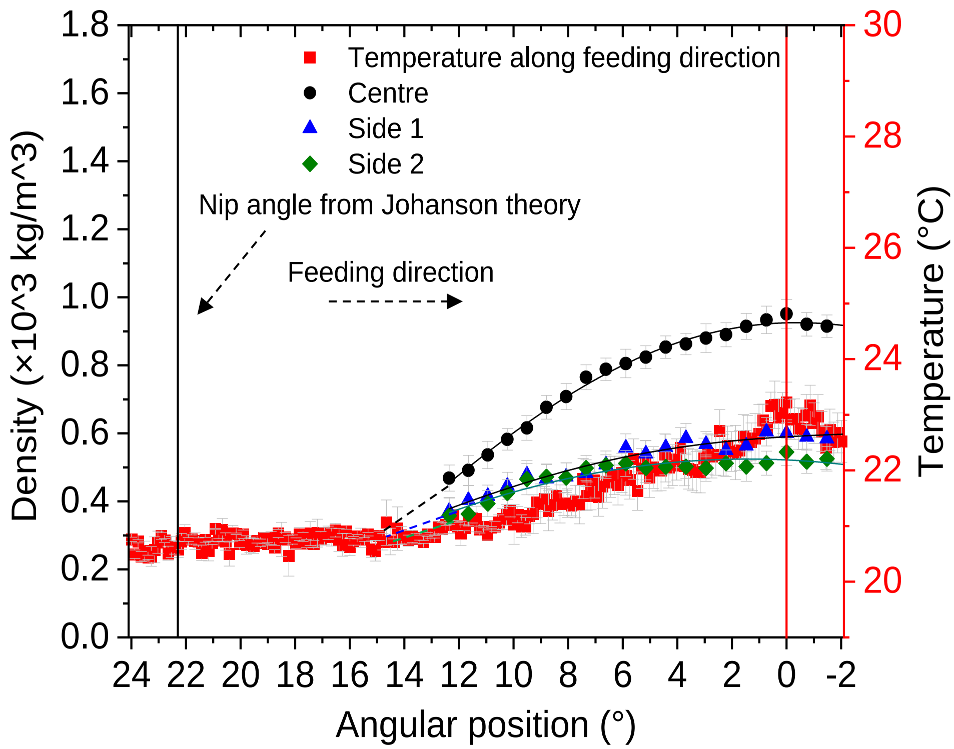

Figure 7-9. Nip angle, temperature and density distribution along feeding to compaction direction at the roller force of 8.29 kN.

In Figure 7-10, the density difference along the feeding direction for the "Centre" is around 0.6×10^3 kg/m^3 under the roller force of 12.44 kN. Comparing to the "Centre", less powders are compacted at sides between the rollers, which results in a lower density. There are 0.4 and 0.35×10^3 kg/m^3 of the density differences along the feeding direction for the "Side 1" and "Side 2", respectively, which is showing a clear similar trend as the profile of "Centre". The extended three density profiles reach a joint point at around angular position of 15°, which agrees with the angular position where the temperature starts to increase with a difference gradually.

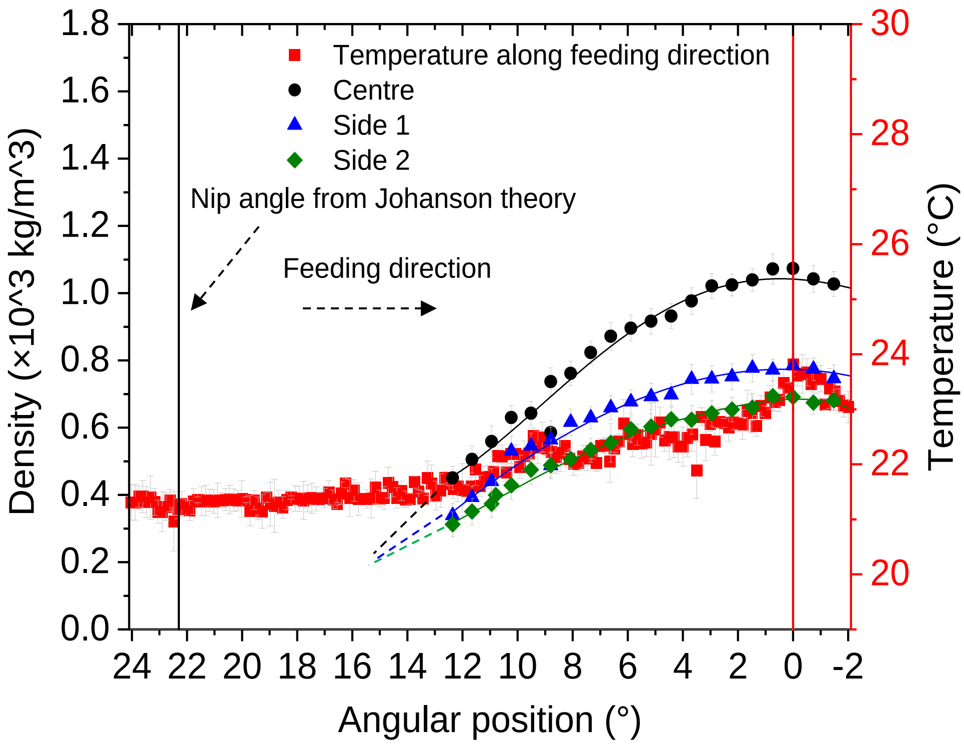

Figure 7-10. Nip angle, temperature and density distribution along feeding to compaction direction at the roller force of 12.44 kN.

As powders are fed (after screw feeder) towards the rollers, the powders are compacted in a limited extent in this region where the powder temperature keeps steady. The stress increases significantly as powders approach the narrow roller gap, the temperature and density of compacted powder increase. As a result of the rotating screw feeder, it is pushing powders towards one side, which is the inner side of the side-sealing cheek plate, reported by Mazor et al. (2018). More powders are fed to the side of inner side-sealing cheek plate. It agrees with that the density values of "Side 1" are higher than that of "Side 2" as shown in Figure 7-10.

Figure 7-11 shows that the powder temperature and density increase along the feeding direction under the roller force of 16.58 kN. The densities of “Centre”, “Side 1” and “Side 2” increase gradually from approximate 0.45, 0.35 and 0.35 × 10^3 kg/m^3 until the 0° of angular position with a maximum density of approximate 1.1, 0.8 and 0.7 × 10^3 kg/m^3. Figure 7-11 shows a similar trend that the temperature starts to increase at the angular position of 15° along the feeding direction, where the density profiles extend to joint.

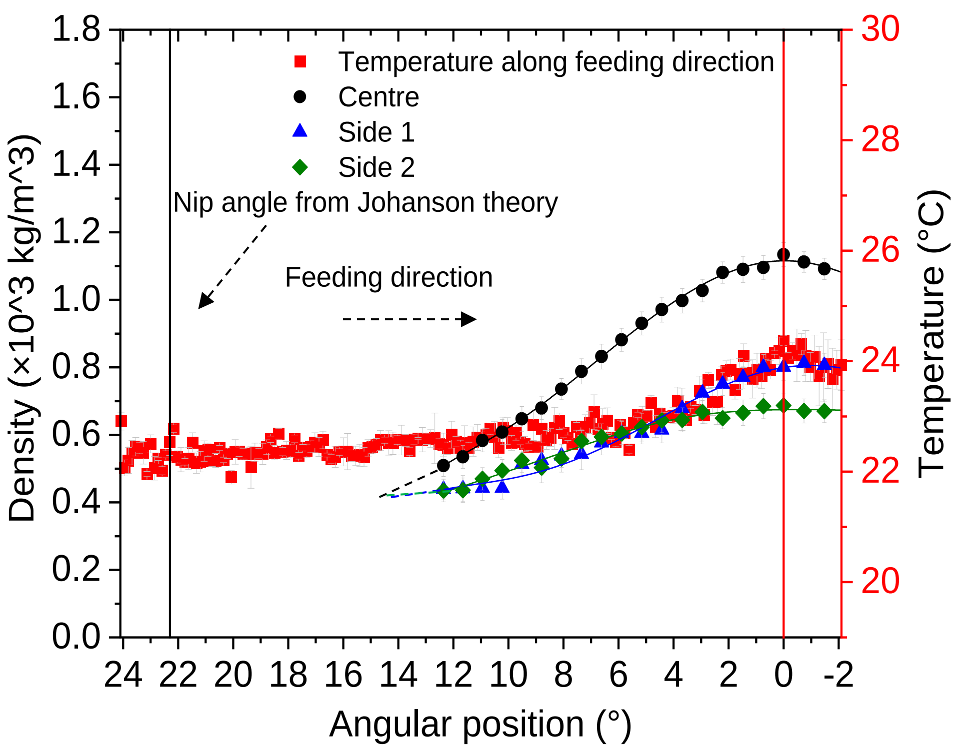

Figure 7-11. Nip angle, temperature and density distribution along feeding to compaction direction at the roller force of 16.58 kN.

Moreover, Figure 7-12 illustrates that when the roller force increases to 20.72 kN, the increase of powder temperature and density are starting from approximately 16.3° of angular position along the feeding direction. The trend of density profiles matches with temperature profile along the feeding direction.

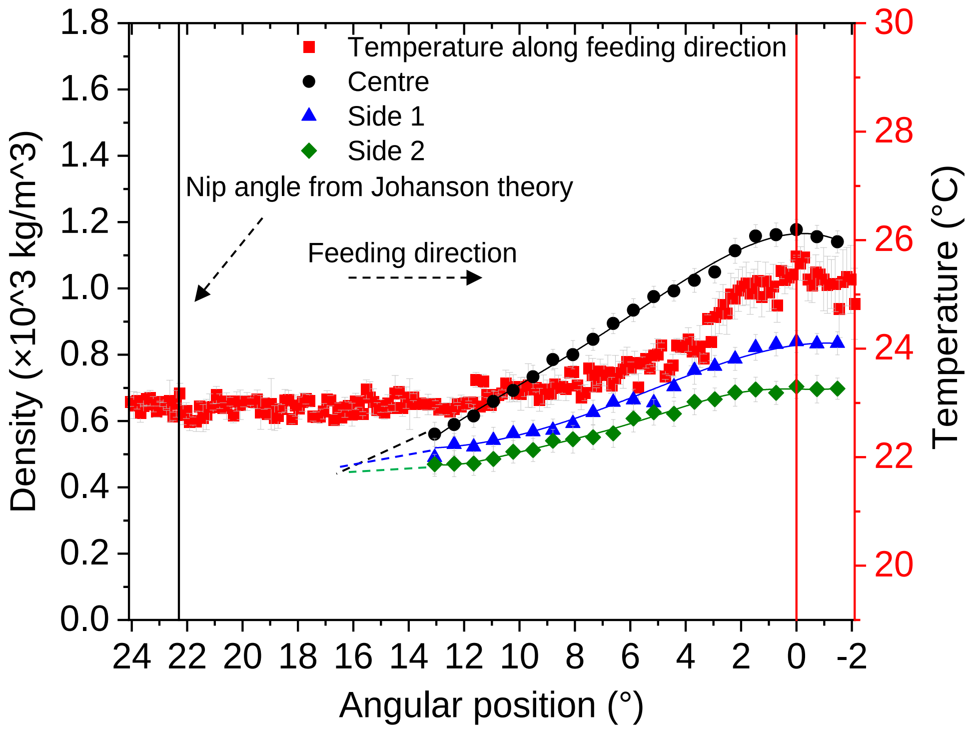

Figure 7-12. Nip angle, temperature and density distribution along feeding to compaction direction at the roller force of 20.72 kN.

Meanwhile, backwards extended three density profiles could be at the joint point around 16.3° of angular position. The trend shows that the nip angle calculated from Johanson theory is over-predicted. Furthermore, the temperature and the density of compacted powder decrease as the angular position is less than 0°.

7.3.2 GLUCIDEX ® Maltodextrin DE6

7.3.2.1 Powder temperature distribution along feeding direction with time

As shown in Figure 7-13, since the time is at 0 s, powders are fed by the screw feeder towards the rollers and the powder temperature keeps at around at 20°C (same as conditioned storage). As powders approach the narrow roller gap, the increase of stress from rollers results in the increasing amount of heat generated, which is showing as the increasing temperature along the feeding to the compaction direction. When the compacted powder (ribbon) leave the minimum roller gap (compaction zone), the temperature starts to decrease.

From 0 s to 40 s, the amount of powder increases to fulfil the roller gap (from 0 mm to 2 mm), in which powder temperature increases at the position between 0 mm to 15 mm on the axis along the feeding direction. After 50 s, the powder temperature starts to be steady. The friction between powders and the screw feeder also causes the heat generated in the feeding zone. At the steady state, there is about 1.5°C difference between the maximum temperature at the minimum roller gap and powder temperature in the feeding zone. Furthermore, the screw speed is quickly adjusted to 23 rpm before steady state due to the higher flowability comparing to MCC, which causes the increase of powder temperature in the feeding zone.

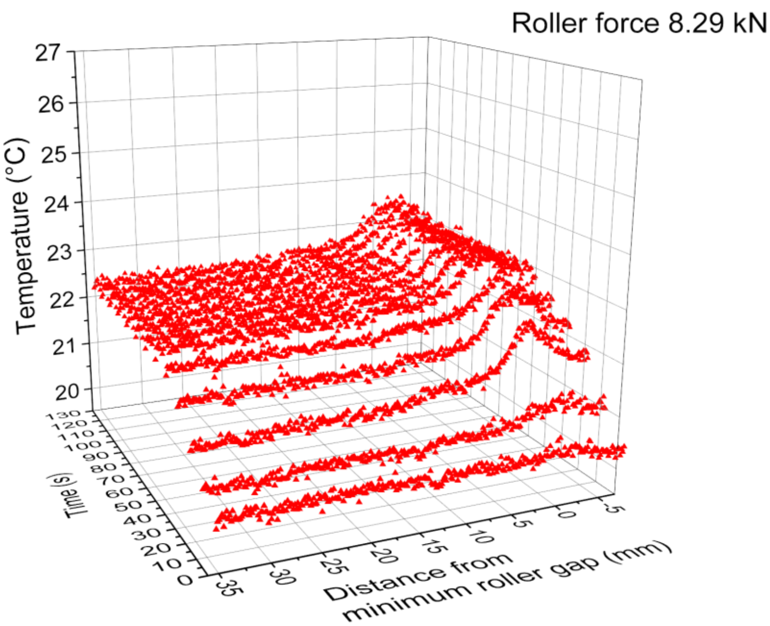

Figure 7-13. Temperature distribution along the feeding direction with time under roller force of 8.29 kN.

Similarly, Figure 7-14, Figure 7-15 and Figure 7-16 illustrate that as time increases from 0 s to 40 s, the temperature increases because of an increasing amount of powder fed to the compaction zone, then temperature becomes steady after 50 s. The temperature difference between the minimum roller gap and the feeding zone increases from about 1.5°C, 2°C to 2.5°C as the roller force increases from 12.44 kN, 16.58 kN to 20.72 kN. Moreover, the increased screw speed before steady state (27 rpm, 30 rpm and 34 rpm respectively under the roller force of 12.44 kN, 16.58 kN and 20.72 kN) causes the increase of powder temperature in the feeding zone.

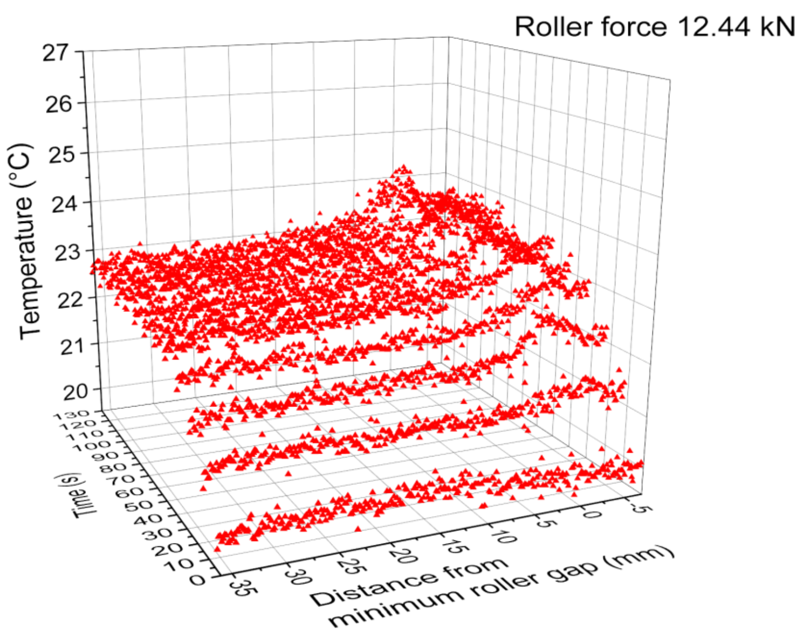

Figure 7-14. Temperature distribution along the feeding direction with time under roller force of 12.44 kN.

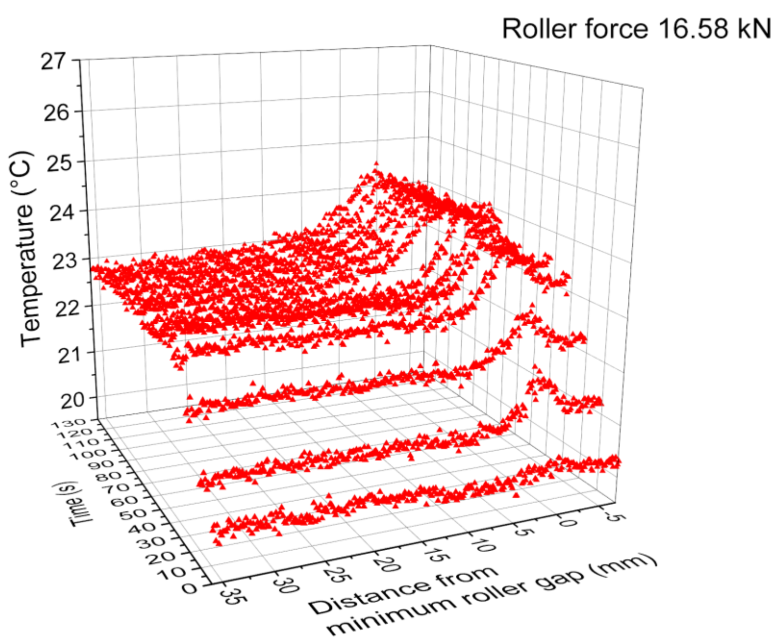

Figure 7-15. Temperature distribution along the feeding direction with time under roller force of 16.58 kN.

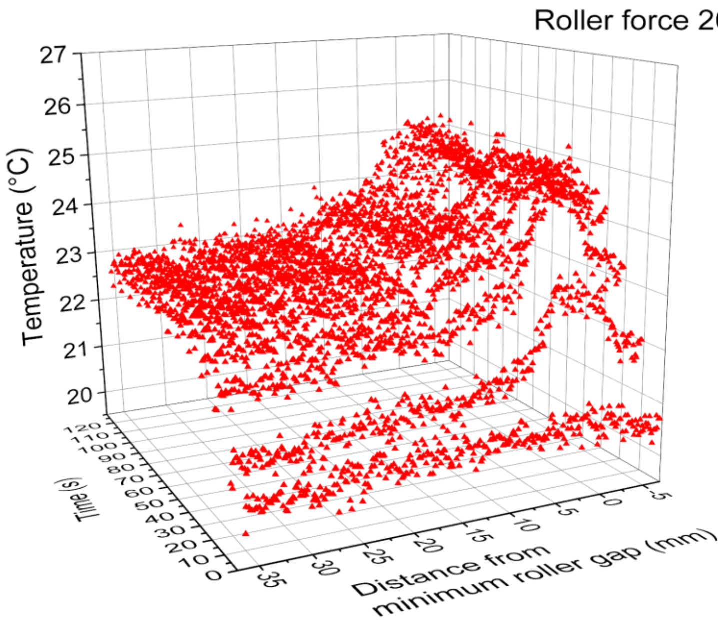

Figure 7-16. Temperature distribution along the feeding direction with time under roller force of 20.72 kN.

Comparison of temperature distribution along feeding direction and across the ribbon width

Figure 7-17 shows the powder temperature distribution along the feeding direction and across the ribbon width at the end of 2 minutes (same as the 120 s in Figure 7-13 to Figure 7-16). Figure 7-17 is showing that there is an increase in temperature difference between the feeding zone and minimum roller gap as the roller force increases. Besides, the increase of roller force results in the increases in temperature across the ribbon width. In addition, the temperature of the compacted powder (ribbon) at the is higher than the temperature of that releases from the minimum roller gap (on the minus axis of the feeding direction).

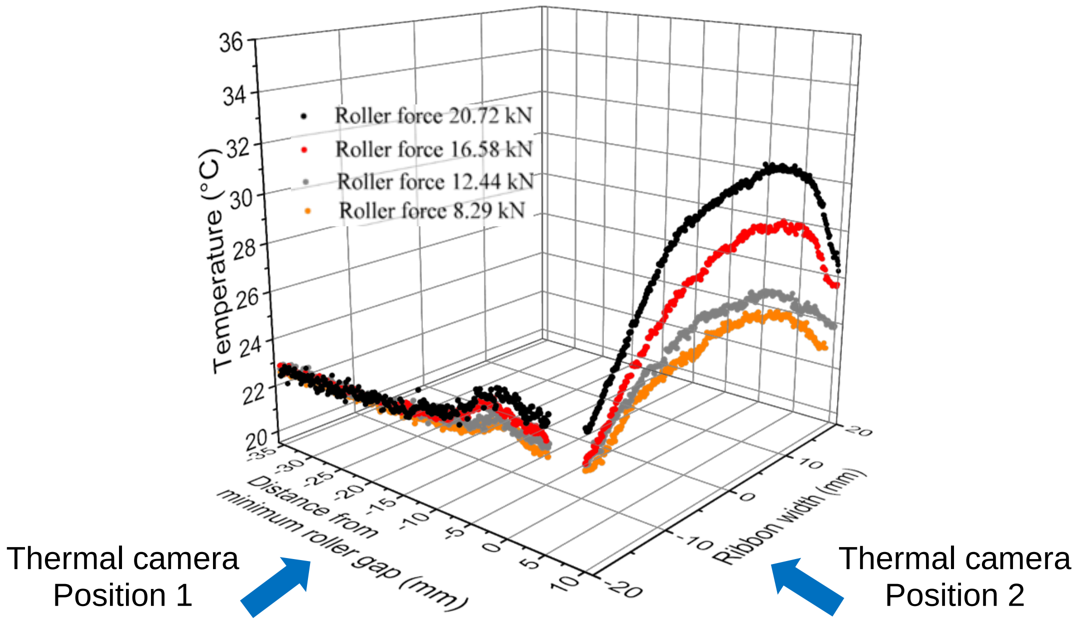

Figure 7-17. The temperature profiles along feeding direction and across ribbon width at 2 minute.

7.3.2.2 Density distribution along feeding to compaction direction

Figure 7-18 illustrates that as the roller force increases, the density of compacted powder increased, which is shown by the colour levels. The lowest density is at the sides of the ribbon. Along feeding to compaction direction, as the powders are fed towards the rollers, the densities gradually increase, which is resulted from the increase of stress from the rollers as shown in Figure 7-18. The trend agrees with that from Figure 7-17, along the feed direction to the compaction zone, the density and temperature gradually increase. A higher density value locates around the ribbon centre than the ribbon sides, because more powders are fed and compacted at the centre than the sides between rollers. In addition, Figure 7-18 shows that the density decreases (presented by lighter colour) when ribbons exit from minimum roller gap, which is shown on the axis position from 0 to -1 mm along the feeding to compaction direction.

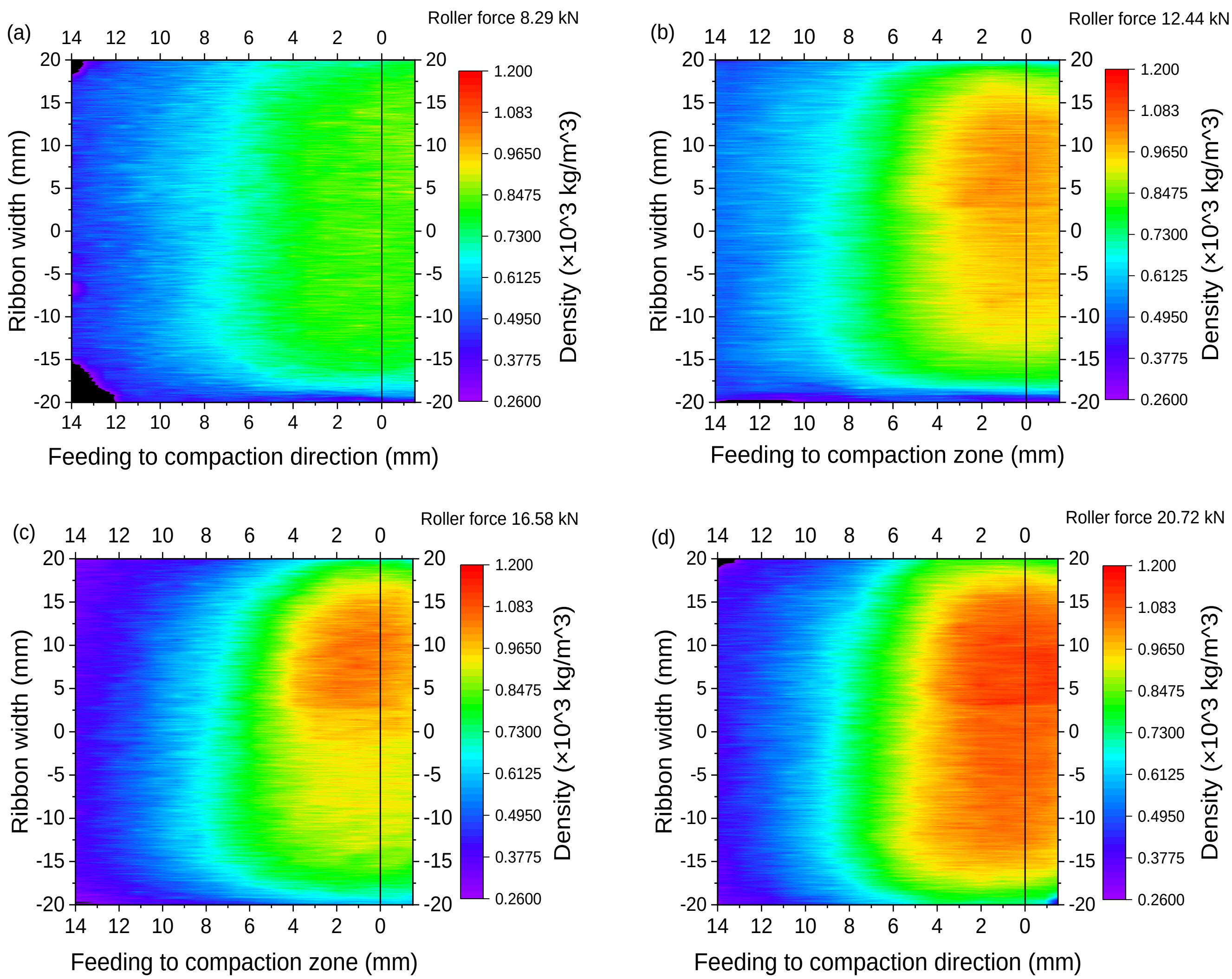

Figure 7-18. The density distribution profiles of compacted powder as the roller speed at 3 rpm, 2 mm of roller gap.

7.3.2.3 Comparisons of temperature profiles and density profiles along the feeding direction

The temperature distribution and the density distribution are compared along the feeding to compaction direction, as illustrated in Figure 7-19 to Figure 7-22 under different roller forces. For instance, Figure 7-19 shows the differences between the three density profiles under the roller force of 8.29 kN. The density of “Side 1” (close to the machine frame) is higher than that of “Side 2” (close to the modified cheek plate). The density of “Centre” is higher than the density of “Side 1” and “Side 2”. The difference in density between “Centre” and “Side 1”, “Side 2" increases from the similar value at the angular position of 14.5°, to 0.15 and 0.2 × 10^3 kg/m^3 respectively at the angular position of - 2°.

Furthermore, Figure 7-19 shows the temperature starts to increase at the angular position of around 14.5°. The joint point of density profiles (“Centre”, “Side 1” and “Side 2") could be explained as a similar value of density at the angular position of around 14.5°. The joint point of density profiles and the start point of the increasing temperature are potential to be the approximate initial point of the increase of stress from rollers (start of nip region). However, the nip angle calculated from Johanson theory is compared and showing an overpredicted value, as shown in Figure 7-19, which is also confirmed in the literature (Muliadi et al., 2012).

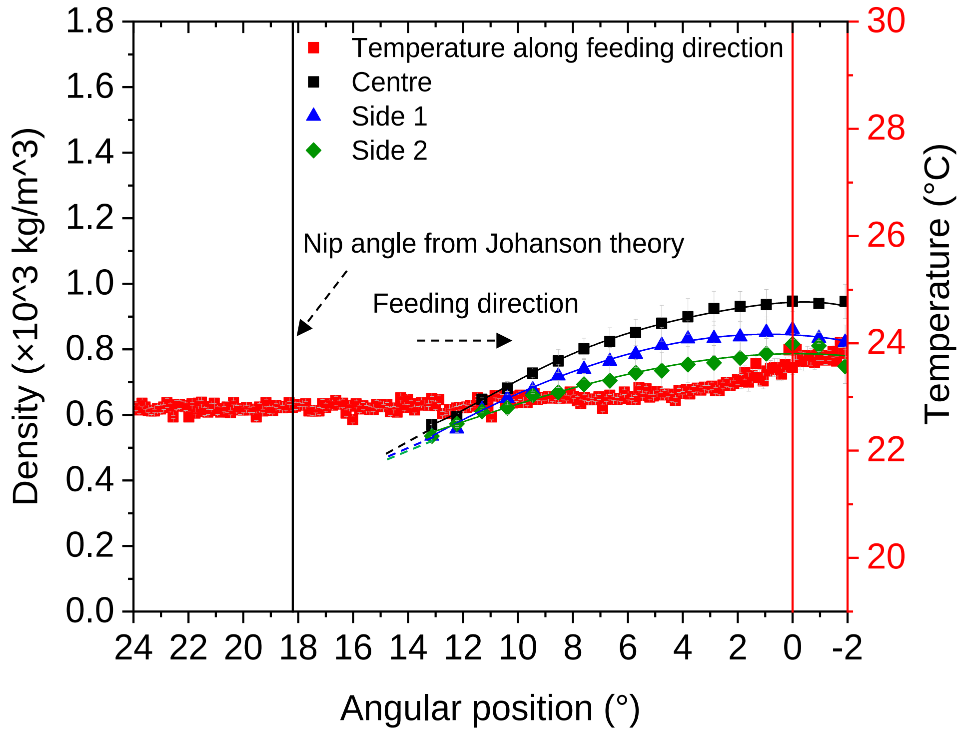

Figure 7-19. Nip angle, temperature profiles and density distribution along feeding to compaction direction under the roller force of 8.29 kN.

Figure 7-20 demonstrates the comparison of temperature and density distribution along the feeding to compaction direction under the roller force of 12.44 kN. As the roller force increases, the overall density and temperature increase along the feeding direction. The temperature and density increase from a similar angular position of around 15°. It could explain that the stress from rollers starts to increase at this angular position. However, the value calculated from the Johanson theory nip angle is 18.3°, which is showing as overpredicted. Moreover, at the angular position of 18.3°, the temperature of powder is still similar to that after the end of the screw feeder (at the angular position of 24°).

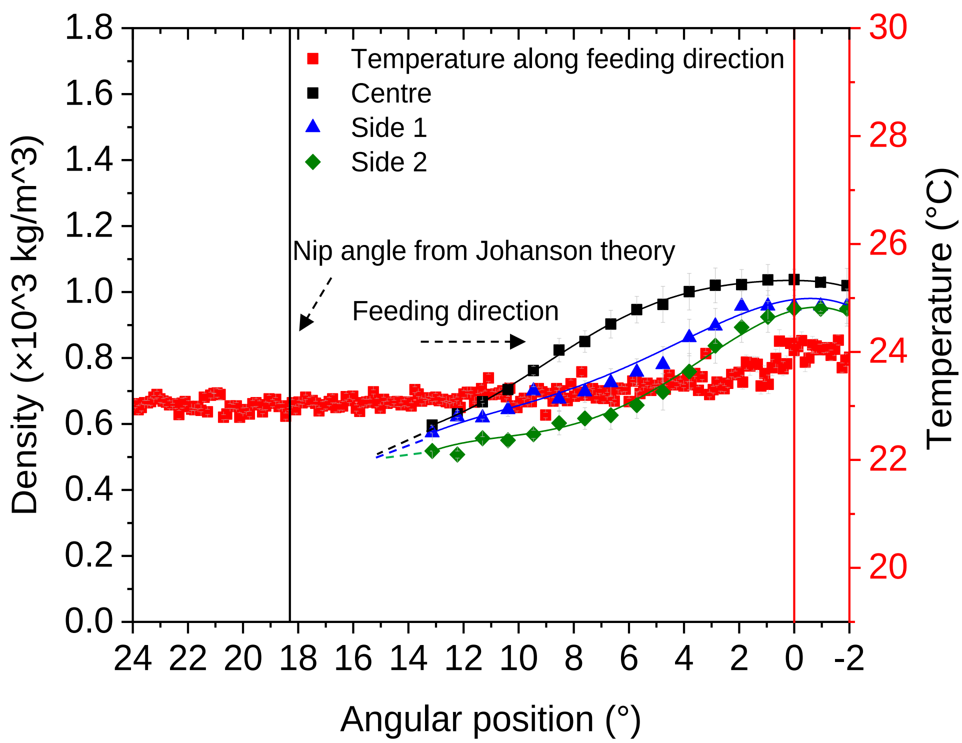

Figure 7-20. Nip angle, temperature profiles and density distribution along feeding to compaction direction as the roller speed at the roller force of 12.44 kN.

Figure 7-21 shows that the temperature and density distribution under the roller force of 16.58 kN. The density distribution profiles display a progressive increase along the feeding direction until the angular position of 0°. The temperature distribution profile indicates a start of increasing temperature at the angular position of 15°. Meanwhile, there could be expected a joint point of density distribution profiles at the angular position of 15°.

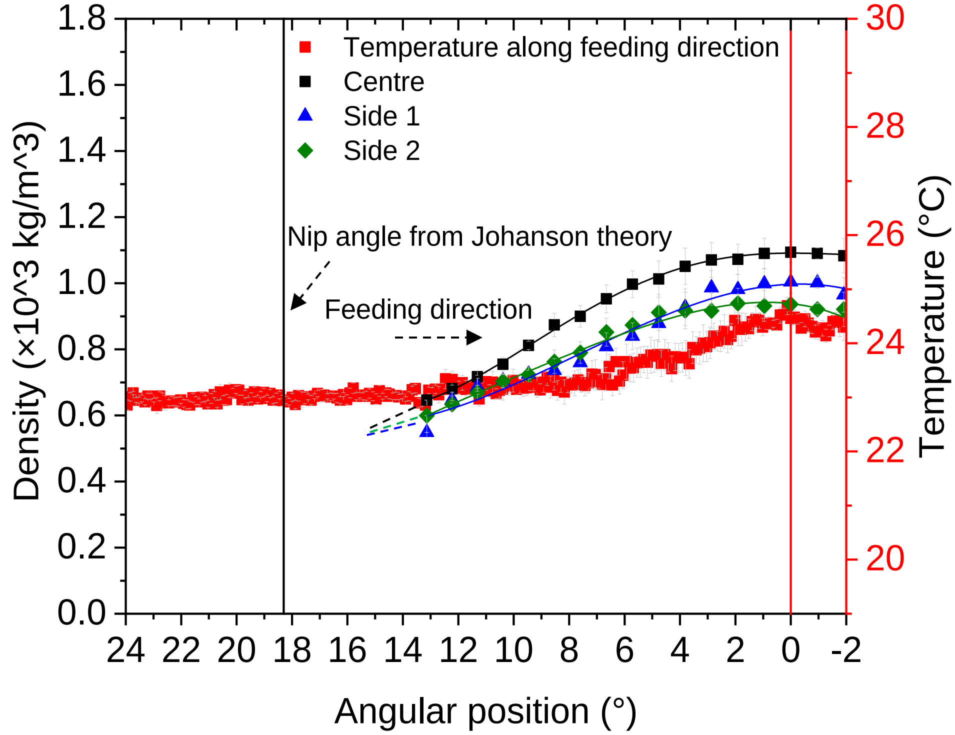

Figure 7-21. Nip angle, temperature profiles and density distribution along feeding to compaction direction as the roller speed at the roller force of 16.58 kN.

Figure 7-22 illustrates the results of comparing temperature and density distribution along the feeding direction under the roller force of 20.72 kN. The density profiles show the same increasing trend along the feeding direction, as the powders experience the increasing stress from the rollers. Also, the temperature distribution profile shows the increase of temperature starts at around angular position of 16°, in which it could be expected a joint point of the density profiles. The angular position of 16° is assumed to be the start point of the nip region, which is showing a lower value of nip angle comparing to that calculated from Johanson theory.

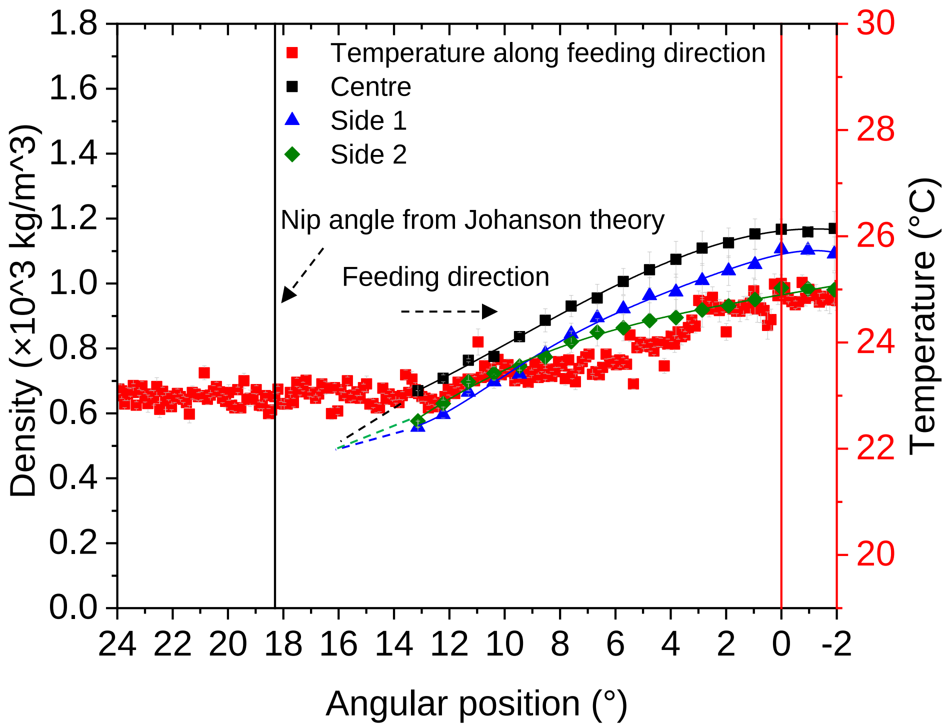

Figure 7-22. Nip angle, temperature profiles and density distribution along feeding to compaction direction as the roller speed at the roller force of 20.72 kN.

In summary, as the roller force increases, the nip angle is increasing according to the significant change of the temperature along the feeding direction and the potential joint of density distribution profiles, which was agreed with both MCC and Maltodextrin powder. Furthermore, the examined nip angle of MCC powder is slightly higher than that of the Maltodextrin powder. Meanwhile, the examined nip angle of MCC and Maltodextrin powder is lower than the nip angle calculated from the Johanson theory.

7.4 Conclusions

In this chapter, the temperature of feeding powder and compacted powder (MCC and Maltodextrin) has been monitored by online thermal imaging with the special Germanium window (side-sealing cheek plate) as a PAT. The temperature gradually increases as powder approached closer the narrow roller gap along the feeding to the compaction direction. Besides, the temperature of the ribbon at the minimum gap is higher than the temperature as it releases from the compaction zone. As the roller force increases, the temperature along the feeding direction increases because of higher stress applied to the powder. Additionally, MCC powder is more deformable than Maltodextrin powder, which results in more deformation of MCC powder and higher temperature observed under the same roller force.

Meanwhile, the density distribution of compacted powder has been examined, which matched the trend of temperature profiles along feeding direction and across ribbon width. The density increases along feeding direction as powders approach the minimum roller gap and decrease as it releases; higher density locates at the ribbon centre than the ribbon sides.

Moreover, the nip region was investigated from the results of temperature and density along the feeding to the compaction direction under different roller forces. The examined nip angle (nip region) was less than that calculated from the Johanson theory, which can be explained that Johanson theory overpredicted actual mass of powder fed to the compaction zone (Muliadi et al., 2012).

Chapter 8 Conclusions and future work

8.1 Conclusions

In this research, the behaviour of the powder in the feeding system of the roller compaction process has been investigated. The powder flowability in this process has a significant effect on the behaviour of the powder in the compaction zone, and therefore on the final product properties. This study focused on designing new parts in the roller compactor in order to improve the powder feeding in the process, which ultimately improved the uniformity of temperature and porosity across the ribbon width.

In the first attempt, the flow of different powders was investigated at different relative humidity conditions using newly designed setups to mimic the roller compaction feeding process. The first setup, which involved an array design of straws, was used to deliver a uniform powder feeding to its destination. However, this design was not useful for cohesive and poor flowability powders. To overcome this issue, the second setup was designed, which involved passing the powder through a guiding setup with varying flight angle, which controls the amount of powder fed at different positions. The optimum angle of the flights in the guiding setup was found to be lower with the increase of repose angle of the powder. Both designs were found to be useful in improving the powder distribution by controlling the flow of powder at the side and the centre of the passage.

Based on the idea from the first attempt, a design of feeding guiders was implemented in a lab-scale roller compactor (Alexanderwerk WP120) to improve the uniformity of powder distribution to the compaction zone. The feeding guiders were designed with a range of dimension grades (height) under the considerations of the powder flowability and process parameters involved in the design of experiments. The ribbon temperature was online monitored using a thermal camera and the temperature distribution across the width of the ribbon was used as an indication of improving the powder feeding uniformity. The results showed that the uniformity of temperature across the ribbon of all powders was improved significantly when using the feeding guiders at different roller forces. The overall relative temperature uniformity increased for feeding guiders, which was significantly higher than that of the original guiders. The feeding guiders were also scaled up and used in a pilot plant scale roller compactor (Alexanderwerk WP200 Pharma). The feeding guiders showed significant improvements in the product quality, which was indicated by the ribbon temperature and porosity distribution across its width.

A design space graph has been then developed and used as a conclusion for materials with different flowabilities, dimension grades of feeding guiders and roller forces, which can be used for the design of experiments and prediction of relative temperature uniformity of other materials.

The online system for monitoring temperature was then implemented to examine the powder temperature in feeding and compaction zone during the roller compaction. This was facilitated with thermal imaging as a PAT and modified side-sealing cheek plate (fixed with Germanium windows). The temperature of the powder was found to increase gradually while approaching the narrow roller gap along the feeding to the compaction direction. In addition, the temperature of compacted powder at the minimum gap was higher than the temperature as it exits from the compaction zone. As the roller force increases, the temperature along the feeding direction increased because of higher stress applied to the powder. The density distribution of compacted powder (investigated using an X-ray tomography) was found to match the temperature profiles along feeding direction and across ribbon width. The density increases as powder approach the minimum roller gap and decrease as it exits, and higher density at the ribbon centre and lower at the ribbon sides.

8.2 Future work

8.2.1 Improving powder distribution in the roller compaction

In the future work, a regime map (based on the design space graph) will be developed for optimum relative uniformity of product properties, which is based on the powder flowability and mechanical properties of powders (particle hardness or powder compressibility), dimension grade of feeding guiders and process parameters of roller compaction such as roller speed, roller force and roller gap. The regime map can help industries easily find a matched feeding guider to achieve the optimum uniformity of ribbon temperature and porosity across the width and reduction in the amount of fines using the feeding guiders referring to the materials’ properties and process parameters used in the process. This can help avoid wasting a good amount of materials and time.

8.2.2 Online thermal imaging of powder temperature from feeding to compaction zone in roller compaction

In the future, online thermal imaging (as a Process Analytical Technology - PAT) can be used to examine the relationship between the temperature and density distribution along the feeding to the compaction direction. The work can involve more process parameters, such as roller speed, roller force and roller gap, in order to investigate the relationship between the temperature and the density. Those results could be further understanding the nip region and comparing with the value calculated from Johanson theory in a wide range of process parameters and different materials' properties. Moreover, the strength of the Germanium window (used in the modified cheek plate) needs to be tested before the roller compaction process operates at a higher roller force and roller gap.

References

AL-ASADY, R. B., DHENGE, R. M., HOUNSLOW, M. J. & SALMAN, A. D. 2016. Roller compactor: Determining the nip angle and powder compaction progress by indentation of the pre-compacted body. *Powder Technology,* 300**,** 107-119.

AL-ASADY, R. B., OSBORNE, J. D., HOUNSLOW, M. J. & SALMAN, A. D. 2015. Roller compactor: The effect of mechanical properties of primary particles. *International Journal of Pharmaceutics,* 496**,** 124-36.

ALLESO, M., HOLM, R. & HOLM, P. 2016. Roller compaction scale-up using roll width as scale factor and laser-based determined ribbon porosity as critical material attribute. *European Journal of Pharmaceutical Sciences,* 87**,** 69-78.

BACHER, C., OLSEN, P. M., BERTELSEN, P., KRISTENSEN, J. & SONNERGAARD, J. M. 2007. Improving the compaction properties of roller compacted calcium carbonate. *International Journal of Pharmaceutics,* 342**,** 115-23.

BI, M., ALVAREZ-NUNEZ, F. & ALVAREZ, F. 2014. Evaluating and modifying Johanson's rolling model to improve its predictability. *Journal of Pharmaceutical Sciences,* 103**,** 2062-2071.

BINDHUMADHAVAN, G., SEVILLE, J. P. K., ADAMS, M. J., GREENWOOD, R. W. & FITZPATRICK, S. 2005. Roll compaction of a pharmaceutical excipient:

Experimental validation of rolling theory for granular solids. *Chemical Engineering Science,* 60**,** 3891-3897.

BROWNSON, J. R. S. 2014. *Solar Energy Conversion Systems,* Boston, Academic Press.

CAPECE, M., SILVA, K. R., SUNKARA, D., STRONG, J. & GAO, P. 2016. On the relationship of inter-particle cohesiveness and bulk powder behavior: Flowability of pharmaceutical powders. *International Journal of Pharmaceutics,* 511**,** 178-89.

COELHO, M. C. & HARNBY, N. 1978. The effect of humidity on the form of water retention in a powder. *Powder Technology,* 20**,** 197-200.

CUNNINGHAM, J. C., WINSTEAD, D. & ZAVALIANGOS, A. 2010. Understanding variation in roller compaction through finite element-based process modeling. *Computers & Chemical Engineering,* 34**,** 1058-1071.

DEC, R. T., ZAVALIANGOS, A. & CUNNINGHAM, J. C. 2003. Comparison of various modeling methods for analysis of powder compaction in roller press. *Powder Technology,* 130**,** 265-271.

EMERY, E., OLIVER, J., PUGSLEY, T., SHARMA, J. & ZHOU, J. 2009. Flowability of moist pharmaceutical powders. *Powder Technology,* 189**,** 409-415.

FITZPATRICK, J. J., BARRINGER, S. A. & IQBAL, T. 2004. Flow property measurement of food powders and sensitivity of Jenike's hopper design methodology to the measured values. *Journal of Food Engineering,* 61**,** 399-405.

FOROUGHI-DAHR, M., SOTUDEH-GHAREBAGH, R. & MOSTOUFI, N. 2019. Effect of operation conditions on coating of pharmaceutical pellets with a film of HPMC/PEG in a Wurster coater. *Powder Technology,* 354**,** 804-814.

FREEMAN, R. 2007. Measuring the flow properties of consolidated, conditioned and aerated powders — A comparative study using a powder rheometer and a rotational shear cell. *Powder Technology,* 174**,** 25-33.

FUNAKOSHI, Y., ASOGAWA, T. & SATAKE, E. 1977. The use of a Novel Roller Compactor with a Concavo-Convex Roller pair to Obtain Uniform Compacting Pressure. *Drug Development and Industrial Pharmacy,* 3**,** 555-573.

GERDEEN, J. C. & RORRER, R. A. L. 2011. *Engineering Design with Polymers and Composites,* New York, CRC Press.

GUIGON, P. & SIMON, O. 2003. Roll press design—influence of force feed systems on compaction. *Powder Technology,* 130**,** 41-48.

HORIO, T., YASUDA, M. & MATSUSAKA, S. 2014. Effect of particle shape on powder flowability of microcrystalline cellulose as determined using the vibration shear tube method. *International Journal of Pharmaceutics,* 473**,** 572-8.

HULL, P. 2010. *Glucose Syrups: Technology and Applications,* Chicester, Wiley-Blackwell.

INGHELBRECHT, S. & REMON, J. P. 1998. Roller compaction and tableting of microcrystalline cellulose drug mixtures. *International Journal of Pharmaceutics,* 161**,** 215-224.

JAGER, P. D., BRAMANTE, T. & LUNER, P. E. 2015. Assessment of Pharmaceutical Powder Flowability using Shear Cell-Based Methods and Application of Jenike's Methodology. *Journal of Pharmaceutical Sciences,* 104**,** 3804-13.

JENIKE, A. W. & SHIELD., R. T. 1959. On the plastic flow of Coulomb Solids beyond original failure. *Journal of Applied Mechanics,* 26**,** 599-602.

JOHANSON, J. R. 1965. A rolling theory for granular solids, ASME Journal of Applied Mechanics. *Journal of Applied Mechanics,* 32**,** 842-848.

KAERGER, J. S., EDGE, S. & PRICE, R. 2004. Influence of particle size and shape on flowability and compactibility of binary mixtures of paracetamol and microcrystalline cellulose. *European Journal of Pharmaceutical Sciences,* 22**,** 173-9.

KATASHINSKII, V. P. 1966. Analytical determination of specific pressure during the rolling of metal powders. *Powder Metallurgy and Metal Creamics,* 5**,** 765-772.

KHOMANE, K. S. & BANSAL, A. K. 2014. Differential compaction behaviour of roller compacted granules of clopidogrel bisulphate polymorphs. *International Journal of Pharmaceutics,* 472**,** 288-95.

KLEINEBUDDE, P. 2004. Roll compaction/dry granulation: pharmaceutical applications. *European Journal of Pharmaceutics and Biopharmaceutics,* 58**,** 317-26.

KROK, A., PECIAR, M. & FEKETE, R. 2014. Using the DPIV optical technique to measure the velocity of powder material in the space between the rollers in a roll compactor. *Powder Technology,* 262**,** 131-141.

KROK, A. & WU, C. Y. 2019. Evolutions of temperature and density during roll compaction of a pharmaceutical excipient. *International Journal of Pharmaceutics,* 572**,** In Press.

KUHN, H. A. & DOWNEY, C. L. 1971. Deformation characteristics and plasticity theory of sintered powder materials. *International Journal of Powder Metallurgy,* 7**,** 15-25.

LETURIA, M., BENALI, M., LAGARDE, S., RONGA, I. & SALEH, K. 2014. Characterization of flow properties of cohesive powders: A comparative study of traditional and new testing methods. *Powder Technology,* 253**,** 406-423.

LITSTER, J. & ENNIS, B. 2004. *The Science and Engineering of Granulation Processes,* Dordrecht, Kluwer Academic Publishers.

LIU, L. X., MARZIANO, I., BENTHAM, A. C., LITSTER, J. D., WHITE, E. T. & HOWES, T. 2008. Effect of particle properties on the flowability of ibuprofen powders. *International Journal of Pharmaceutics,* 362**,** 109-17.

LUMAY, G., TRAINA, K., BOSCHINI, F., DELAVAL, V., RESCAGLIO, A., CLOOTS, R. & VANDEWALLE, N. 2016. Effect of relative air humidity on the flowability of lactose powders. *Journal of Drug Delivery Science and Technology,* 35**,** 207-212.

MAZOR, A., OREFICE, L., MICHRAFY, A., DE RYCK, A. & KHINAST, J. G. 2018. A combined DEM & FEM approach for modelling roll compaction process. *Powder Technology,* 337**,** 3-16.

MAZOR, A., PEREZ-GANDARILLAS, L., DE RYCK, A. & MICHRAFY, A. 2016. Effect of roll compactor sealing system designs: A finite element analysis. *Powder Technology,* 289**,** 21-30.

MCAULIFFE, M. A. P., O'MAHONY, G. E., BLACKSHIELDS, C. A., COLLINS, J. A., EGAN, D. P., KIERNAN, L., O'NEILL, E., LENIHAN, S., WALKER, G. M. & CREAN, A. M. 2014. The Use of PAT and Off-line Methods for Monitoring of Roller Compacted Ribbon and Granule Properties with a View to

Continuous Processing. *Organic Process Research & Development,* 19**,** 158-166.

MICHRAFY, A., DIARRA, H., DODDS, J. A. & MICHRAFY, M. 2011a. Experimental and numerical analyses of homogeneity over strip width in roll compaction. *Powder Technology,* 206**,** 154-160.

MICHRAFY, A., DIARRA, H., DODDS, J. A., MICHRAFY, M. & PENAZZI, L. 2011b. Analysis of strain stress state in roller compaction process. *Powder Technology,* 208**,** 417-422.

MIGUELEZ-MORAN, A. M., WU, C. Y., DONG, H. & SEVILLE, J. P. 2009. Characterisation of density distributions in roller-compacted ribbons using micro-indentation and X-ray micro-computed tomography. *European Journal of Pharmaceutics and Biopharmaceutics,* 72**,** 173-82.

MIGUELEZ-MORAN, A. M., WU, C. Y. & SEVILLE, J. P. 2008. The effect of lubrication on density distributions of roller compacted ribbons. *International Journal of Pharmaceutics,* 362**,** 52-9.

MULIADI, A. R., LITSTER, J. D. & WASSGREN, C. R. 2012. Modeling the powder roll compaction process: Comparison of 2-D finite element method and the rolling theory for granular solids (Johanson's model). *Powder Technology,* 221**,** 90-100.

MULIADI, A. R., LITSTER, J. D. & WASSGREN, C. R. 2013. Validation of 3-D finite element analysis for predicting the density distribution of roll compacted pharmaceutical powder. *Powder Technology,* 237**,** 386-399.

ODAGI, K., TANAKA, T. & TSUJI, Y. 2001. Compressive Flow Property of Powder in Roll-type Presses Numerical Simulation by Discrete Element Method. *Journal of the Society of Powder Technology, Japan,* 38**,** 150-159.

OMAR, C. S., AL-ASADY, R. B. & SALMAN, A. D. 2019. Roller compaction: Improving the homogeneity of ribbon properties along the roller width. *Powder Technology,* 342**,** 464-474.

OMAR, C. S., DHENGE, R. M., OSBORNE, J. D., ALTHAUS, T. O., PALZER, S., HOUNSLOW, M. J. & SALMAN, A. D. 2015. Roller compaction: Effect of morphology and amorphous content of lactose powder on product quality. *International Journal of Pharmaceutics,* 496**,** 63-74.

OMAR, C. S., DHENGE, R. M., PALZER, S., HOUNSLOW, M. J. & SALMAN, A. D. 2016. Roller compaction: Effect of relative humidity of lactose powder. *European Journal of Pharmaceutics and Biopharmaceutics,* 106**,** 26-37.

OSBORNE, J. D., ALTHAUS, T., FORNY, L., NIEDERREITER, G., PALZER, S., HOUNSLOW, M. J. & SALMAN, A. D. 2013. Investigating the influence of moisture content and pressure on the bonding mechanisms during roller compaction of an amorphous material. *Chemical Engineering Science,* 86**,** 61-69.

PEREZ-GANDARILLAS, L., PEREZ-GAGO, A., MAZOR, A., KLEINEBUDDE, P., LECOQ, O. & MICHRAFY, A. 2016. Effect of roll-compaction and milling conditions on granules and tablet properties. *European Journal of Pharmaceutics and Biopharmaceutics,* 106**,** 38-49.

QIU, Y., CHEN, Y., ZHANG, G. G., YU, L. & MANTRI, R. V. 2017. *Developing Solid Oral Dosage Forms,* London, Mica Haley.

RAJKUMAR, A. D., REYNOLDS, G. K., WILSON, D., WREN, S. A. C. & SALMAN, A. D. 2019. The effect of roller compaction and tableting stresses on pharmaceutical tablet performance. *Powder Technology,* 341**,** 23-37.

RHODES, M. J. 2008. *Introduction to particle technology,* Hoboken, N.J. : Chichester, Hoboken, N.J. Wiley.

ROJAS., J., URIBE., Y. & ZULUAGA., A. 2012. Powder and compaction characteristics of pregelatinized starches. *Pharmazie,* 67**,** 513-517.

ROWE, J. M., CRISON, J. R., CARRAGHER, T. J., VATSARAJ, N., MCCANN, R. J. & NIKFAR, F. 2013. Mechanistic insights into the scale-up of the roller compaction process: a practical and dimensionless approach. *Journal of Pharmaceutical Sciences,* 102**,** 3586-95.

SAKER, A., CARES-PACHECO, M. G., MARCHAL, P. & FALK, V. 2019. Powders flowability assessment in granular compaction: What about the consistency of Hausner ratio? *Powder Technology,* 354**,** 52-63.

SALEHI, H., BARLETTA, D. & POLETTO, M. 2017. A comparison between powder flow property testers. *Particuology,* 32**,** 10-20.

SCHULZE, D. 2007**.** *Powders and Bulk Solids_ Behavior, Characterization, Storage and Flow,* Berlin, Springer.

SKIKANT, P., AKASH, J., MAHESH, D. & ASTIK, S. 2015. Roller compaction design and critical parameters in drug formulation and development: review. *Internatinal Journal PharmTech Research,* Vol.7, No. 1**,** 90-98.

STOKLOSA, A. M., LIPASEK, R. A., TAYLOR, L. S. & MAUER, L. J. 2012. Effects of storage conditions, formulation, and particle size on moisture sorption and flowability of powders: A study of deliquescent ingredient blends. *Food Research International,* 49**,** 783-791.

SUN, C. C. 2016. Quantifying effects of moisture content on flow properties of microcrystalline cellulose using a ring shear tester. *Powder Technology,* 289**,** 104-108.

TAO, H., LI, M., DENG, H.-D., REN, K.-X., ZHUANG, G.-Q., XU, X.-M. & WANG, H.-L. 2019. The impact of sodium carbonate on physico-chemical properties and cooking qualities of starches isolated from alkaline yellow noodles. *International Journal of Biological Macromolecules,* 137**,** 697-702.

TENG, Y., QIU, Z. & WEN, H. 2009. Systematical approach of formulation and process development using roller compaction. *European Journal of Pharmaceutics and Biopharmaceutics,* 73**,** 219-29.

WEYENBERG, W., VERMEIRE, A., VANDERVOORT, J., REMON, J. P. & LUDWIG, A. 2005. Effects of roller compaction settings on the preparation of bioadhesive granules and ocular minitablets. *European Journal of Pharmaceutics and Biopharmaceutics,* 59**,** 527-36.

WIEDEY, R. & KLEINEBUDDE, P. 2018. Infrared thermography — A new approach for in-line density measurement of ribbons produced from roll compaction. *Powder Technology,* 337**,** 17-24.

WIEDEY, R., SIBANC, R., WILMS, A. & KLEINEBUDDE, P. 2018. How relevant is ribbon homogeneity in roll compaction/dry granulation and can it be influenced? *European Journal of Pharmaceutics and Biopharmaceutics,* 133**,** 232-239.

WU, C. Y., HUNG, W. L., MIGUELEZ-MORAN, A. M., GURURAJAN, B. & SEVILLE, J. P. 2010. Roller compaction of moist pharmaceutical powders. *International Journal of Pharmaceutics,* 391**,** 90-7.

YU, M., OMAR, C., SCHMIDT, A., LITSTER, J. D. & SALMAN, A. D. 2018. Improving feeding powder distribution to the compaction zone in the roller compaction. *European Journal of Pharmaceutics and Biopharmaceutics,* 128**,** 57-68.

YU, M., OMAR, C., WEIDEMANN, M., SCHMIDT, A., LITSTER, J. D. & SALMAN, A. D. 2020a. Roller compaction: Infrared thermography as a PAT for monitoring powder flow from feeding to compaction zone. *International Journal of Pharmaceutics,* 578**,** 119114.

YU, M., WEIDEMANN, M., OMAR, C. S., SCHMIDT, A., LITSTER, J. D. & SALMAN, A. D. 2020b. Application of feeding guiders to improve the powder distribution in the two scales of roller compactors. *International Journal of Pharmaceutics,* 573**,** 118815.

YU, S., ADAMS, M., GURURAJAN, B., REYNOLDS, G., ROBERTS, R. & WU, C.-Y. 2013. The effects of lubrication on roll compaction, ribbon milling and tabletting. *Chemical Engineering Science,* 86**,** 9-18.

YU, W., MUTEKI, K., ZHANG, L. & KIM, G. 2011. Prediction of bulk powder flow performance using comprehensive particle size and particle shape distributions. *Journal of Pharmaceutical Sciences,* 100**,** 284-93.

Appendix

Appendix - 1

Table A-1. Primary particle size.

Material	D_{10} (μm)	D_{50} (μm)	D_{90} (μm)
Avicel ® MCC PH101	20.9	44.5	76.0
Light Sodium Carbonate	16.1	72.5	182.9
Starch 1500	17.7	60.7	134.4
Pharmatose ® 200 M	10.3	37.9	92.4
Pharmatose ® 350 M	10.6	35.3	75.0
Pharmatose ® 450 M	7.7	22.8	42.8
PVA	37.4	87.0	137.0
KCl	38.4	84.0	162.0
GLUCIDEX ® Maltodextrin 6	19.9	91.9	227.6
GLUCIDEX ® Maltodextrin 19	14.4	69.7	212.4
GLUCIDEX ® Maltodextrin 39	17.0	76.7	198.6
Ethyl Cellulose	70.0	260.0	521.0
Tylopur ® 603 HPMC	23.9	64.3	124.7
$CaCO_3$ – small size	2.0	8.0	12.0
$CaCO_3$ – middle size	2.0	14.0	94.0
$CaCO_3$ – large size	20.0	85.0	200.0
Polyplasdone xl-10	11.4	23.6	45.7

Table A-2. Table of primary particle size distribution.

<table>
<tr>
<td>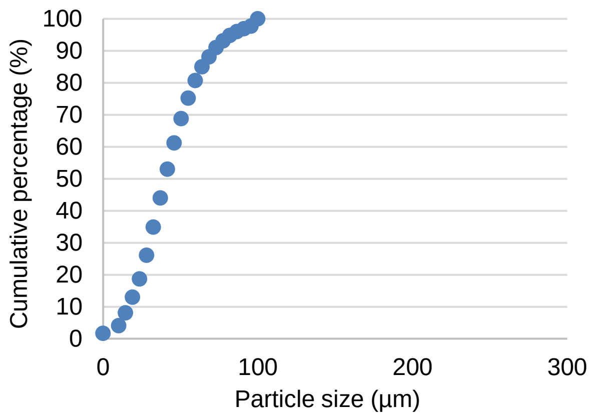

Avicel ® PH101 MCC</td>
<td>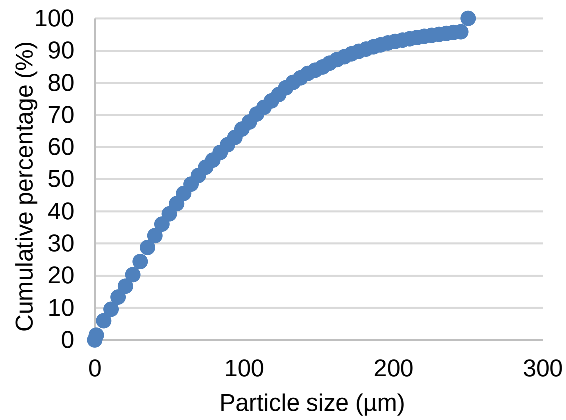

Light Sodium Carbonate</td>
</tr>
<tr>
<td>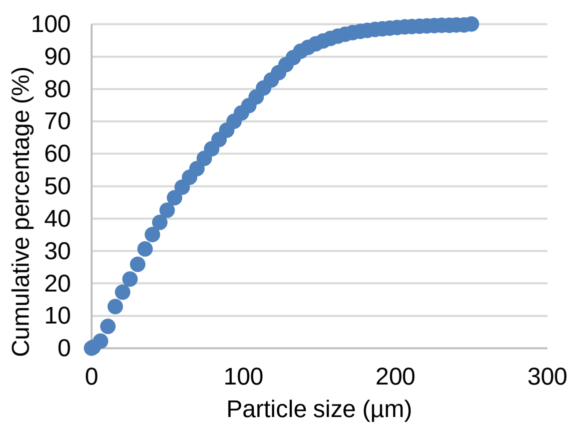

Starch 1500</td>
<td>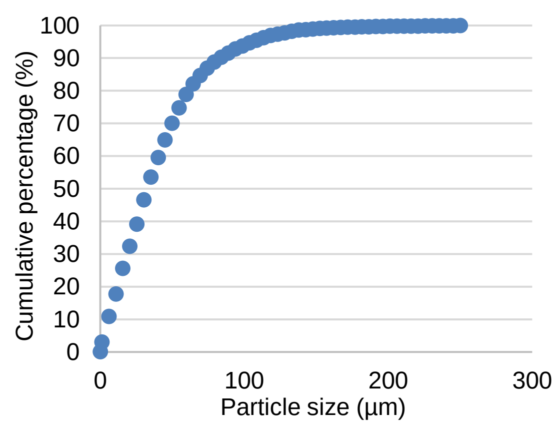

Pharmatose ® 200 M</td>
</tr>
</table>

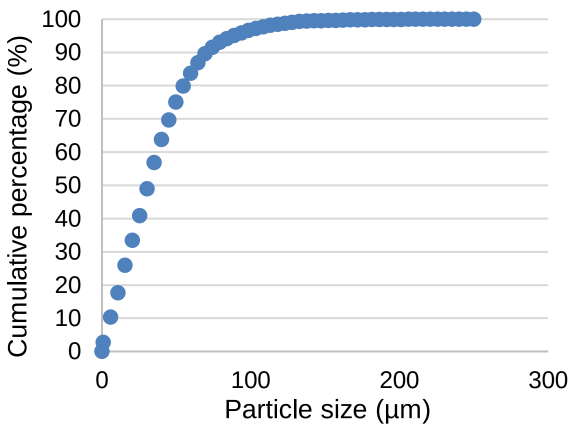

Pharmatose ® 350 M

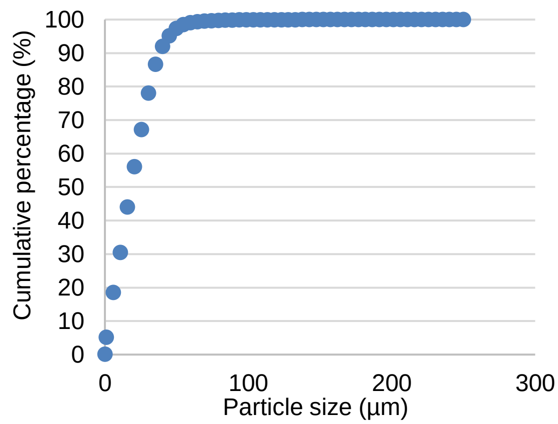

Pharmatose ® 450 M

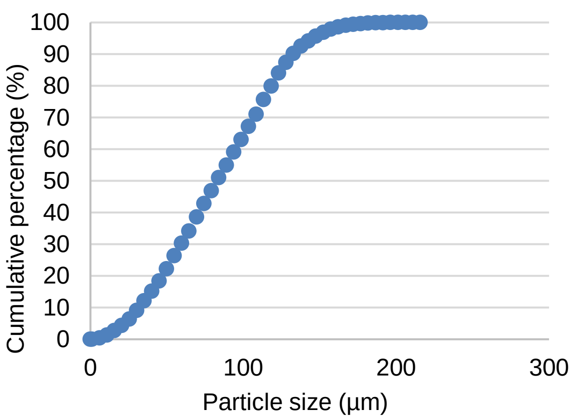

PVA

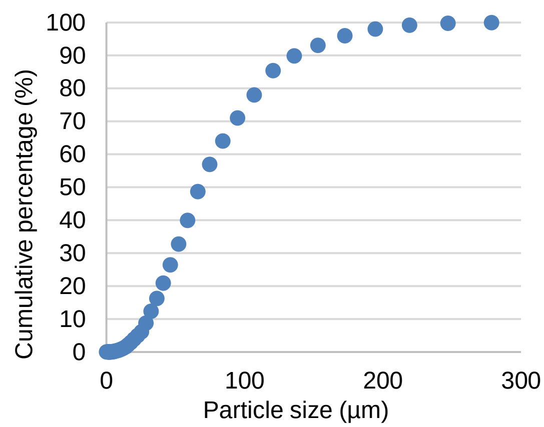

KCl

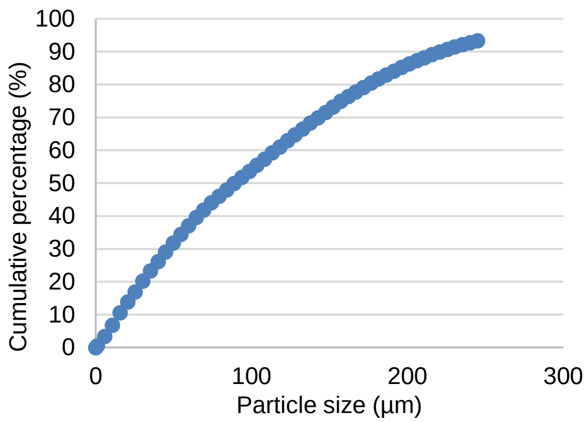

GLUCIDEX ® DE6

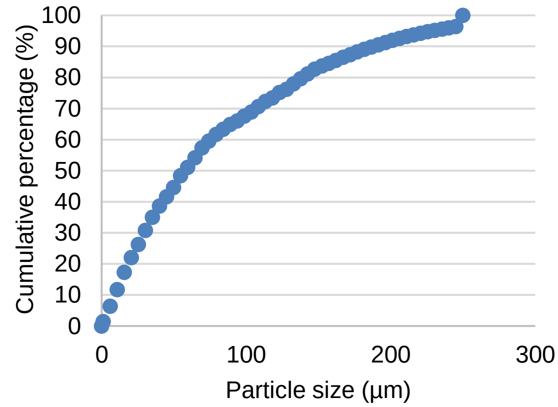

GLUCIDEX ® DE19

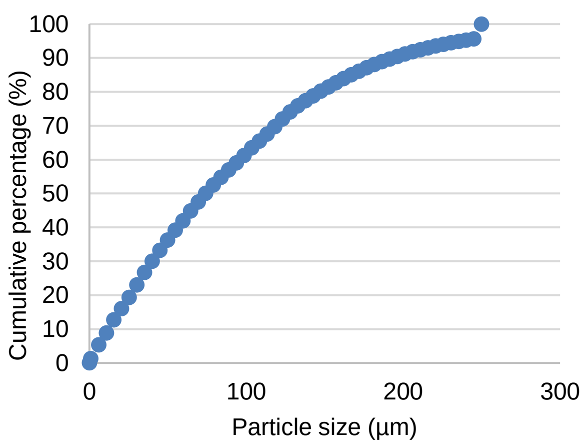

GLUCIDEX ® DE39

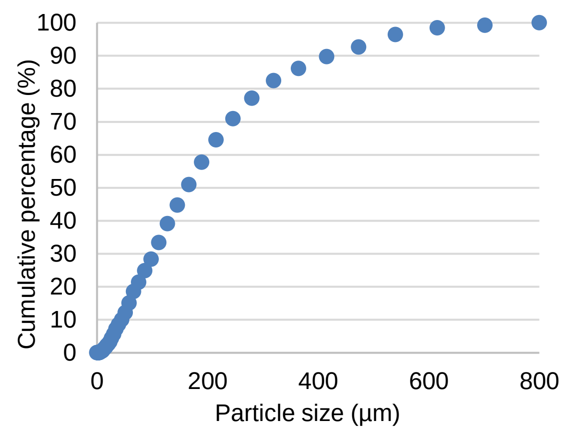

Ethyl Cellulose

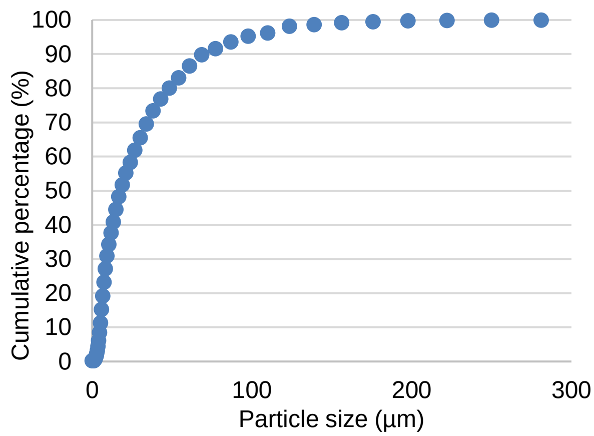

$CaCO_3$ – middle size

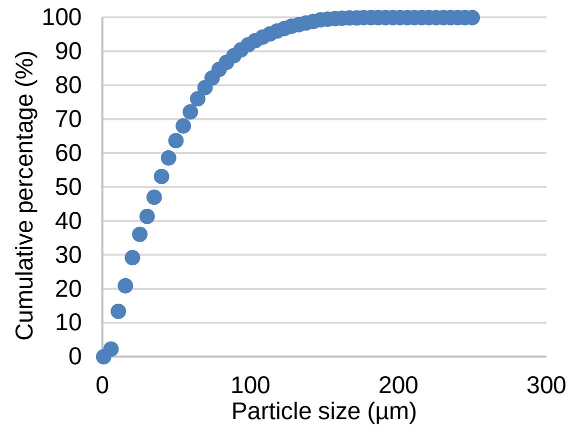

Tylopur ® 603

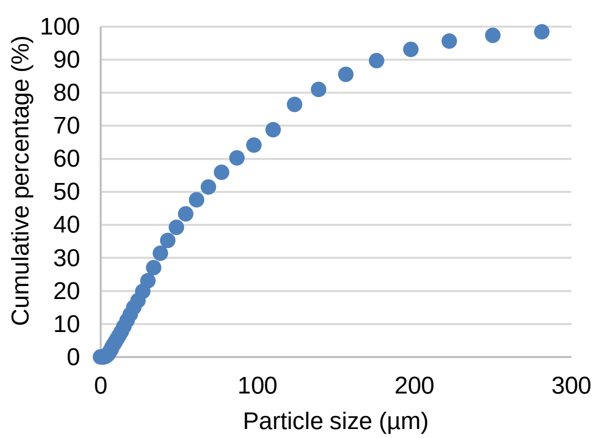

$CaCO_3$ – large size

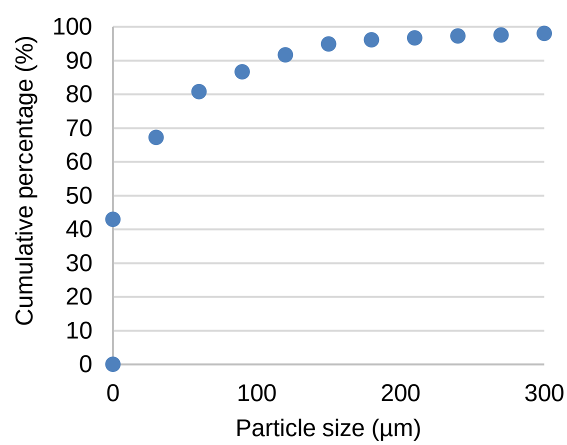

$CaCO_3$ – small size

Appendix - 2

Table A-3. Particle shape by scanning electron microscopy (SEM).

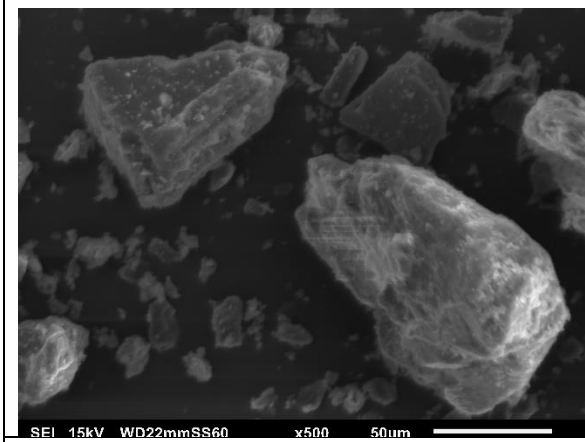	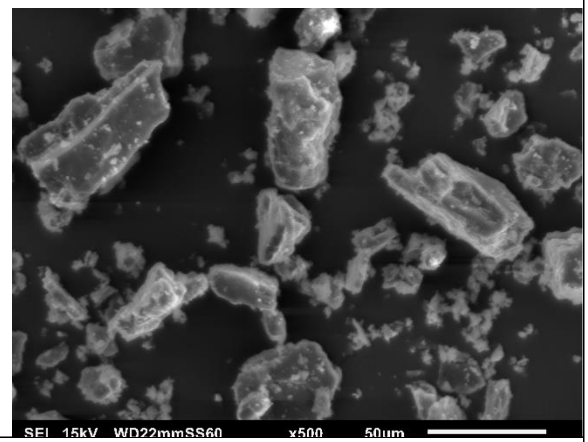
Pharmatose ® 350 M	Pharmatose ® 450 M
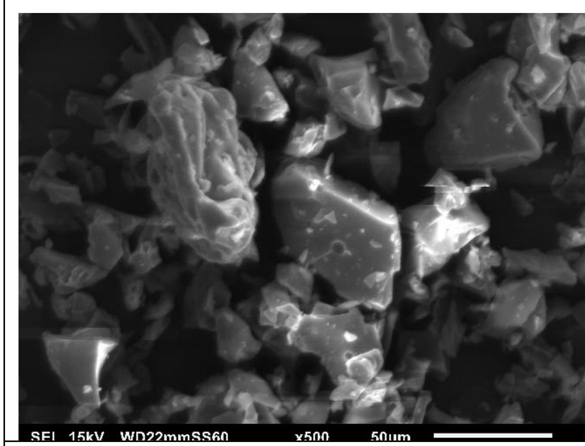	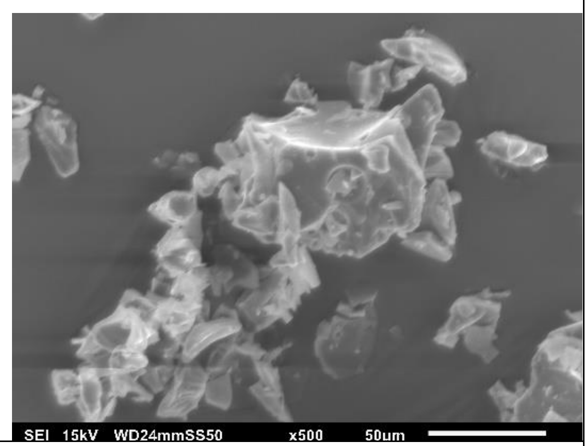
Maltodextrin ® 19	Maltodextrin ® 39

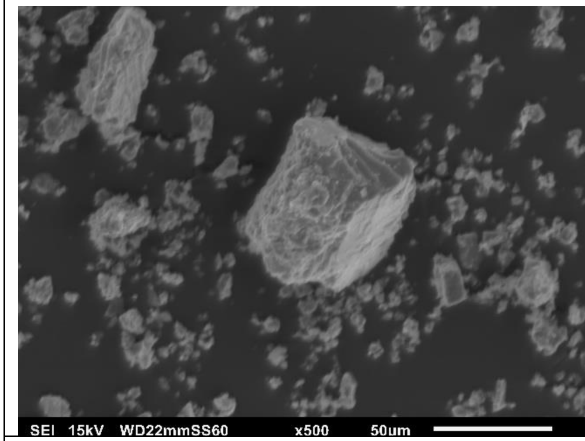

Calcium carbonate - large size

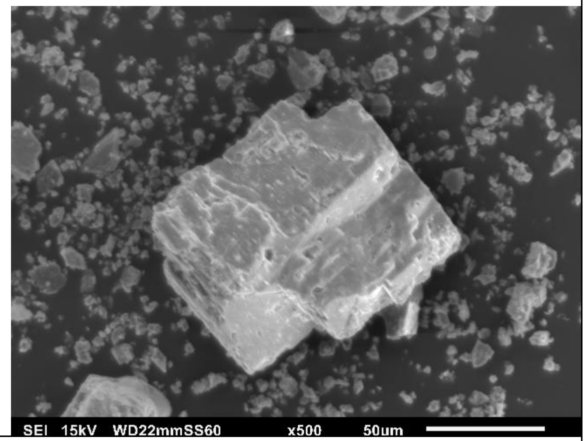

Calcium carbonate - middle size

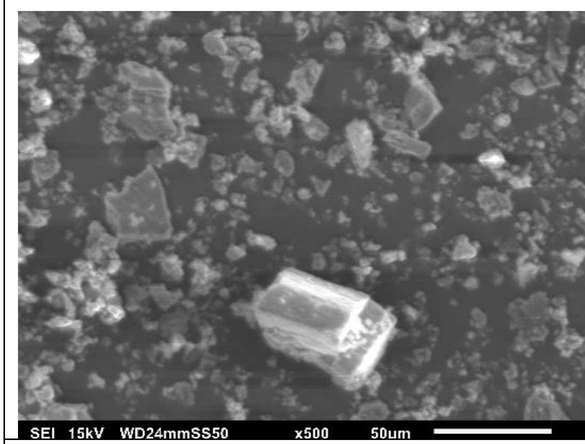

Calcium carbonate – small size

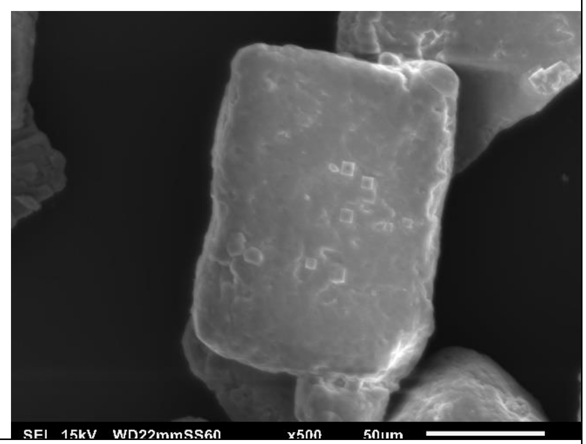

KCl

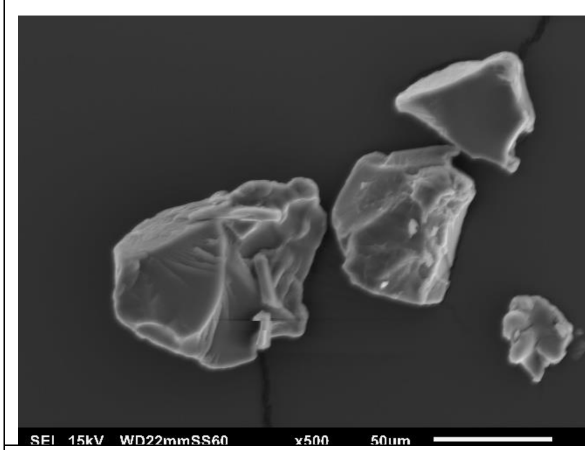

Polyvinyl Alcohol (PVA)

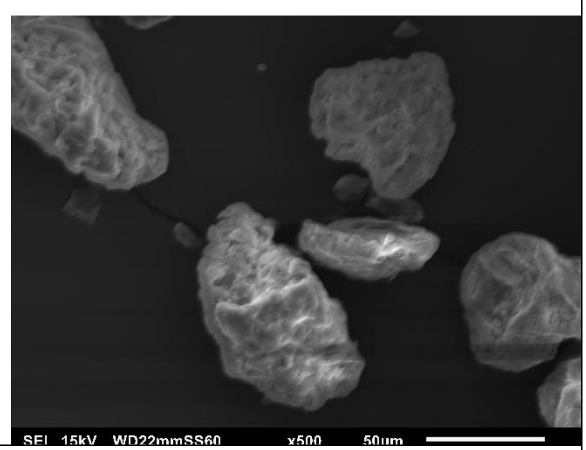

Ethyl cellulose

Appendix - 3

Table A-4. Hydraulic pressure and roller force – WP 120 Pharma and WP 200 Pharma (Alexanderwerk AG, Germany).

Hydraulic pressure (Bar) (MPa)	Roller force (KN)	
	WP 120 Pharma	WP 200 Pharma
20	8.29	15.54
30	12.44	23.33
40	16.58	31.09
50	20.72	38.85
60	24.88	46.65
70	29.02	54.41
80	33.17	62.19
100	41.47	77.76
120	49.76	93.3
140	58.05	108.84
160	66.35	124.41
180	74.64	139.95
200	82.94	155.51
215	89.16	167.18
230	95.38	178.84

Appendix - 4

Table A-5. Emissivity of different materials.

Materials	Emissivity
Pharmatose ® 200M	0.98 ± 0.01
Avicel ® PH101 MCC	0.94 ± 0.01
Tylopur ® 603 HPMC	0.96 ± 0.01
Light Sodium Carbonate	0.95 ± 0.01
GLUCIDEX ® Maltodextrin DE6	0.97 ± 0.01
Starch 1500	0.96 ± 0.01

Appendix - 5

Table A-6: Angle of repose at 40% and 60% relative humidity.

Materials	Angle of repose (40%)	Angle of repose (60%)
Starch 1500	31.3 ± 0.3	35.8 ± 0.4
PVA	32.7 ± 1.1	36.7 ± 0.9
Ethyl Cellulose	32.9 ± 0.9	32.9 ± 0.6
Polyplasdone xl-10	33.6 ± 0.7	36.6 ± 0.9
Glucidex ® maltodextrin DE6	35.8 ± 1.2	39.8 ± 1.1
Avicel MCC PH101	38.4 ± 1.2	48.4 ± 0.4
KCl	39.3 ± 0.8	46.3 ± 1.2
Glucidex ® maltodextrin DE39	40.6 ± 1.3	Caking
Glucidex ® maltodextrin DE19	41.8 ± 1.4	43.2 ± 1.3
Tylopur ® 603 HPMC	43.3 ± 0.3	47.3 ± 0.3
Pharmatose ® 200 M	44.5 ± 0.5	48.6 ± 1.2
$CaCO_3$ – large size	44.5 ± 1.5	49.1 ± 0.9
Light Sodium Carbonate	44.8 ± 1.4	43.6 ± 1.1
$CaCO_3$ – middle size	45.2 ± 1.6	47.5 ± 0.9
$CaCO_3$ – small size	45.4 ± 1.5	49.5 ± 0.9
Pharmatose ® 350 M	45.6 ± 0.8	48.3 ± 0.8
Pharmatose ® 450 M	46.6 ± 0.9	46.8 ± 0.9

Appendix - 6

Table A-7: Flow function coefficient at 40% and 60% relative humidity.

Materials	ffc - 40 % (RH)	ffc - 60 % (RH)
Pharmatose ® 450 M	2.63 ± 0.06	2.59 ± 0.29
CaCO3 – small size	3.00 ± 0.01	3.08 ± 0.03
CaCO3 – large size	3.08 ± 0.11	3.13 ± 0.06
Pharmatose® 200 M	3.23 ± 0.13	3.04 ± 0.02
CaCO3 – middle size	3.32 ± 0.04	3.43 ± 0.30
Pharmatose ® 350 M	3.35 ± 0.07	3.33 ± 0.15
Avicel ® PH 101 MCC	3.70 ± 0.23	2.68 ± 0.12
Glucidex ® maltodextrin DE19	3.87 ± 0.21	3.45 ± 0.36
Tylopur ® 603 HPMC	4.33 ± 0.11	3.51 ± 0.17
Light Sodium Carbonate	5.09 ± 0.43	4.39 ± 0.23
KCl	5.11 ± 0.26	4.35 ± 0.23
Glucidex ® maltodextrin DE39	5.13 ± 0.16	Caking
Polyplasdone xl-10	5.78 ± 0.46	2.02 ± 0.01
Ethyl cellulose	6.15 ± 0.47	5.44 ± 0.26
Glucidex ® maltodextrin DE6	6.50 ± 0.25	3.43 ± 0.23
Starch 1500	8.05 ± 0.25	3.66 ± 0.33
PVA	12.51 ± 0.32	5.70 ± 0.31

Appendix - 7

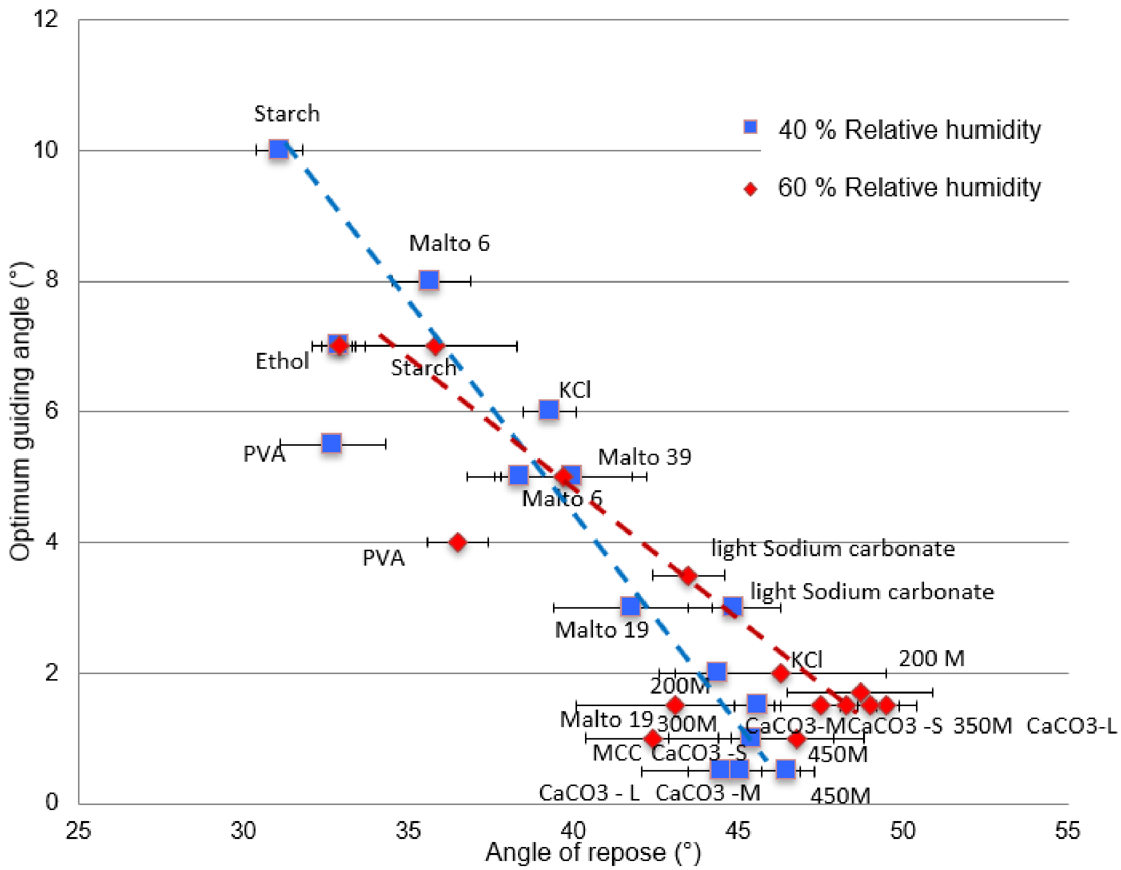

Figure A-1. Optimum guiding angle as a function of repose angle for different powder conditioned at different relative humidity at 20 °C.

Appendix - 8

Table A-8. Thermal images of ribbon surface temperature - Pharmatose ® 200 M.

	Pharmatose ® 200 M			
Roller force 8.29 kN	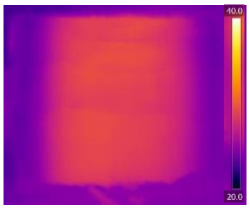 Original	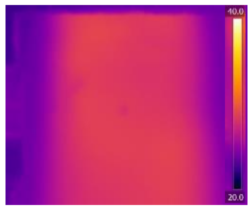 T-9	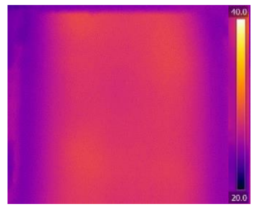 T-10	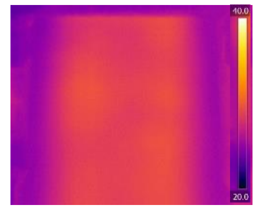 T-11
Roller force 20.72 kN	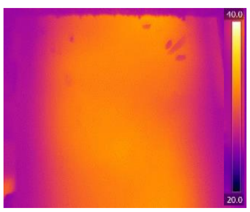 Original	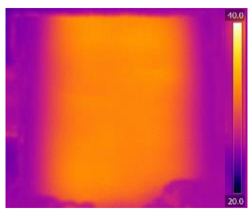 T-9	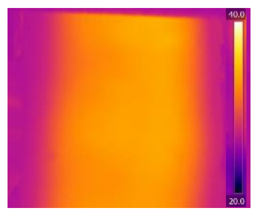 T-10	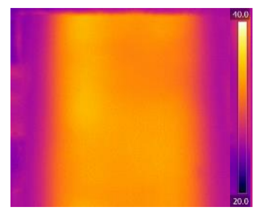 T-11
Roller force 29.02 kN	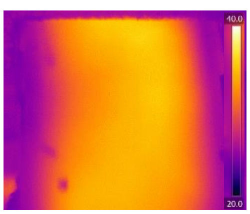 Original	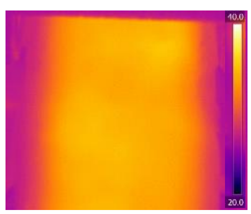 T-9	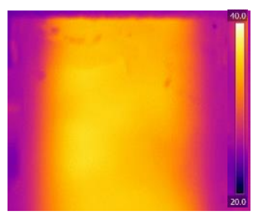 T-10	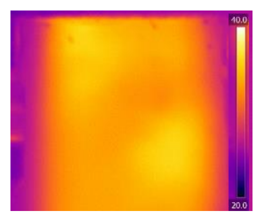 T-11
Roller force 49.76 kN	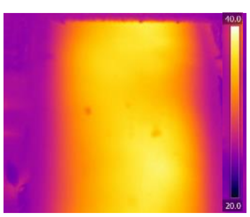 Original	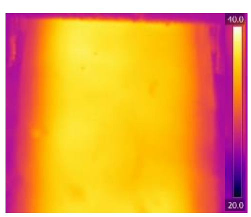 T-8	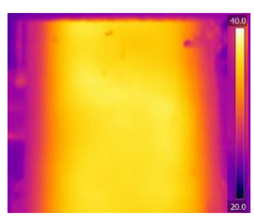 T-9	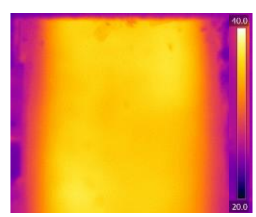 T-10

Table A-9. Thermal images of ribbon surface temperature - Avicel ® PH101 MCC.

	Avicel ® PH101 MCC			
Roller force 8.29 kN	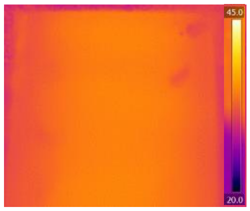 Original	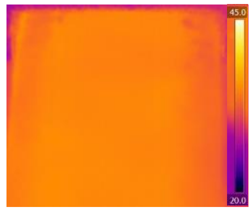 T-10	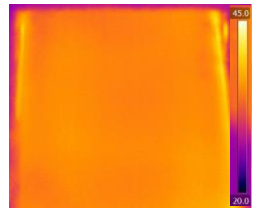 T-11	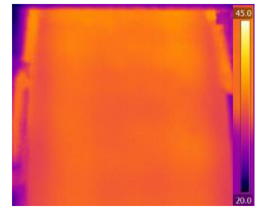 T-12
Roller force 20.72 kN	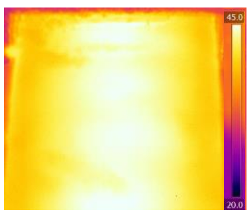 Original	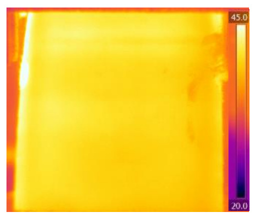 T-6	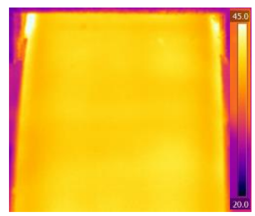 T-7	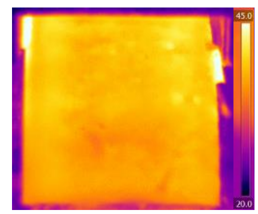 T-8
Roller force 29.02 kN	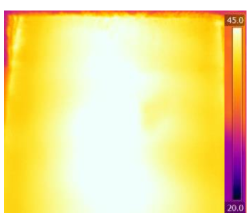 Original	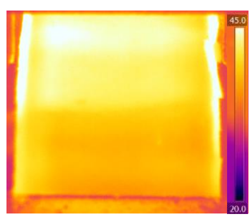 T-5	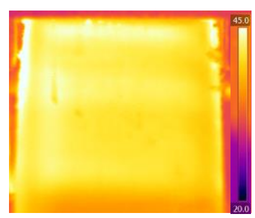 T-6	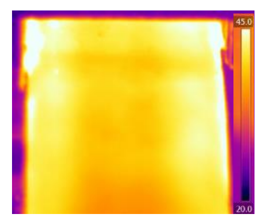 T-7
Roller force 49.76 kN	 Original	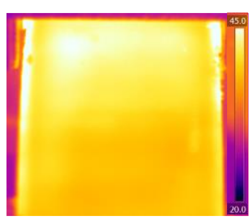 T-3	 T-4	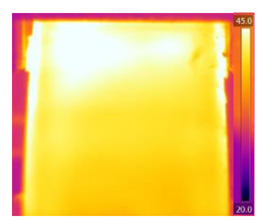 T-5

Table A-10. Thermal images of ribbon surface temperature - Tylopur ® 603 HPMC.

	Tylopur ® 603 HPMC			
Roller force 8.29 kN	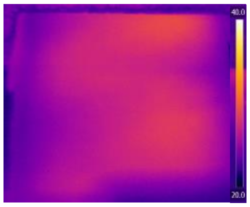 Original	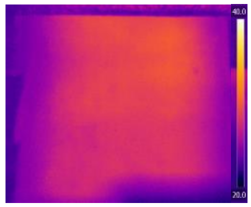 T-10	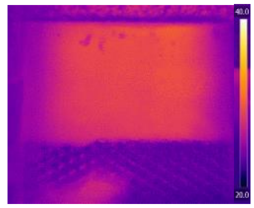 T-11	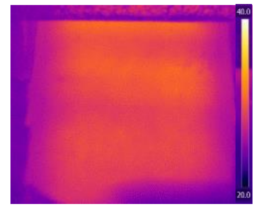 T-12
Roller force 20.72 kN	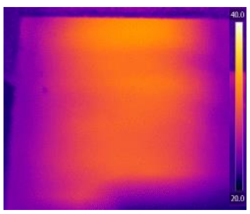 Original	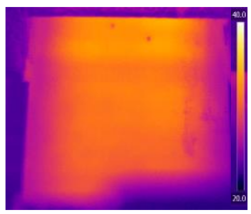 T-9	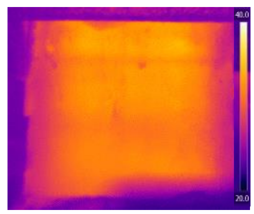 T-10	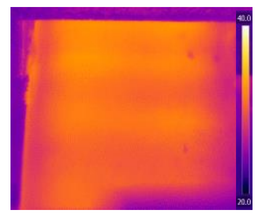 T-11
Roller force 29.02 kN	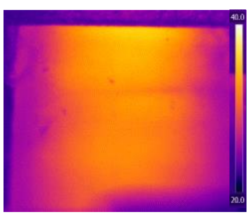 Original	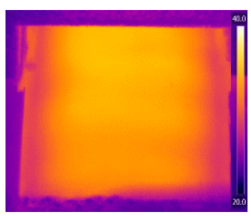 T-8	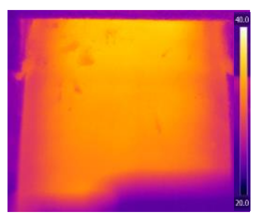 T-9	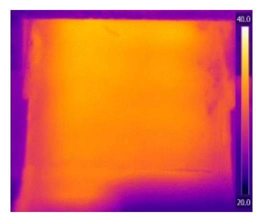 T-10
Roller force 49.76 kN	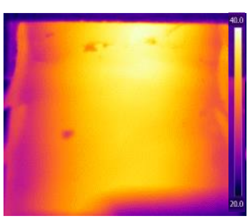 Original	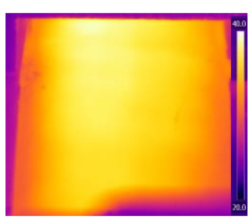 T-7	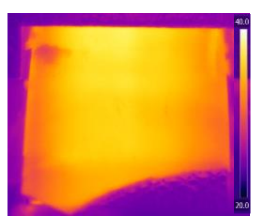 T-8	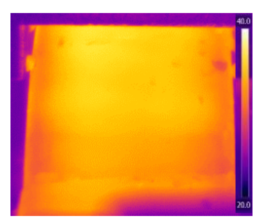 T-9

Table A-11. Thermal images of ribbon surface temperature - LSC.

	Light Sodium Carbonate (LSC)			
Roller force 8.29 kN	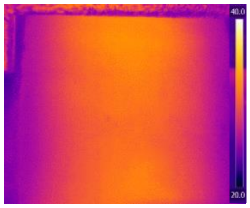 Original	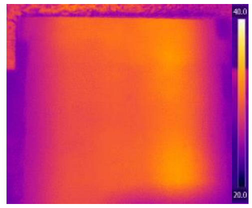 T-12	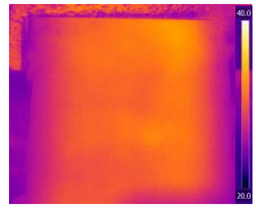 T-13	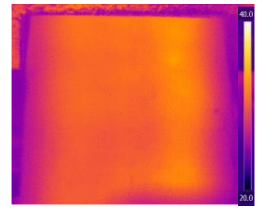 T-14
Roller force 20.72 kN	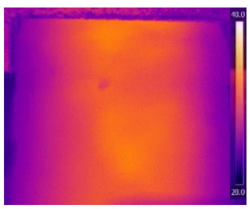 Original	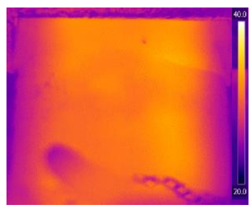 T-9	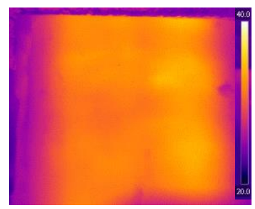 T-10	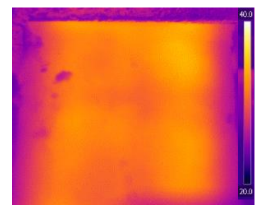 T-11
Roller force 29.02 kN	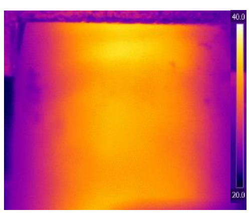 Original	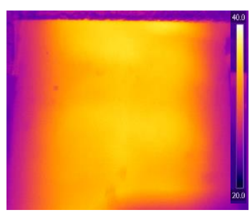 T-7	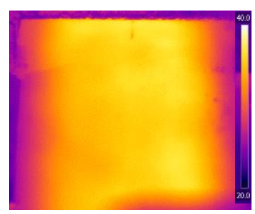 T-8	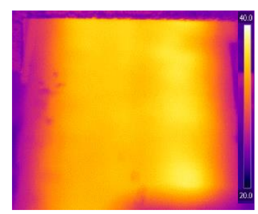 T-9
Roller force 49.76 kN	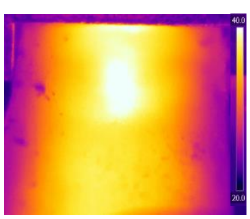 Original	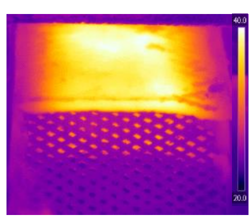 T-7	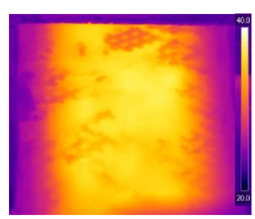 T-8	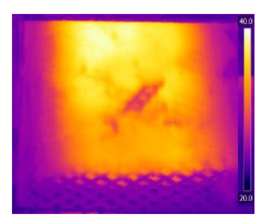 T-9

Table A-12. Thermal images of ribbon surface temperature - GLUCIDEX ® Maltodextrin DE6

	GLUCIDEX ® Maltodextrin DE6			
Roller force 8.29 kN	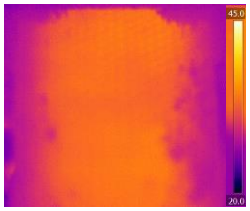 Original	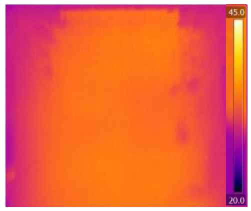 T-9	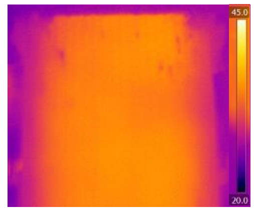 T-10	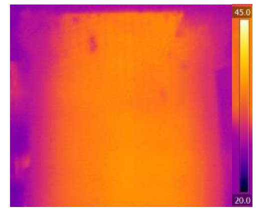 T-11
Roller force 20.72 kN	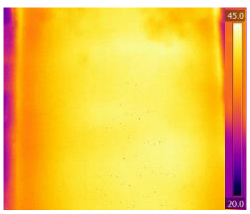 Original	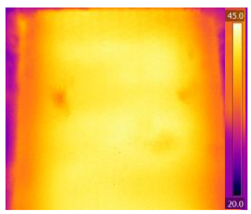 T-6	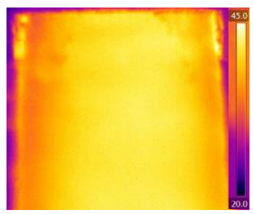 T-7	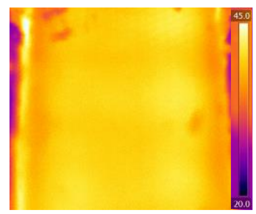 T-8
Roller force 29.02 kN	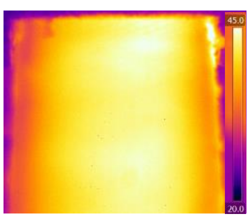 Original	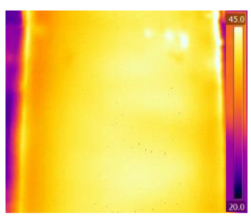 T-5	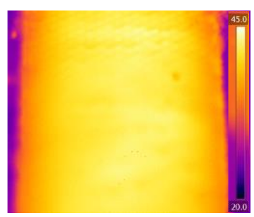 T-6	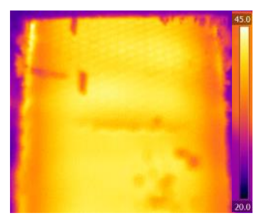 T-7
Roller force 49.76 kN	 Original	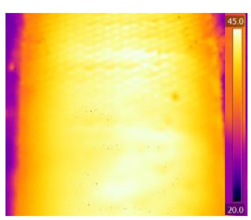 T-4	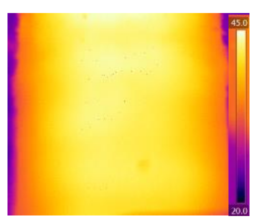 T-5	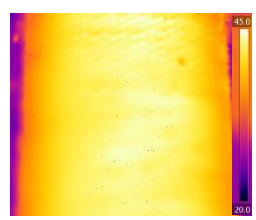 T-6

Table A-13. Thermal images of ribbon surface temperature – Starch 1500.

	Starch 1500			
Roller force 8.29 kN	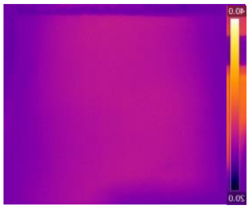 Original	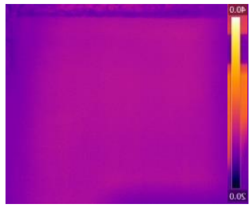 T-12	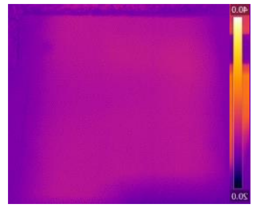 T-13	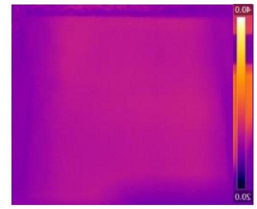 T-14
Roller force 20.72 kN	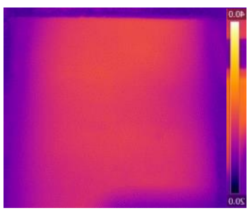 Original	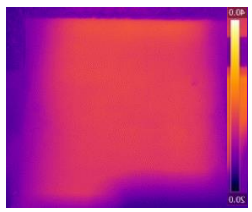 T-9	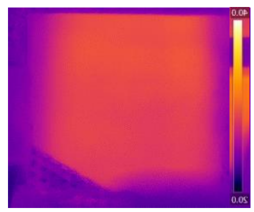 T-10	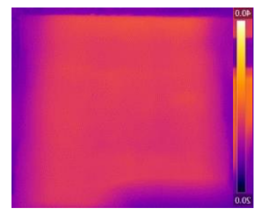 T-11
Roller force 29.02 kN	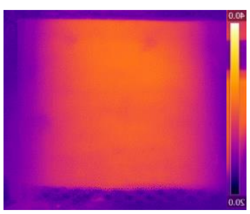 Original	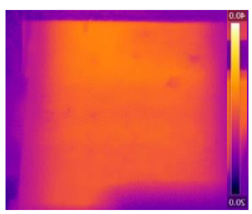 T-8	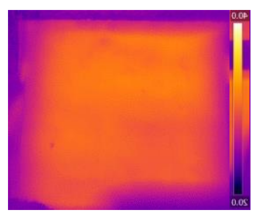 T-9	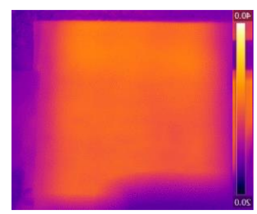 T-10
Roller force 49.76 kN	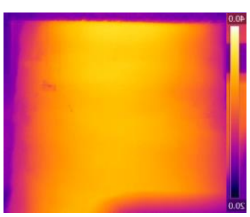 Original	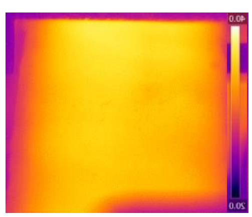 T-7	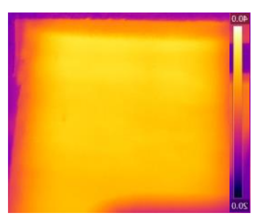 T-8	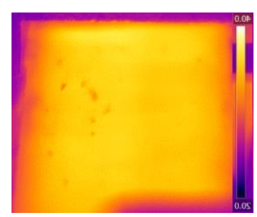 T-9